

**COMPUTER-AIDED DESIGN OF PASSIVE MICROWAVE COMPONENTS
NONSTANDARD RECTANGULAR WAVEGUIDE TECHNOLOGY**

by

Vladimir Andrew Labay
B.Sc.(E.E.), University of Manitoba, 1987
M.Sc., University of Manitoba, 1990

*A dissertation Submitted in Partial Fulfillment of the
Requirements for the Degree of*

DOCTOR OF PHILOSOPHY

in the Department of Electrical and Computer Engineering

We accept this thesis as conforming to the required standard

DR. JENS BORNEMANN, Supervisor
Professor, Department of Electrical and Computer Engineering

DR. RUEBINGER VAHLDIECK, Departmental Member
Professor, Department of Electrical and Computer Engineering

DR. R. LYNN KIRLIN, Departmental Member
Professor, Department of Electrical and Computer Engineering

DR. RON P. PODHODESKI, Outside Member
Assistant Professor, Department of Mechanical Engineering

DR. AL WEXLER, External Examiner
Professor Emeritus, University of Manitoba and President, Quantic Laboratories Inc.

© Vladimir Andrew Labay, 1995

University of Victoria

All rights reserved. Dissertation may not be reproduced in whole or in part, by photocopying or other means, without the permission of the author.

A.M.D.G.

Supervisor: Dr. Jens Bornemann, Professor

ABSTRACT

Continued advancement in microwave telecommunications generates an ever increasing need for the further development of computer-aided analysis and design tools. The objective of this thesis is to develop computer-aided design algorithms for the construction of original and innovative components in an all-metal nonstandard rectangular waveguide technology, and to do so employing accurate electromagnetic field analysis. Nevertheless, the principles derived from this relatively narrow field of research are applicable to other waveguide technologies.

Through the examination of a variety of ways to accomplish this, a mode-matching method is found best suited to this purpose. A building block approach, involving the separate analysis of smaller discrete discontinuities leading to the cascading and combining of them through the Generalized S-matrix Method, is selected as having the greatest potential for universal application. Two nonstandard discontinuities are selected for further pursuit: as an example of two-port discontinuities, the T-septum waveguide; and, as an example of multi-ports, the discontinuity-distorted T-junction. To facilitate the discussion of these nonstandard discontinuities, mode-matching is reviewed by solving a double-plane step and a simple E -plane T-Junction.

The first objective, when applying mode-matching to nonstandard rectangular waveguide discontinuities, is to determine the propagation characteristics or eigenmodes of each subregion of the discontinuity. The standing wave formulation in conjunction with a minimum singular value decomposition algorithm is employed to determine the cut-off frequencies of a T-septum waveguide. The results are then employed in the application of mode-matching to a rectangular-to-T-septum waveguide

discontinuity. The discontinuity is shown to be advantageous in the design of evanescent-mode filters, transformers, and diplexers. Two prototypes, a bandpass filter and a diplexer, were built and tested. With the exception of poor insertion loss performance attributable to an unanticipated poor level of conductivity in material coupled with an additional loss resulting from the abrupt conjunction of the miniaturized T-septum filter segments with the larger input/output waveguides, the measurements compared well to calculated responses.

The theoretical and numerical analysis of nonstandard two-port theory is expanded to include multi-ports. The formulation produces the generalized scattering matrix of a discontinuity-distorted T-junction by applying superposition to the non-homogeneous boundary conditions toward a solution of the Helmholtz equation in determining the eigenmodes of the resonator region. The waveguide corner, being a special case of the T-junction, is used to demonstrate the accuracy of the formulation through its high level of agreement with known measurements and calculated results of mitered 90° and 180° waveguide bends. This discontinuity is then employed to develop improved compact three-port components, namely power dividers and orthomode transducers. Power dividers are shown to demonstrate improved division over a wider bandwidth compared with conventional designs. The orthomode transducer while producing similar responses to conventional designs is significantly reduced in size.

The formulations presented in this thesis have proven to be accurate and successful in all of the applications presented here and promise to be of substantial benefit in the area of component design in the future.

DR. J. BORNEMANN, Supervisor

DR. R. VAHLDECK, Departmental Member

DR. R. L. KIRLIN, Departmental Member

DR. R. PODHORODESKI, Outside Member

DR. A. WEXLER, External Examiner

TABLE OF CONTENTS

ABSTRACT	ii
TABLE OF CONTENTS	iv
LIST OF FIGURES	v
ACKNOWLEDGMENTS	xi
DEDICATION	xii
1. OVERVIEW	1
1.1. Introduction	1
1.2. Waveguide Discontinuities: Modeling and Analysis	4
1.2.1. Theoretical Background	4
1.2.2. Two-Port Junctions with Nonstandard Waveguide Cross-sections	9
1.2.3. Multi-port Junctions with Nonstandard Resonator Regions	11
1.3. Passive Microwave Rectangular Waveguide Components	12
1.3.1. Two-Port Components	12
1.3.2. Waveguide Corners and Three-port Components	13
1.4. Methodology and Organization	15
2. THE MODE-MATCHING METHOD	17
2.1. Introduction	17
2.2. Theoretical Background	18
2.3. Two-Port Waveguide Junction: A Double-Plane Step	21
2.4. Three-Port Waveguide Junction: An <i>E</i>-Plane T-Junction	24
3. T-SEPTUM WAVEGUIDE	28
3.1 Introduction	28
3.2 Eigenvalue Problem	28

3.3	Rectangular-to-T-Septum Waveguide Discontinuity	40
3.4	Component Design	44
	3.4.1. Bandpass Filters	44
	3.4.2. Transformers	51
	3.4.3. Diplexers	54
4.	DISCONTINUITY-DISTORTED T-JUNCTIONS	61
4.1.	Introduction	61
4.2.	T-junction with Discontinuity-Distorted Resonator Region	65
	4.2.1 Theoretical Formulation	66
4.3.	T-Junction with Stepped Resonator Region	82
4.4.	Waveguide Corners	87
	4.4.1. 90° Waveguide Corners	89
	4.4.2. 180° Waveguide Corners	91
4.5.	Component Design	92
	4.5.1. Power Divider	93
	4.5.2. Orthomode Transducer	97
5.	CONCLUSIONS AND RECOMMENDATIONS	103
5.1.	Conclusions	103
5.2.	Recommendations	106
	References	108
	APPENDIX A: GENERALIZED S-MATRIX METHOD	117
	A.1. Introduction	117
	A.2. Two Two-Ports	117
	A.3. Two-Port and Homogeneous Waveguide	118
	A.4. Two-Port and Its Inverse Structure	119
	A.5. Two-port and Three-port	120
	APPENDIX B: ELECTRIC FIELD DISTRIBUTION	122
	APPENDIX C: ALTERNATIVE MATRIX INVERSION	125

LIST OF FIGURES

- FIGURE 1.1** Examples of standard rectangular waveguide discontinuities: (a) asymmetrical double-plane step waveguide junction (two-port); (b) waveguide corner (two-port); (c) *E*-plane T-junction (three-port); (d) Magic T (four-port). 8
- FIGURE 1.2** Examples of rectangular waveguides with a nonstandard cross-section: (a) double ridge septum; (b) double T-septum. 9
- FIGURE 1.3** Examples of multi-ports junctions with a nonstandard resonator region: (a) stepped mitered waveguide corner; (b) ridged *E*-plane T-junction. 12
- FIGURE 1.4** (a) Evanescent-mode T-septum filter; (b) Stepped T-septum transformer. 14
- FIGURE 1.5** (a) Integrated T-septum diplexer; (b) Compact power divider; (c) Compact orthomode transducer. 15
- FIGURE 2.1** Double-plane step discontinuity: (a) end view; (b) side view. (cf. Figure 1.1 for a three-dimensional view). 21
- FIGURE 2.2** Simple *E*-plane T-junction of three rectangular waveguides: (a) end view; (b) side view. (cf. Figure 1.1 for a three-dimensional view). 24
- FIGURE 3.1** T-septum waveguide cross-section (quarter section): (a) dimensions and subregions for the transverse-resonance method (TRM); (b) dimensions and subregions for the standing wave formulation (SWF). 29
- FIGURE 3.2** Typical behavior of system determinant and minimum singular value versus frequency: (a) transverse resonance method (TRM); (b) standing wave formulation (SWF). Dimensions (mm): $a = 22.86$, $b = 11.425$, $a_1 = 5.7125$, $a_2 = 10.2825$, $b_1 = 0.8569$ and $b_2 = 1.1425$ (cf. Figure 3.1). 37
- FIGURE 3.3** Convergence analysis and comparison with [35]: (a) normalized cut-off wavelength of fundamental-mode; (b) normalized cut-off wavelength of first higher mode. Dimensions same as in Figure 3.2. 39

- FIGURE 3.4** Geometry of a rectangular-to-T-septum waveguide discontinuity: (a) end view; (b) side view. 40
- FIGURE 3.5** Structure of an evanescent-mode bandpass filter: (a) end view; (b) side view (cf. Figure 1.4(a) for a cut-away view of the filter). 45
- FIGURE 3.6** (a) Calculated transmission and reflection of an X-band three-resonator evanescent-mode T-septum waveguide filter; (b) stopband response. Dimensions (mm): $a_i = 22.86$, $b_i = 10.16$, $a = 7.06$, $b = 6.98$, $a_1 = 1.0$, $a_2 = 2.556$, $b_1 = 0.5$, $b_2 = 1.5$, $l_1 = l_7 = 0.49$, $l_2 = l_6 = 0.51$, $l_3 = l_5 = 7.60$ and $l_4 = 1.20$ (cf. Figures 3.1 and 3.5). 47
- FIGURE 3.7** (a) Calculated transmission and reflection of an X-band five-resonator evanescent-mode T-septum waveguide filter; (b) stopband response. Dimensions (mm): $a_i = 22.86$, $b_i = 10.16$, $a = 7.06$, $b = 6.98$, $a_1 = 1.0$, $a_2 = 2.53$, $b_1 = 0.49$, $b_2 = 1.49$, $l_1 = l_{11} = 0.47$, $l_2 = l_{10} = 0.488$, $l_3 = l_9 = 7.85$, $l_4 = l_8 = 0.983$, $l_5 = l_7 = 8.59$ and $l_6 = 0.983$ (cf. Figures 3.1 and 3.5). 48
- FIGURE 3.8** (a) Calculated transmission and reflection of a Ka-band three-resonator evanescent-mode T-septum waveguide filter; (b) stopband response. Dimensions (mm): $a_i = 7.112$, $b_i = 3.161$, $a = 2.1964$, $b = 2.1716$, $a_1 = 0.3111$, $a_2 = 0.7952$, $b_1 = 0.1556$, $b_2 = 0.4667$, $l_1 = l_7 = 0.1524$, $l_2 = l_6 = 0.1587$, $l_3 = l_5 = 2.2644$ and $l_4 = 0.3174$ (cf. Figures 3.1 and 3.5). 49
- FIGURE 3.9** (a) Comparison between the measured and calculated response of an X-band three-resonator filter prototype; (b) stopband response. Dimensions (mm): $a_i = 22.86$, $b_i = 10.16$, $a = 7.0$, $b = 6.95$, $a_1 = 0.94$, $a_2 = 2.49$, $b_1 = 0.3$, $b_2 = 1.32$, $l_1 = l_7 = 0.54$, $l_2 = l_6 = 0.5$, $l_3 = l_5 = 7.68$ and $l_4 = 0.9$ (cf. Figures 3.1 and 3.5). 50
- FIGURE 3.10** Photograph of the opened evanescent-mode T-septum waveguide filter prototype with feeding X-band waveguide. 51
- FIGURE 3.11** Structure of a T-septum waveguide transformer: (a) end view; (b) side view (cf. Figure 1.4(b) for a cut-away view of the transformer). 52
- FIGURE 3.12** Input return loss of an optimized three-section transformer. 53
- FIGURE 3.13** Structure of a T-septum waveguide diplexer: (a) end view; (b) side view (cf. Figure 1.5(a) for a cut-away view of the diplexer). 54
- FIGURE 3.14** (a) Transmission and input reflection behavior of an integrated T-septum X-band waveguide diplexer; (b) stopband response. Dimensions (mm):

$a_i = 22.86$, $a = 7.112$, $b = 3.5$. Main waveguide filter: $a_1 = 1.0$, $a_2 = 2.556$, $b_1 = 0.5$, $b_2 = 1.5$, $l_1 = l_7 = 0.905$, $l_2 = l_6 = 0.895$, $l_3 = l_5 = 7.73$ and $l_4 = 1.17$. Branch waveguide filter: $a_1 = 1.0$, $a_2 = 2.556$, $b_1 = 0.5$, $b_2 = 1.5$, $l_1 = l_7 = 0.3750$, $l_2 = l_6 = 2.17$, $l_3 = l_5 = 7.15$ and $l_4 = 2.836$ (cf. Figures 3.1 and 3.12). 56

- FIGURE 3.15** (a) Transmission and input reflection behavior of an integrated T-septum Ka-band waveguide diplexer; (b) stopband response. Dimensions (mm): $a_i = 7.112$, $a = 2.2126$, $b = 1.089$. Main waveguide filter: $a_1 = 0.3111$, $a_2 = 0.7952$, $b_1 = 0.1556$, $b_2 = 0.4667$, $l_1 = l_7 = 0.2815$, $l_2 = l_6 = 0.2784$, $l_3 = l_5 = 2.4149$ and $l_4 = 0.364$. Branch waveguide filter: $a_1 = 0.3111$, $a_2 = 0.7952$, $b_1 = 0.1556$, $b_2 = 0.4667$, $l_1 = l_7 = 0.1166$, $l_2 = l_6 = 0.6751$, $l_3 = l_5 = 2.2244$ and $l_4 = 0.4412$ (cf. Figures 3.1 and 3.12). 57
- FIGURE 3.16** Comparison between measured and calculated responses of an integrated X-band T-septum diplexer prototype. Dimensions (mm): $a_i = 22.86$, $a = 7.112$, $b = 3.5$. Main waveguide filter: $a_1 = 1.0$, $a_2 = 2.556$, $b_1 = 0.49$, $b_2 = 1.49$, $l_1 = l_7 = 0.905$, $l_2 = l_6 = 0.895$, $l_3 = l_5 = 7.73$ and $l_4 = 1.17$. Branch waveguide filter: $a_1 = 1.0$, $a_2 = 2.556$, $b_1 = 0.49$, $b_2 = 1.49$, $l_1 = l_7 = 0.3750$, $l_2 = l_6 = 2.17$, $l_3 = l_5 = 7.15$ and $l_4 = 2.836$ (cf. Figures 3.1 and 3.12). 58
- FIGURE 3.17** Photograph of the opened integrated evanescent-mode T-septum waveguide diplexer prototype. 60
- FIGURE 4.1** A three-plane mode-matching method to determine the scattering parameters of a T-junction with discontinuity-distorted resonator region. 63
- FIGURE 4.2** *E*-plane T-junction with discontinuity-distorted resonator region viewed from port 1 along the *z*-axis. 65
- FIGURE 4.3** Discontinuity-distorted *E*-plane T-junction of three rectangular waveguides: (a) end view; (b) side view. 68
- FIGURE 4.4** Superposition of the resonator region for field theory treatment. 69
- FIGURE 4.5** Detailed description of the subregions corresponding to solution (1). 71
- FIGURE 4.6** Detailed description of the subregions corresponding to solution (2). 73
- FIGURE 4.7** Detailed description of the subregions corresponding to solution (3). 75
- FIGURE 4.8** Subdivision assignment for the *E*-plane T-junction stepped resonator re-

- gion: (a) subregions for solutions (1) and (2); (b) subregions for solution (3). 82
- FIGURE 4.9** Structure of a waveguide corner: (a) end view; (b) side view (cf. Figure 1.3(a) for a three-dimensional view of the corner). 88
- FIGURE 4.10** Input return loss of a mitered E -plane corner. Approximation of miter by increasing the number of steps. (a) TE_{10} -mode. (b) TE_{01} -mode. Dimensions (mm): $a = b_1 = b_3 = 22.86$, $\Delta y = 0.0$, $\Delta z = 5.08$, and $\theta = 45.0^\circ$ (cf. Figure 4.9). 90
- FIGURE 4.11** Input return loss of a mitered H -plane corner with 22-step approximation. Dimensions (mm): $a = b_1 = b_3 = 22.86$, $\Delta y = 0.0$, $\Delta z = 6.55$, and $\theta = 45.0^\circ$ (cf. Figure 4.9). 91
- FIGURE 4.12** Comparison of this theory (five-step miter approximation) with the finite element analysis [69] at a 180° E -plane bend. Dimensions (mm): $a = 19.05$, $b_1 = 5.08$, $b_3 = 4.826$, $\Delta y = 0.0$, $\Delta z = 0.659$, $\theta = 45.0^\circ$ and $s = 6.096$ (cf. Figure 4.9). 92
- FIGURE 4.13** Structure of a compact E -plane T-junction power divider: (a) end view; (b) side view (cf. Figure 1.5(b) for a three-dimensional view of the divider). 93
- FIGURE 4.14** Comparison of this theory with [75] for a simple E -plane T-junction power divider and the effect of moving the step into the resonator region: (a) return loss; (b) insertion loss. Dimensions (mm): $a = 2b_1 = 15.799$, $b_2 = 4.41$, $b_3 = 4.38$, $\Delta y = b_1 - b_2$ and $\theta = 0^\circ$ (cf. Figure 4.13). 95
- FIGURE 4.15** Performance comparison of a single step E -plane T-junction power divider as in [75] with that of a five step where $\Delta y = \Delta z = 0.0$ and $\theta = 18.5^\circ$: (a) return loss; (b) insertion loss. Waveguide dimensions as in Figure 4.14. 96
- FIGURE 4.16** Response of a five step E -plane T-junction power divider achieving a 3 dB crossover for the insertion loss within the performance band: (a) return loss; (b) insertion loss. Dimensions (mm): $a = 2b_1 = 4b_2 = 15.799$, $b_3 = 4.38$, $\Delta y = \Delta z = 0.0$ and $\theta = 18.5^\circ$ (cf. Figure 4.13). 97
- FIGURE 4.17** Configuration and dimensions of a double taper orthomode transducer. 99
- FIGURE 4.18** VSWR of rectangular waveguide orthomode transducer [110]. Dimensions in Figure 4.17. 100
- FIGURE 4.19** Compact orthomode transducer with resonant iris: (a) end view; (b) side view. 101

- FIGURE 4.20** Performance of an optimized five step compact orthomode transducer without a resonant iris. Return loss and insertion loss for (a) TE₁₀ polarization; (b) TE₀₁ polarization. Dimensions (mm): $a_1 = 2a_3 = b_1 = 2b_2 = b_3 = 15.798$ and $\Delta y = \Delta z = 0.0$. 101
- FIGURE 4.21** Performance of an optimized five step compact orthomode transducer with a resonant iris. This formulation including higher order modes at the interfaces (solid and dotted lines), fundamental-mode scattering matrix for junction (dashed lines). Return loss and insertion loss for (a) TE₁₀ polarization; (b) TE₀₁ polarization. Dimensions (mm): $a_1 = 2a_3 = b_1 = 2b_2 = b_3 = 15.798$, $a' = 5.924$, $b' = 11.849$, $l = 1.0$ and $\Delta y = \Delta z = 0.0$ (cf. Figure 4.19). 102
- FIGURE A.1** Cascading two-port scattering matrices. 117
- FIGURE A.2** Cascading a two-port scattering matrix with a homogeneous waveguide of electrical length θ . 118
- FIGURE A.3** Scattering matrix of a two-port discontinuity and its inverse separated by electrical length θ . 119
- FIGURE A.4** Cascading a two-port scattering matrix with that of a three-port. 120
- FIGURE B.1** The cross-sectional dimensions of the rectangular-to-T-septum waveguide discontinuity used for the calculation of the electric field distribution. 122
- FIGURE B.2** The real part of the y-component of the electric field distribution at the rectangular-to-T-septum interface as a function of x at $y=0$. (a) 5 modes; (b) 15 modes. Dimensions: $a/b = 0.5$, $d/b = 0.2$, $t/b = 0.05$, $s/a = 0.5$, and $w/a = 0.25$ (cf. Figure B.1). 123
- FIGURE B.3** The real part of the y-component of the electric field distribution at the rectangular-to-T-septum interface as a function of x at $y=0$. (a) 25 modes; (b) 40 modes. Dimensions: $a/b = 0.5$, $d/b = 0.2$, $t/b = 0.05$, $s/a = 0.5$, and $w/a = 0.25$ (cf. Figure B.1). 124

ACKNOWLEDGMENTS

The author wishes to extend a word of special thanks to his director, Dr. Jens Bornemann, Professor of Electrical Engineering at the University of Victoria. You have inspired and guided me through this whole process and I know that it is your continued confidence and patient support which has made it possible for me to reach this successful conclusion.

Gratitude is extended to the Natural Science Engineering Research Council for its financial support. Their original funding, along with further invaluable sources made possible with the collaboration of Dr. Bornemann through the Department of Electrical Engineering, has made this investigation possible.

I would like also to acknowledge the eminent members of the examining committee who have graciously expended their efforts in proofing and recognizing the contribution to the field that I have here proposed.

To the many friends who have gifted my life since beginning work here in Victoria, I extend also a word of gratitude for the boundless support and encouragement they have offered me in so many different ways.

Finally I thank my parents and family who have never wavered in their steadfast solidarity with me in pursuing my goals, both academic and otherwise. My pursuit of knowledge began at home and those first lessons learned there remain unforgotten: as we continue to explore God's infinite creation, may we always acknowledge Him Who is the source of all knowing and achieving,

Ad Majorem Dei Gloriam.

To
KENNETH E. OLSEN
this dissertation is inscribed,
in affectionate acknowledgment of the blessing
of his true friendship and example

1. OVERVIEW

1.1. INTRODUCTION

In the past twenty years there has been unprecedented growth in the telecommunications industry. Personal mobile communication and the development of a wide array of exciting new technologies in support of the global information network are making increasing demands on research and development in electrical engineering. In particular, there is a constant quest for ever smaller components with improved performance and increasing levels of integration. This, coupled with the need to eliminate costly and time consuming prototype iteration, indicates the development of a new generation of accurate computer-aided analysis and design tools. The impact of all this on microwave technology is significant given its involvement in the telecommunications industry. Reliance on computer-aided analysis to produce superior microwave components will continue to expand, offering exciting new prospects and challenges well into the 21st century.

This research, although of a highly specialized nature, constitutes a significant contribution to the development of such a component design tool for future microwave and satellite communication systems. The principal objective is to develop computer-aided design algorithms for the construction of original and innovative components in an all-metal, but nonstandard, rectangular waveguide technology, and to accomplish this employing accurate electromagnetic field analysis. Since the rectangular waveguide is one of the most popular transmission lines -- due to its wide range of allowable operating specifications (e.g., temperature, pressure, power capabilities, etc.) -- this research will restrict itself to component design for this technology. It should be

noted, however, that the principles presented in this thesis can be applied to other waveguide technologies as well.

Waveguide circuit components for microwave communications systems have certain well-defined design requirements. Besides compactness and low-tolerance specifications, the components must be low loss, light weight, and able to survive and function accurately for extended periods in the physically demanding environments in which they are to operate. To meet these exacting specifications, accurate full-wave analysis and computer-aided design routines for these components are essential.

Such computer routines have been in existence for almost two decades and have achieved a moderate level of maturity. However, most of them in use today rely on closed-form expressions for the electromagnetic fields and, therefore, are only approximate and thus limiting in nature. What would be of particular value today is one that will offer a greater degree of accuracy and be applicable to a wider range of design requirements.

To understand the framework of such computer routines, it is important to review briefly the realization of passive rectangular waveguide components. The development of waveguide components is restricted only by the innovativeness and resourcefulness of design engineers in creating microwave transmission line structures that synthesize the lumped elements employed in corresponding components at lower frequencies. It is well known that this is made necessary by the limitations in size and quality of physical lumped elements at microwave and millimeter wave frequencies. Low frequency lumped elements, for example, capacitors and inductors, are realized at the higher microwave frequencies in waveguide circuit components as obstacles (posts, septums, etc.) or junctions (diaphragms, single plane steps, irises, etc.), collectively known as waveguide discontinuities. As an example, a double-plane step discontinuity in a rectangular waveguide may be used to form a capacitive element in filter design. Hence, all passive waveguide circuit components, in general, may be considered an interconnection of a plurality of waveguide discontinuities. The performance of a component depends on how closely each discontinuity images its corresponding lumped element prototype in the specified frequency range.

In this work the waveguide component design process will consist of discrete discontinuity analyses and, therefore, be described as a 'building block' approach. This approach will be divided into two phases: first, the development of accurate analytic and/or numerical models for electromagnetic fields near waveguide discontinuities and, second, the cascading and combination of these different discontinuities in a unique way to realize circuit components. The first phase of the process establishes a foundation for passive waveguide circuit design; it creates a library of rigorous field descriptions, or building blocks, for various waveguide discontinuities which then are incorporated into the second phase, a cascading algorithm. Naturally, the core of such a library contains the many basic well-known waveguide discontinuities such as the double-plane step or the simple T-junction. However, the desire to engineer smaller waveguide circuit components with improved performance, compounded with fabrication difficulties of standard junction discontinuities at the higher frequencies, has stimulated interest and research efforts to expand this library. Hence, the nucleus of this research is an investigation into junctions formed by waveguides with nonstandard cross-sections that have distinctive propagation characteristics or that exhibit a potential to improve certain component characteristics, such as size. In the second phase these particular nonstandard waveguide discontinuities are incorporated into specific component designs by using conventional cascading algorithms.

Within the two phases, research efforts in computer-aided analysis and design techniques for waveguide components span three major areas, namely, modeling, analysis, and optimization. Notwithstanding the importance of optimization, this research focuses on the first two areas and utilizes existing optimization methods. The next two sections will briefly review the history and current literature on passive microwave circuit components as applied to rectangular waveguide technology. Waveguide discontinuity modeling and analysis will be discussed in Section 1.2 followed by component design in Section 1.3. This review will not be an exhaustive one, as the area under consideration is enormous, but will present significant relevant contributions to the field and indicate how this research is integrated therein. The chapter will conclude with a description of the methodology and organization of the thesis.

1.2. WAVEGUIDE DISCONTINUITIES: MODELING AND ANALYSIS

1.2.1. Theoretical Background

Historically, waveguide discontinuities were modeled by reformulating the electromagnetic field boundary value problem as a microwave equivalent transmission line network. The field in the vicinity of the discontinuity was analyzed, its reactive behaviour determined, and an equivalent reactive network derived. This approach has been invaluable because it allowed a wide range of seemingly complex but practical problems to be solved by conventional network algebraic calculations.

In the literature, electromagnetic characterization of discontinuities began in 1944 when Whinnery and Jamieson [1] published equivalent circuits of several capacitance junction discontinuities (E -plane) in parallel-plate transmission lines. In 1951, Marcuvitz published a text [2] of equivalent circuits for a broad range of waveguide discontinuities that has since become an industry standard. Matthaei, Young and Jones, in 1964, published their definitive handbook [3] on passive waveguide component design based on microwave equivalent network theory.

Since, however, integral transforms and variational techniques were primarily employed [4], the equivalent circuits developed are only valid for dominant mode propagation. This solution is only an approximation and not adequate for the class of multi-discontinuity problems that will be considered here. For example, at discontinuities formed by changes in the waveguide cross-section or joints of different waveguides geometries, it is not possible to satisfy the electromagnetic field boundary conditions dictated by Maxwell's equations employing only the field components of the dominant mode. Below cut-off modes (higher-order modes), observed near the discontinuity by distortion and fringing fields, will be excited. Although they attenuate rapidly due to their below cut-off characteristic, they will cause mode interaction and mode conversion at, for example, a nearby discontinuity. For the design of modern components and systems, it is crucial that these effects be incorporated into the theoretical model. To illustrate, the omission of higher-order mode effects in filter design, can, upon fabrication, result in unanticipated filter responses, such as bandwidth shrinkage, bandpass ripples and considerable frequency shifts.

Over the years, a variety of numerical and analytical methods [5] have been developed for the rigorous theoretical treatment of electromagnetic fields in multi-discontinuity waveguide problems. These methods are, for example, the Finite Element Method (FEM), the Boundary Element Method (BEM), the Finite Difference Method (FD), the Integral Equation Method (IEM), the Method of Moments (MoM), the Transmission Line Matrix Method (TLM) and the Mode-Matching Method (MMM), each with its own unique advantages and disadvantages.

The choice of method employed depends largely on the geometry of the structure itself. When investigating three-dimensional waveguide geometries of arbitrary shape, where the distribution of the electromagnetic field cannot be described in closed form, one must inevitably resort to variational methods such as finite-element [6] or surface/boundary integral formulations [7] because of their universal applicability. An example of this is the commercially available software package, the Hewlett Packard High Frequency Structure Solver (HFSS), which solves for any geometry but needing lengthy CPU time and large memory requirements. For the class of problems in which the components contain discontinuities constructed from fixed boundary cross-sections, whether they be rectangular, circular, elliptical, etc., specific solutions for the electromagnetic fields exist and, therefore, present an advantage in favor of a mode-matching method with respect to CPU time. Therefore, the analytical and numerical method is selected, not only for its ability to solve rigorously a single discontinuity as well as a series of interacting discontinuities, but also for its capability of accomplishing this efficiently using minimal computer time. It can be said, then, that the building block approach, in that it does not require recomputation of propagation characteristics each time the same discontinuity is utilized, is virtually always more time-efficient computationally than the general variational methods mentioned above when computing three-dimensional geometries. It should be noted that this particular type of difficulty with the variational methods has led to the development of frequency domain applications of time domain algorithms; for example, the Finite Difference Time Domain (FD-TD) Method [111] and the Frequency Domain TLM method [112]. Furthermore, a combination method which solves first a two-dimensional problem by a variational method and then the third dimension through mode-matching will be examined in Chapter 3.

In the early 1970's, some of the variational methods that have been applied for a number of years to solve for a single waveguide discontinuity (specifically in equivalent microwave network theory), were expanded to solve for interacting multi-discontinuity waveguide problems [8]. In the multi-modal variational method, an admittance matrix of the discontinuity is developed from its variational, obtained through a self-adjoint operator involving the waveguide eigenmodes, and by using the similarity between field and network theory. Since then, this procedure has been applied to a limited number of rectangular waveguide discontinuities [9-11] and eigenvalue problems [12, 13]. The complete method in its generalized form for both homogeneous and inhomogeneous discontinuities was published in 1991 by Tao and Baudrand [14]. Early claims that the multi-modal variational approach (compared to a mode-matching method) would require smaller matrix sizes for an accurate solution leading to an appreciable reduction in computation time and use of memory space, have not been adequately demonstrated (cf. [14]). This would indicate that the multi-modal variational method does not hold any distinct advantage over mode-matching.

Due to their popularity, the mode-matching methods have matured to a greater degree compared with the expanded variational methods mentioned above and have proven effective in numerous multi-discontinuity problems -- even when complex waveguide cross-section geometries are involved. In 1967, Wexler [15] formalized a modal analysis approach in an attempt to include higher mode influences in discontinuity modeling. In his illustration of the approach on E - and H -plane steps and bifurcations, Wexler claimed that since a mode-matching approach is more direct, i.e., conforms closely to physical reality, the solutions obtained have distinct advantages over other techniques. Subsequently, mode-matching has been successfully applied to a number of common waveguide discontinuities, such as double-plane step junctions [16, 17] and N -furlcations [18].

Generally speaking, in mode-matching, the unknown electromagnetic fields on both sides of the discontinuity are first expanded in terms of their respective modal functions and then matched at the common interface by the application of field continuity conditions [19, 20]. This procedure eventually leads to a set of linear simultaneous equations for the unknown modal coefficients and, hence, the generalized scattering matrix of the discontinuity. In the design algorithm, the Generalized S-matrix

Method [6, 21], which combines the mutual interaction of all discontinuities involved via the dominant and higher-order modes, is used routinely to characterize cascaded and interconnected discontinuities. Mode-matching is universally applied for the component designs in this research.

It is worth noting that the other analysis techniques have been applied to waveguide discontinuity problems, but these suffer from limited applicability and propose no advantage over a mode-matching method. Examples include: a modified residue approach [22], an extended spectral domain method [23], and a boundary-element method [24].

To facilitate a mode-matching method, rectangular waveguide discontinuities may be divided into two basic classifications (cf. Figure 1.1): i) uniaxial two-port junctions and ii) multi-port junctions with a resonator region. Both classifications contain subsets consisting of well-known waveguide discontinuities, e.g., E - and H - plane steps, irises, waveguide bifurcation, double-plane steps, corners, T-junctions, etc., all of which have been extensively investigated and will continue to serve as basic building blocks in component design. However, both classifications also include subsets of nonstandard waveguide discontinuities, and these are the focus of this research. Some nonstandard discontinuities are well established in component design (e.g., round posts and ridge waveguides), but it is worthy to note that there is a virtually limitless field of as yet uninvestigated configurations in which lies a prodigious potential for component designs better suited to modern system specifications.

Two-port junctions formed by waveguides with nonstandard (complex) cross-sections and multi-port junctions with nonstandard (discontinuity-distorted) resonator regions require extensive theoretical and numerical analysis to determine, either the equivalent circuit parameters, or the propagation characteristics of the eigenmodes prior to the application of mode-matching. A well-established nonstandard waveguide discontinuity known as the rectangular-to-ridge, and formed by the fixing of a thin ridge at the top of a rectangular waveguide [cf. Figure 1.2(a)], has been successfully employed in components to improve performance. Since proposed in 1944 [25], the ridge waveguide has been analyzed using many different techniques and is introduced here as the starting point for an investigation of nonstandard waveguide discontinuities. It is

precisely the wealth of information readily available about this waveguide that provides the basis for confidence in the numerical modeling techniques used extensively throughout this research.

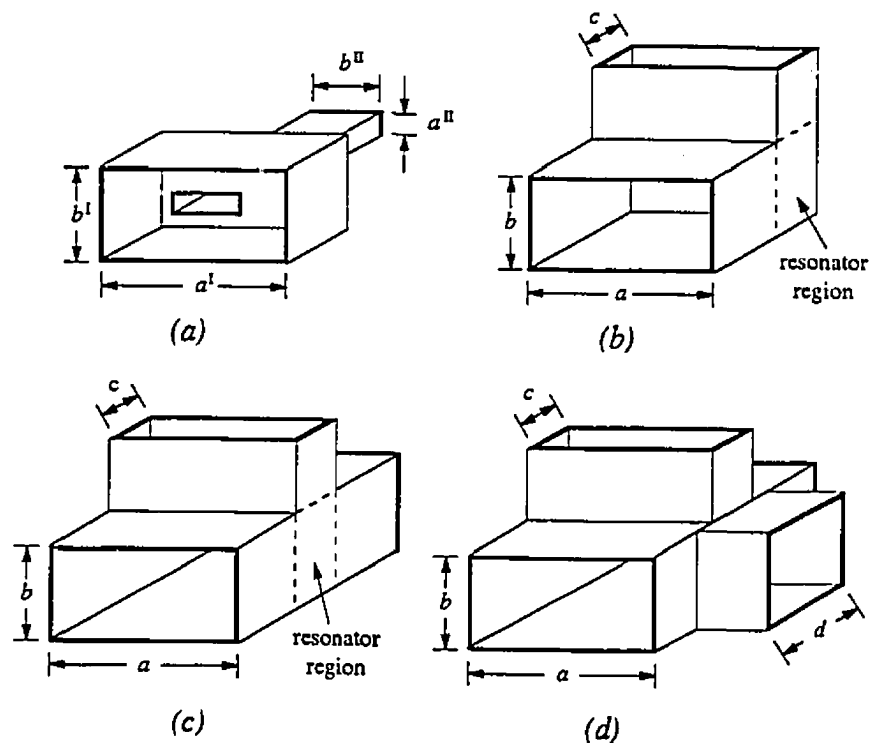


FIGURE 1.1 Examples of standard rectangular waveguide discontinuities: (a) asymmetrical double-plane step waveguide junction (two-port); (b) waveguide corner (two-port); (c) E-plane T-junction (three-port); (d) Magic T (four-port).

The various avenues used to analyze the ridge waveguide for application in a two-port junction discontinuity will be reviewed next, followed by a look at the current status of the analysis of multiports with nonstandard resonator regions. It is an important objective of this thesis to expand the theoretical and numerical analysis of nonstandard two-port discontinuities to include multi-ports.

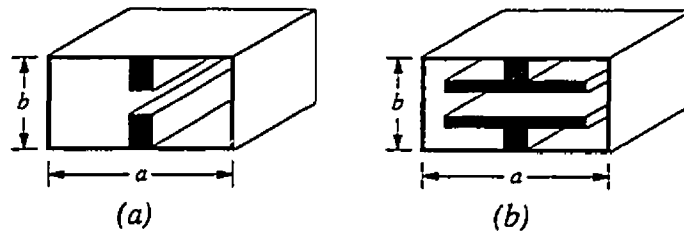


FIGURE 1.2 *Rectangular waveguides with a nonstandard cross-section: (a) double ridge septum; (b) double T-septum.*

1.2.2. Two-Port Junctions with Nonstandard Waveguide Cross-sections

This section will review two nonstandard rectangular waveguide cross-sections: i) the ridge waveguide and ii) the T-septum waveguide. The impact of these cross-sections on component design will be detailed in Section 1.3. The ridge waveguide, originally proposed as a transmission media because of its improved impedance properties and wider bandwidth compared to the standard, has played a significant role in septum technology. The T-septum waveguide is the only exemplar of a nonstandard cross-section used in a two-port junction that will be investigated in this work, however, it should be noted that the analysis is applicable to a wide range of other septum technology.

Compared with a standard waveguide, the ridged guide has better impedance properties and a greater bandwidth of operation, thus offering a higher level of integration leading to smaller components and improved performance. In 1947, Cohn [26], using susceptance values between parallel plates in [1], published ridge waveguide eigenvalues obtained by applying a rudimentary form of the transverse resonance technique [5]. Both Hopfer [27] in 1955 and, later, Anderson [28] in 1956, by employing a quasi-static solution for the susceptance from [2], extended Cohn's work to other aspect ratios. Accurate data for the general range of aspect ratios was published in 1966 by Pyle [29], followed by the complete ridge waveguide eigenvalue spectrum in 1971 by Montgomery [30], who applied an integral eigenvalue equation to obtain his results. Utsumi was able to reduce the computation time necessary to calculate the eigenmodes of the ridge waveguide in 1985 by using a variational analysis [31]. In 1991, Bornemann

published his comparison between standing wave and transverse resonance field matching techniques as applied to the mode-matching of two-port junctions [32]. Currently these appear to be the most effective techniques to obtain the required septum eigenmode spectra for mode-matching and, hence, will be employed exclusively in this work.

Preliminary investigations suggest that T-septum technology may offer impressive potential for improving component design. To enhance septum waveguide propagation characteristics, a T-septum was derived by reshaping the ridge into a "T" [cf. Figure 1.2(b)]. In the literature, analysis has indicated that this structure has a lower dominant mode cut-off frequency [33-35] and a broader bandwidth [36, 37] than that of a ridged waveguide of comparable size. The solution for the cutoff frequency and bandwidth of the dominant mode of a double T-septum presented in [33] was extended to include single T-septum waveguides and then compared to that of its ridge waveguide counterpart in [34]. A theoretical analysis of the complete eigenvalue spectrum with its impedance characteristics is given in [35]. All authors, with the exception of German and Riggs in [36], where the transmission line matrix (TLM) method was employed, formulated an integral eigenvalue equation which was subsequently solved numerically by application of the Ritz-Galerkin method to determine the T-septum waveguide properties.

The attenuation and power-handling capabilities of the T-septum waveguide were subsequently investigated. It can handle less power, but has lower attenuation than the single-ridge guide with identical gap parameters [38]. Dielectric filling of the septum gap increases the cutoff wavelength of the dominant mode and its bandwidth [39], and improves the power handling capability [40], but, unfortunately, increases the losses of the structure. In addition, and unlike the ridge waveguide, the dimensions of the T-septum waveguide may be selected to permit a dual-mode, dual-polarization propagation, i.e., two and only two modes will propagate in a designated frequency interval with equal velocities [41, 42].

1.2.3. Multi-port Junctions with Nonstandard Resonator Regions

Multi-port junctions with a resonator region, such as E -plane and H -plane T-junctions, magic-T's, and waveguide bends, have important applications in many microwave circuits for modern communication systems. As in two-ports, these junctions were initially analyzed using equivalent circuit models [2]. However, as stated earlier, equivalent circuits are only approximate solutions and do not give sufficiently accurate results for many applications; therefore, rigorous field solutions are being sought.

From the mode-matching perspective, multi-port junctions always contain a region, commonly referred to as the resonator region, where the electromagnetic fields cannot be expanded in natural eigenmodes and therefore one cannot apply mode-matching directly. This difficulty, best illustrated in the analysis of the T-junction, has been resolved in a variety of different manners. One of these, introduced in 1967, applied equivalent-circuit concepts to waveguide modes [43], where the admittance matrix was calculated by successively placing short circuits exactly at two of the three openings, yielding three one-ports consisting of shorted uniform waveguides. This strategy was generalized for mode matching of resonator type circuits in 1973 [44]. A three-plane mode-matching technique, where a short circuit is placed in three different positions on the side arm of a T-junction, was introduced in 1991 [45]. Recently, in 1992, Sieverding and Arndt [46], based on [44], published a complete rigorous analysis of the general rectangular T-junction. However, among the works published to date, none has rigorously solved and obtained the generalized scattering matrix for a multi-port junction with a nonstandard resonator region. This thesis proposes a full-wave solution, by expanding the principles of the two-port theory, to T-junctions that are distorted by discontinuities within the resonator region (cf. Figure 1.3).

It should be noted that variational methods, such as the finite element method and the boundary element method, have been successfully applied to T-junctions and waveguide corners but, as in two-port junctions, require considerable computing efforts when compared to the mode-matching method [47].

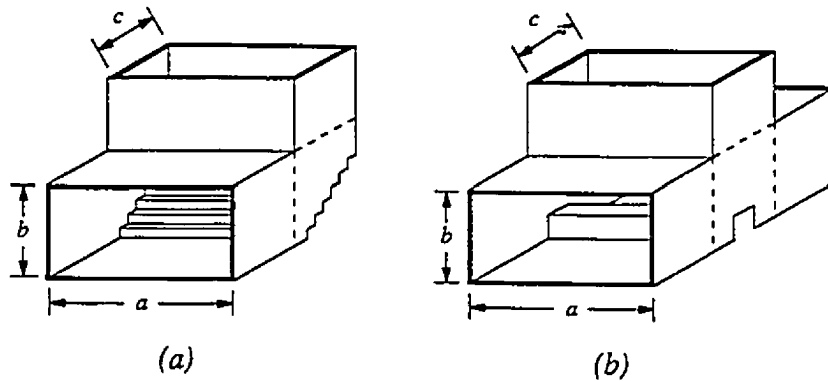


FIGURE 1.3 Examples of multi-ports junctions with a nonstandard resonator region: (a) stepped mitered waveguide corner; (b) ridged E-plane T-junction.

1.3. PASSIVE MICROWAVE RECTANGULAR WAVEGUIDE COMPONENTS

A wide range of two-port and multi-port components have been realized by cascading junction type discontinuities in rectangular waveguide technology. Two-port components based on the ridge waveguide are discussed next, and this is followed by a discussion of multi-port components. Special attention will be given to the analytical and numerical techniques employed for the solution of the basic building block discontinuity.

1.3.1. Two-Port Components

Many components have been designed using common two-port junctions. Some pertinent examples are: the utilization of single and double-plane steps and bifurcations as building block discontinuities in i) E -plane and resonant-iris filters [48-51], ii) impedance transformers [52, 53], iii) phase shifters and 180° couplers [54, 54], iv) polarizers [56-58], and v) corrugated waveguides [59] leading to applications in horn antennas and feeders. With the exception of applying a residue-calculus technique in [50, 51] and the Wiener-Hopf method in [56], the majority of design analyses were based on a mode-matching method.

As indicated earlier, the nonstandard cross-section of the ridge waveguide

has improved component design. The amount of cutoff frequency reduction, compared to a ridgeless rectangular waveguide, made the ridge septum ideal as a capacitive element for application in evanescent-mode filters [60-63]. Not only do these evanescent-mode filters have several advantages over conventional filters, such as sharper transition to out-of-band rejection, wider stopbands, and compactness, but also, they may be fabricated at millimeter-wave frequencies where the other capacitive elements, such as screws and round posts, are too large. Theoretical and numerical analyses were based on the Generalized S-matrix Method in conjunction with a spectral-domain approach or a mode-matching method to formulate the modal scattering matrix of the waveguide-to-ridge-waveguide discontinuity.

The viable use of ridge waveguide technology in impedance transformers has been well demonstrated. The experimental and empirical design procedure of Hensperger [64] was employed by Bornemann and Arndt [61, 65], using mode-matching and the Generalized S-matrix Method to optimize the stepped transitions for both the ridges and the different outer cross-sections from the input waveguide to the smaller housing of the ridged waveguide. This combined the advantage of stepped constant thickness ridges with that of the additional matching potential achieved by varying cross-section dimensions to obtain improved return loss behavior and a compactness not possible with empirical procedures alone.

To date, there are no published results using the T-septum waveguide in passive microwave circuit component design. It will be demonstrated that use of the T-septum can significantly ameliorate current ridge waveguide circuit components; for example, the reduction in cutoff frequency should contribute to the development of smaller and lighter components. This research produces designs for two two-port components in T-septum technology: filters and transformers (cf. Figure 1.4).

1.3.2. Waveguide Corners and Three-port Components

Waveguide Corners are not components in the strict sense but are used extensively in microwave communications where long waveguide runs are required, such as in antenna feed systems. Because they include a resonator region with analysis similar to the T-junction, they require extensive numerical modeling. Using integral transforms,

non-mitered H -plane and E -plane bends were first analyzed and equivalent circuits presented in [2]. Several others have attempted to expand this work meeting with varying degrees of success. Lewin attempted to do so in [66]. Campbell and Jones in [67] extended the model to include an E -plane waveguide with mitered corner. The mode-matching method was applied successfully to a non-mitered 90-degree E -plane corner in [68]. All of these attempts were limited to waveguides with the same size input as output port. Using the finite element method, the calculated return loss of a wide selection of mitered waveguide bends for angles between 20° and 90° inclusive have been published in [69]. This thesis will propose a mode-matching method with a computational efficiency advantage unmatched by the finite element method for stepped approximations of mitered 90- and 180-degree bends.

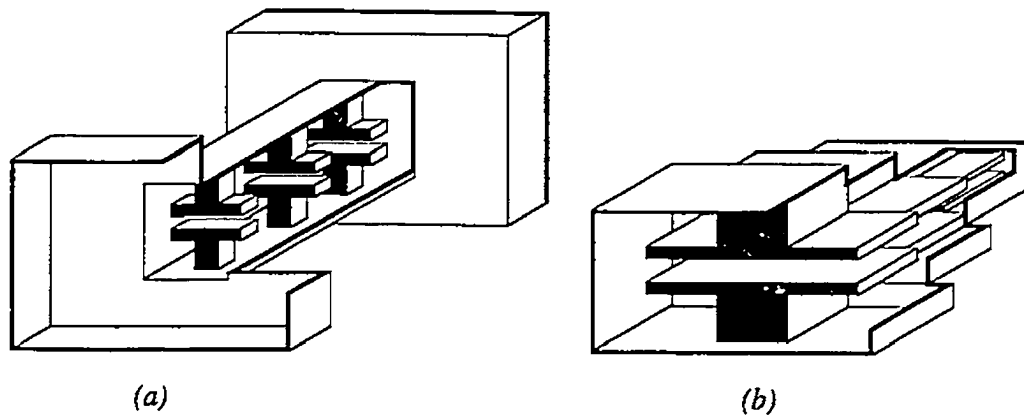


FIGURE 1.4 (a) *Evanescent-mode T-septum filter*; (b) *stepped T-septum transformer*.

The T-junction is fundamental in many three-port waveguide components, such as bandstop resonator cavity filters [3], multiplexers [70-74], power-dividers [75], orthomode transducers [76], and couplers [77]. By distorting the resonator region of the T-junction with discontinuities, new components will be proposed which will improve the performance of well-known designs and, of equal significance, contribute to their reduction in size (cf. Figure 1.5).

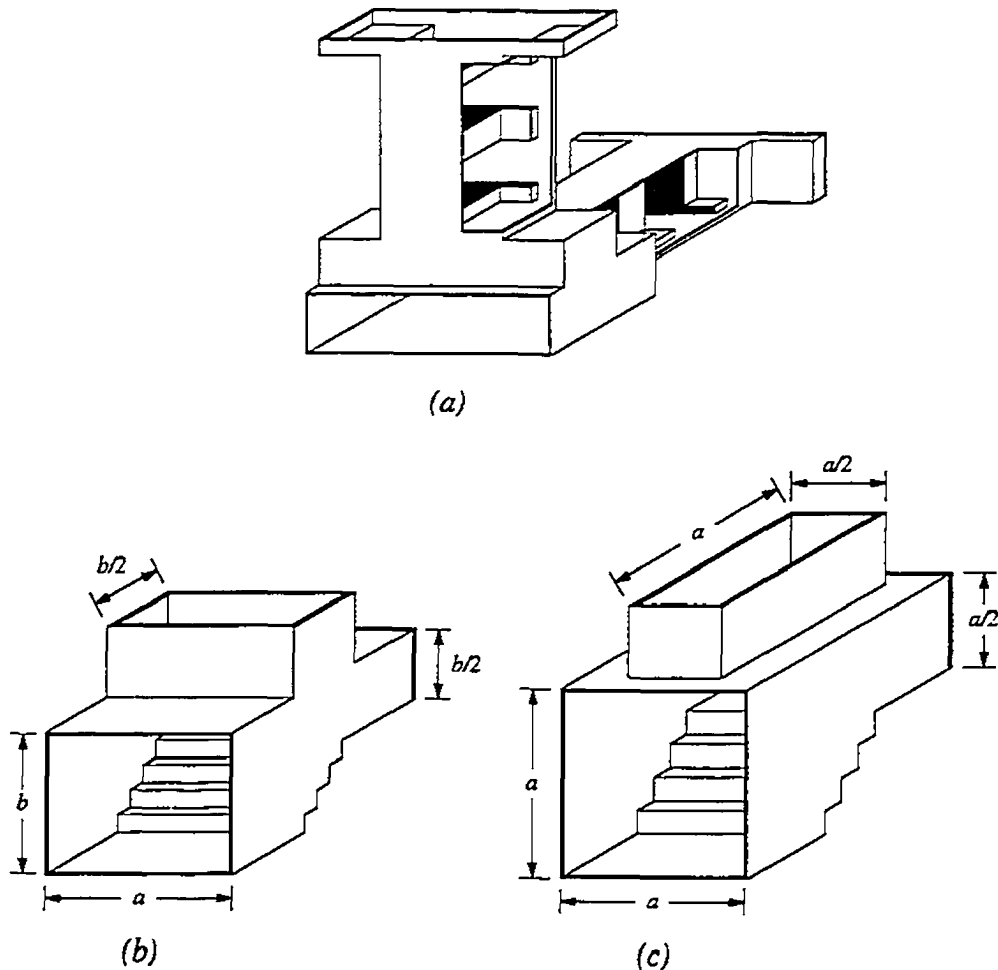


FIGURE 1.5 (a) *Integrated T-septum diplexer*; (b) *compact power divider*; (c) *compact orthomode transducer*.

1.4. METHODOLOGY AND ORGANIZATION

As already mentioned, this research will follow a two phase approach to the development of rectangular waveguide component design algorithms. The theoretical treatment of a waveguide discontinuity will be presented, followed by an array of components which then incorporate that discontinuity. No attempt will be made to exhaust the field of components made possible by using a particular waveguide discontinuity but only to present a few design examples to support the applicability of

each. Chapter 2 will present the particular mode-matching method selected and applied to the double-plane step and the simple E -plane T-junction. Chapter 3 will introduce the eigenvalue spectrum and propagation characteristics of the T-septum waveguide. Once the rectangular-to-T-septum waveguide discontinuity is solved, various filters and transformers can be designed. Two filter designs will be combined with a simple E -plane T-junction to produce a compact T-septum diplexer. The theoretical treatment of a T-junction with a discontinuity-distorted resonator region, and its application to mitered waveguide bends and other three-port components, will be the topic of Chapter 4.

Throughout the thesis, a unified theoretical and experimental approach has been used. The numerical models and procedures developed were tested and debugged using the Faculty of Engineering's SUN systems environment. An IBM 6000/530 RISC Station equipped with a next-generation Fortran compiler with extended precision capabilities was available for production jobs with full matrix size utilization. Component prototypes have been built and tested in the microwave laboratory at the University of Victoria in order to verify the numerical models developed. The Laboratory is a fully equipped facility with signal generators, spectrum analyzers, and scalar and vector network analyzers; the measurement capability covers a range from 10 MHz to 110 GHz.

2. THE MODE-MATCHING METHOD

2.1. INTRODUCTION

Among the variety of numerical and analytical methods that have been applied to investigate waveguide circuits, the mode-matching method has been preferred where the structures in question have fixed boundary cross-sections with discontinuities in the direction of propagation. Since the method was first applied in the 1940's, certain advantages have been discerned. First and most important, the mode-matching method inherently includes higher-order mode excitations at the discontinuity, thus accounting for the contributions of evanescent TE and TM modes to the overall electromagnetic field [78]. Second, it may be applied easily in conjunction with other numerical techniques, such as the standing wave formulation and transverse resonance methods [61] which are employed to solve for a waveguide's propagation constants, cutoff frequencies, or characteristic impedances. Third, the modal scattering matrix obtained is cascaded effortlessly with other scattering matrices of adjacent discontinuities by the Generalized S-matrix Method [6]. The Generalized S-matrix Method combines the mutual interaction of two discontinuities by the inclusion of dominant and higher modes. Fourth, mode-matching is applicable to the resonator regions of multi-port passive microwave components such as T-junctions and couplers [44].

There are, however, two distinct disadvantages to the method. One is the phenomenon of relative convergence, i.e., convergence to the correct solution is not always ensured by increasing the number of modes. The second is that large matrix sizes are generated tending to extend numerical computation time. Solutions to these disadvantages are being sought; it has been reported, for example, that taking the ratio of

the number of modes in each region to correspond to the surface area ratio prevents relative convergence problems [79, 80]. Matrix size reduction is possible by including field symmetries or, in special cases, by neglecting field components of minor influence, for example, in [81].

It should be noted that the Conservation of Complex Power Technique, initially proposed by Safavi-Naina and MacPhie [82], to solve waveguide junction scattering problems is mathematically identical to the mode-matching procedure presented in this chapter and offers no new knowledge. The admittance matrix formulation proposed in [83] does eliminate two matrix inversions as compared to the Generalized S-matrix Method but fails in the case of discontinuities of vanishing length.

After a synopsis of the mode-matching method, this chapter analyzes two configurations, namely the double-plane step and the E -plane T-junction, to demonstrate this modal expansion technique and to serve as a bridge to a discussion of nonstandard multi-ports in Chapters 3 and 4.

2.2. THEORETICAL BACKGROUND

The mode-matching method is limited to the orthogonal coordinate systems in Euclidean 3-space because general solutions of Maxwell's electromagnetic field equations are constructed by the separation of variables [84]. In particular, the solution to the electromagnetic field in an homogeneous source-free waveguide is derived from the electric and magnetic vector potentials \vec{A} and \vec{F} , respectively:

$$\begin{aligned}\vec{E} &= -\nabla \times \vec{F} + \frac{1}{j\omega\epsilon} \nabla \times \nabla \times \vec{A} \\ \vec{H} &= \nabla \times \vec{A} + \frac{1}{j\omega\mu} \nabla \times \nabla \times \vec{F}\end{aligned}\tag{2-1}$$

where the angular frequency $\omega = 2\pi f$, ϵ and μ are the permittivity and permeability of the medium, respectively, and $j = \sqrt{-1}$ [2]. The components of \vec{A} and \vec{F} are chosen such that they have non-vanishing components only in the longitudinal direction of the waveguide, and hence, satisfy a separable Helmholtz partial differential equation.

For example, in a waveguide with its axis parallel to the z -coordinate, the field is readily divided into a sum of TE_z and TM_z fields by choosing the longitudinal components of \vec{A} and \vec{F} , denoted by ψ^e and ψ^m , respectively. The scalar wave potentials ψ^e and ψ^m are solutions to the Helmholtz equation which, when partially separated, have the general form:

$$\begin{aligned}\psi^e(x, y, z) &= \sum_{p=1}^{\infty} \sqrt{Z_p^e} \Psi_p^e(x, y) \zeta_p^e(z) \\ \psi^m(x, y, z) &= \sum_{q=1}^{\infty} \sqrt{Y_q^m} \Psi_q^m(x, y) \zeta_q^m(z)\end{aligned}\quad (2-2)$$

where Z^e and Y^m are the wave impedances and admittances, respectively. The cross-section eigenfunctions $\Psi^{e,m}$ are solutions to the boundary value problem

$$\begin{aligned}\nabla_{\perp}^2 \Psi^{e,m} + k_c^2 \Psi^{e,m} &= 0 \quad \text{in the waveguide} \\ \left. \begin{aligned} \frac{\partial \Psi^e}{\partial n} &= 0 \\ \Psi^m &= 0 \end{aligned} \right\} &\text{on the metallic surface}\end{aligned}\quad (2-3)$$

where the derivative is taken in a direction normal to the waveguide surface. The functions $\zeta^{e,m}$, which generally contain two unknown coefficients, are solutions to the second-order ordinary differential equation

$$\frac{d^2 \zeta}{dz^2} + k_c^2 \zeta = 0. \quad (2-4)$$

The cut-off wave numbers k_c are related to the propagation constants k_z by

$$k_c^2 + k_z^2 = k^2 \quad (2-5)$$

where $k^2 = \omega^2 \mu \epsilon$. The indices p and q in eq.(2-2) are ordered in increasing mode cut-off frequencies. The propagation constants are determined from eq.(2-5) after the cut-off wave numbers are found by solving the boundary value problem.

When applying the mode-matching method to a waveguide discontinuity problem, the junction is subdivided into suitable regions, such that eigenfunction

expansions can be calculated for the cross-sections of each subregion. Once solutions for eqs.(2-3) and eq.(2-4) are determined in each subregion, the results are substituted into eqs.(2-1) to obtain electromagnetic field expressions. Then, by matching the tangential field components at common interfaces between the subregions and utilizing the orthogonal property of the cross-section eigenfunctions [85], an infinite set of mode-matching equations is generated. In order to obtain a useful numerical result, this set of equations must be truncated and solved. The unknown amplitude coefficients may now be related to each other by the desired modal scattering matrix of the junction. The accuracy of the representation to the actual electromagnetic field within a waveguide is dependent on the number of eigenfunctions (or modes) included to demonstrate convergence.

The waveguide modal spectrum of the electromagnetic field \vec{E} and \vec{H} propagating in the $+z$ -direction is written in matrix form [c.f. eqs. (2-1)]:

$$\begin{aligned} \vec{E}(x, y, z) &= [\vec{e}_T^e \mid \vec{e}_T^m + e_z^m \hat{u}_z] \cdot \left[\begin{array}{c|c} \text{diag}(\sqrt{Z_p^e}) & \mathbf{0} \\ \hline \mathbf{0} & \text{diag}(\sqrt{Z_q^m}) \end{array} \right] \cdot \left[\begin{array}{c|c} \text{diag}(\exp(-jk_z^e z)) & \mathbf{0} \\ \hline \mathbf{0} & \text{diag}(\exp(-jk_z^m z)) \end{array} \right] \cdot \begin{bmatrix} A_p^e \\ A_q^m \end{bmatrix} \\ \vec{H}(x, y, z) &= [\vec{h}_T^e + h_z^e \hat{u}_z \mid \vec{h}_T^m] \cdot \left[\begin{array}{c|c} \text{diag}(\sqrt{Y_p^e}) & \mathbf{0} \\ \hline \mathbf{0} & \text{diag}(\sqrt{Y_q^m}) \end{array} \right] \cdot \left[\begin{array}{c|c} \text{diag}(\exp(-jk_z^e z)) & \mathbf{0} \\ \hline \mathbf{0} & \text{diag}(\exp(-jk_z^m z)) \end{array} \right] \cdot \begin{bmatrix} A_p^e \\ A_q^m \end{bmatrix} \end{aligned} \quad (2-6)$$

where $A^{e,m}$ is the amplitude of the forward traveling wave as a solution to eq.(2-4) and the submatrices span the appropriate number of TE_z and TM_z modes, i.e., $p = 1, 2, \dots, n^e$ and $q = 1, 2, \dots, n^m$. The elements of the mode functions in eq.(2-6) are

$$\begin{aligned}
 \vec{e}_{T_p}^e &= \hat{u}_z \times \nabla_z \Psi_p^e & \vec{e}_{T_q}^m &= -\nabla_z \Psi_p^e \\
 \vec{h}_{T_p}^e &= -\nabla_z \Psi_q^m & \vec{h}_{T_q}^m &= -\hat{u}_z \times \nabla \Psi_q^m \\
 h_{z_p}^e &= \frac{(k_c^2)_p}{jk_{z_p}^e} \Psi_p^e & e_{z_q}^m &= \frac{(k_c^2)_q}{jk_{z_q}^m} \Psi_q^m
 \end{aligned}
 \tag{2-7}$$

Since the z direction is arbitrary, the electromagnetic field may be represented in any waveguide in a corresponding manner by choosing the appropriate longitudinal components of \vec{A} and \vec{F} and satisfying eqs.(2-3) and eq.(2-4).

2.3. TWO-PORT WAVEGUIDE JUNCTION: A DOUBLE-PLANE STEP

This section presents the basic procedure for applying the mode-matching method and obtaining the generalized modal scattering matrix for the double-plane step discontinuity formed by connecting two rectangular waveguides of differing cross-sections. The derivation of this scattering matrix is well known and has been presented in a number of papers, e.g., [81]. With the exception of the cross-section eigenfunctions, the equations presented here are valid for all two-port waveguide junctions.

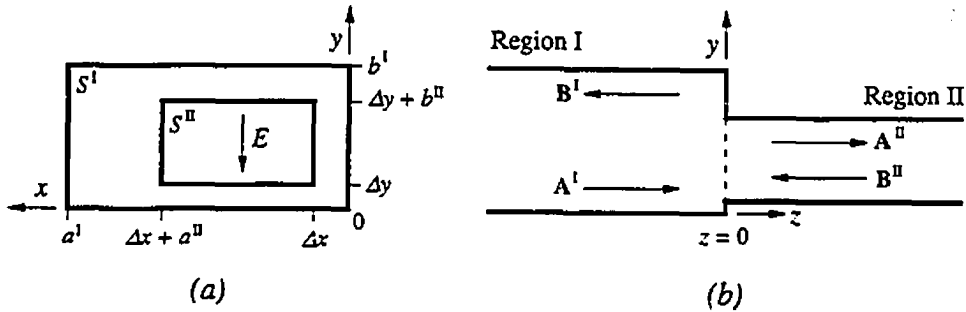


FIGURE 2.1 Double-plane step discontinuity: (a) end view; (b) side view. (cf. Figure 1.1 for a three-dimensional view)

Figure 2.1 depicts the double-plane step discontinuity subdivided into two cross-sectional regions denoted by I and II. The solutions to the Helmholtz equation for each region, $i = I$ and II, are

$$\begin{aligned}
\Psi^{ei}(x, y, z) &= \sum_{p=1}^{n^i} \sqrt{Z_p^{ei}} \Psi_p^{ei}(x, y) \left\{ A_p^{ei} \exp(-jk_z^{ei} z) + B_p^{ei} \exp(+jk_z^{ei} z) \right\} \\
\Psi^{mi}(x, y, z) &= \sum_{q=1}^{n^m} \sqrt{Y_q^{mi}} \Psi_q^{mi}(x, y) \left\{ A_q^{mi} \exp(-jk_z^{mi} z) - B_q^{mi} \exp(+jk_z^{mi} z) \right\}
\end{aligned} \tag{2-8}$$

where $A^{ei,mi}, B^{ei,mi}$ are the amplitudes of the forward and backward traveling waves of the TE_z and TM_z modes, respectively. The cross-section eigenfunctions are the well-known rectangular waveguide modes

$$\begin{aligned}
\Psi_{mn}^{ei}(x, y) &= C_{mn}^i \cos\left(\frac{m\pi}{a^i}(x - \Delta x_i)\right) \cos\left(\frac{n\pi}{b^i}(y - \Delta y_i)\right) \\
\Psi_{mn}^{mi}(x, y) &= D_{mn}^i \sin\left(\frac{m\pi}{a^i}(x - \Delta x_i)\right) \sin\left(\frac{n\pi}{b^i}(y - \Delta y_i)\right)
\end{aligned} \tag{2-9}$$

where $m, n = 0, 1, 2, \dots$, ($m = n = 0$ excepted) and a, b are the waveguide dimensions. The TE_z and TM_z modes are ordered in increasing cut-off frequencies, i.e., $m, n \rightarrow p, m, n \rightarrow q$ for region I and $m, n \rightarrow r, m, n \rightarrow s$ for region II. The coefficients C and D are then normalized by

$$\iint_{S^i} [\nabla \Psi^{ei,mi}]^2 ds = 1 \tag{2-10}$$

so that the power carried by a mode through the cross-section S^i is

$$P^{ei,mi} = \begin{cases} 1W & \text{for propagating modes} \\ +j1W & \text{for evanescent TE modes} \\ -j1W & \text{for evanescent TM modes} \end{cases} \tag{2-11}$$

if the corresponding wave amplitude equals $1/\sqrt{W}$.

To apply the field continuity equations, the tangential field components for each subregion are extracted from eq.(2-6), and equated:

$$\left. \begin{aligned} \bar{\mathbf{E}}_T^I &= \bar{\mathbf{E}}_T^II & \text{on } S^I \\ \bar{\mathbf{E}}_T^I &= 0 & \text{on } S^I \cap S^{II} \\ \bar{\mathbf{H}}_T^I &= \bar{\mathbf{H}}_T^II & \text{on } S^{II} \end{aligned} \right\} \text{at } z = 0. \tag{2-12}$$

Integrating over interfaces S^I and S^{II} , while using the orthogonal property of the respective cross-section eigenfunctions, will yield the modal scattering matrix of the discontinuity

$$\begin{bmatrix} \mathbf{B}^I \\ \mathbf{A}^{II} \end{bmatrix} = \begin{bmatrix} \mathbf{S}_{11} & \mathbf{S}_{12} \\ \mathbf{S}_{21} & \mathbf{S}_{22} \end{bmatrix} \cdot \begin{bmatrix} \mathbf{A}^I \\ \mathbf{B}^{II} \end{bmatrix} \quad (2-13)$$

where

$$\begin{aligned} \mathbf{S}_{11} &= -[\mathbf{I} + \mathbf{M}\mathbf{M}^T]^{-1}[\mathbf{I} - \mathbf{M}\mathbf{M}^T] \\ \mathbf{S}_{12} &= 2[\mathbf{I} + \mathbf{M}\mathbf{M}^T]^{-1}\mathbf{M} \\ \mathbf{S}_{21} &= \mathbf{M}^T[\mathbf{I} - \mathbf{S}_{11}] \\ \mathbf{S}_{22} &= \mathbf{I} - \mathbf{M}^T\mathbf{S}_{12} \end{aligned} \quad (2-14)$$

and

$$\mathbf{M} = \text{diag}\left(\sqrt{Y_{p,q}^{eI,mI}}\right) \begin{bmatrix} \mathbf{M}^{eI-eII} & \mathbf{0} \\ \mathbf{M}^{mI-eII} & \mathbf{M}^{mI-mII} \end{bmatrix} \text{diag}\left(\sqrt{Z_{r,s}^{eII,mII}}\right) \quad (2-15)$$

In eqs.(2-14) and (2-15), \mathbf{I} is the unit matrix, T means transpose, and 'diag' denotes a diagonal matrix. The elements of the coupling matrices in eq.(2-15) are

$$\begin{aligned} M_{pr}^{eI-eII} &= \iint_{S^II} (\hat{u}_z \times \nabla_z \Psi_p^{eI}) \cdot (\hat{u}_z \times \nabla_z \Psi_r^{eII}) ds \\ M_{qr}^{mI-eII} &= \iint_{S^II} (-\nabla_z \Psi_q^{mI}) \cdot (\hat{u}_z \times \nabla_z \Psi_r^{eII}) ds \\ M_{qs}^{mI-mII} &= \iint_{S^II} (-\nabla_z \Psi_q^{mI}) \cdot (-\nabla_z \Psi_s^{mII}) ds \end{aligned} \quad (2-16)$$

The scattering matrix of any singular discontinuity thus obtained may be combined with any number of similar scattering matrices by using the generalized scattering matrix cascading algorithms which can be found in Appendix A.

2.4. THREE-PORT WAVEGUIDE JUNCTION: AN *E*-PLANE T-JUNCTION

The structure of an *E*-plane T-junction, depicted in Figure 2.2, is the interconnection of three rectangular waveguides. To formulate the electromagnetic field representation of the junction, the configuration is first subdivided into the cross-sectional regions I, II, III, and IV. Region IV forms the resonator region connected to the three waveguides I through III. The presentation of the problem here is similar to one already published by Sieverding and Arndt [46]. The admittance matrix formulation, which is a variation of this solution, is presented in [86].

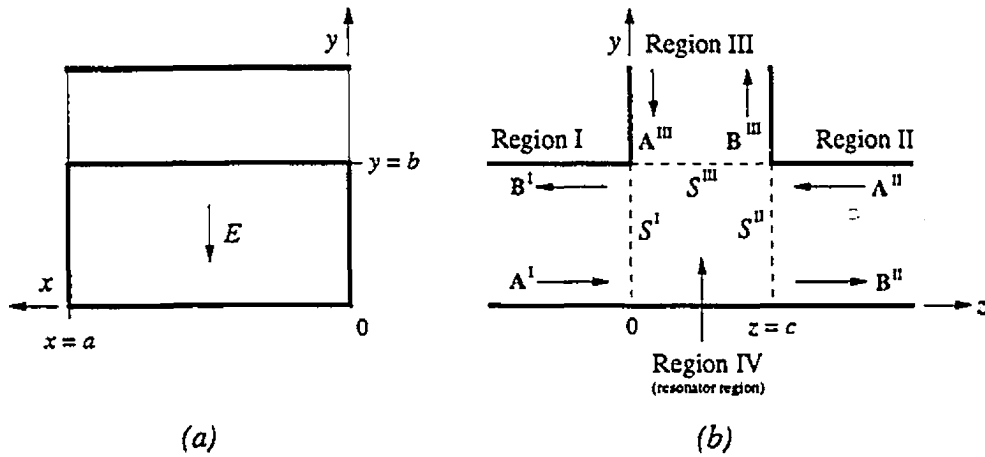


FIGURE 2.2 Simple *E*-plane T-junction of three rectangular waveguides: (a) end view; (b) side view. (cf. Figure 1.1 for a three-dimensional view)

For waveguides I, II, and III, the longitudinal components of the vector potentials are chosen as

$$\begin{aligned}
 \bar{F}^I &= \hat{u}_z \psi^{eI}(x, y, z) & \bar{A}^I &= \hat{u}_z \psi^{mI}(x, y, z) \\
 \bar{F}^{II} &= \hat{u}_z \psi^{eII}(x, y, z) & \bar{A}^{II} &= \hat{u}_z \psi^{mII}(x, y, z) \\
 \bar{F}^{III} &= \hat{u}_z \psi^{eIII}(x, y, z) & \bar{A}^{III} &= \hat{u}_z \psi^{mIII}(x, y, z)
 \end{aligned}
 \tag{2-17}$$

where $\psi^{e,m}$ and $\phi^{e,m}$ are the wave potentials given by the general form of eq.(2-2), with appropriate traveling wave amplitude shown in Figure 2.2. The wave potential $\phi^{e,m}$ in

region III is a simple cyclic interchange of x, y, z on $\psi^{e,m}$. Using the cross-section functions of a rectangular waveguide [i.q. eqs.(2-9)], the expressions for the fields in waveguides I to III can be composed.

The electromagnetic field in the resonator region is composed of three solutions, corresponding to the number of apertures. These are found by applying the principle of superposition to the non-homogeneous boundary conditions of the Helmholtz equation. That is, the solution is a sum of the three functions $\psi^{eIV,mIV(1)}$, $\psi^{eIV,mIV(2)}$, and $\phi^{eIV,mIV(3)}$ satisfying eqs.(2-3) and eq.(2-4) where solution (1) is obtained if short circuits are introduced in the boundary planes S^{II} and S^{III} , and S^{I} remains open; solutions (2) and (3) are found analogously:

$$\begin{aligned}\bar{F}^{\text{IV}} &= \hat{u}_z \left(\psi^{eIV(1)}(x, y, z) + \psi^{eIV(2)}(x, y, z) \right) + \hat{u}_y \phi^{eIV(3)}(x, y, z) \\ \bar{A}^{\text{IV}} &= \hat{u}_z \left(\psi^{mIV(1)}(x, y, z) + \psi^{mIV(2)}(x, y, z) \right) + \hat{u}_y \phi^{mIV(3)}(x, y, z)\end{aligned}\quad (2-18)$$

Hence,

$$\begin{aligned}\psi^{eIV,mIV(1)} &= \sum_{p,q=1}^{n^{\text{I}},n^{\text{II}}} \sqrt{Z_p^{\text{I}}, Y_q^{\text{mI}}} \Psi_{p,q}^{eI,mI}(x, y) A_{p,q}^{eIV,mIV(1)} \begin{Bmatrix} \sin(k_{zp}^{\text{eI}}(z-c)) \\ \cos(k_{zq}^{\text{mI}}(z-c)) \end{Bmatrix} \\ \psi^{eIV,mIV(2)} &= \sum_{r,s=1}^{n^{\text{II}},n^{\text{III}}} \sqrt{Z_r^{\text{II}}, Y_s^{\text{mII}}} \Psi_{r,s}^{eII,mII}(x, y) A_{r,s}^{eIV,mIV(2)} \begin{Bmatrix} \sin(k_{zr}^{\text{eII}}z) \\ \cos(k_{zs}^{\text{mII}}z) \end{Bmatrix} \\ \phi^{eIV,mIV(3)} &= \sum_{t,u=1}^{n^{\text{III}},n^{\text{I}}} \sqrt{Z_t^{\text{III}}, Y_u^{\text{mIII}}} \Phi_{t,u}^{eIII,mIII}(x, z) A_{t,u}^{eIV,mIV(3)} \begin{Bmatrix} \sin(k_{yt}^{\text{eIII}}y) \\ \cos(k_{yu}^{\text{mIII}}y) \end{Bmatrix}\end{aligned}\quad (2-19)$$

Applying the continuity condition for the electric field

$$\begin{aligned}\bar{\mathbf{E}}_T^{\text{I}} &= \bar{\mathbf{E}}_T^{\text{IV}(1)} + \bar{\mathbf{E}}_T^{\text{IV}(2)} + \bar{\mathbf{E}}_T^{\text{IV}(3)} \\ &= \bar{\mathbf{E}}_T^{\text{IV}(1)} + \mathbf{0} + \mathbf{0}\end{aligned}\quad \left. \vphantom{\bar{\mathbf{E}}_T^{\text{I}}} \right\} \text{at } z=0 \quad (2-20)$$

yields the following relationship for the unknown amplitudes in the resonator region

$$A_{p,q}^{eIV,mIV(1)} = -\delta^{e,m} \left(\frac{A_{p,q}^{eI,mI} + B_{p,q}^{eI,mI}}{\sin(k_{zp,q}^{\text{eI}}c)} \right) \quad (2-21)$$

where $\delta^e = 1$ and $\delta^m = j$. Similarly, applying the two electric field continuity equations at the remaining apertures will produce

$$\begin{aligned} A_{r,s}^{eIV,mIV(2)} &= \delta^{e,m} \left(\frac{A_{r,s}^{eII,mII} + B_{r,s}^{eII,mII}}{\sin(k_{zr,zs}^{eII,mII} c)} \right) \\ A_{t,u}^{eIV,mIV(3)} &= \delta^{e,m} \left(\frac{A_{t,u}^{eIII,mIII} + B_{t,u}^{eIII,mIII}}{\sin(k_{yt,yu}^{eIII,mIII} b)} \right) \end{aligned} \quad (2-22)$$

The continuity equations for the magnetic fields are

$$\begin{aligned} \bar{\mathbf{H}}_T^I &= \bar{\mathbf{H}}_T^{IV(1)} + \bar{\mathbf{H}}_T^{IV(2)} + \bar{\mathbf{H}}_T^{IV(3)} \text{ at } z = 0 \\ \bar{\mathbf{H}}_T^{II} &= \bar{\mathbf{H}}_T^{IV(1)} + \bar{\mathbf{H}}_T^{IV(2)} + \bar{\mathbf{H}}_T^{IV(3)} \text{ at } z = c \\ \bar{\mathbf{H}}_T^{III} &= \bar{\mathbf{H}}_T^{IV(1)} + \bar{\mathbf{H}}_T^{IV(2)} + \bar{\mathbf{H}}_T^{IV(3)} \text{ at } y = b \end{aligned} \quad (2-23)$$

which, when matched and integrated over S^I , S^{II} and S^{III} , lead to the matrix equation

$$\begin{aligned} \left[\begin{array}{c|c|c} -\mathbf{I} + \text{diag}\{j \cot(k_{zr,zs}^{eI,mI} c)\} & -\text{diag}\{j \csc(k_{zr,zs}^{eII,mII} c)\} & +\mathbf{K}^{I-III} \\ \hline -\text{diag}\{j \csc(k_{zr,zs}^{eI,mI} c)\} & -\mathbf{I} + \text{diag}\{j \cot(k_{zr,zs}^{eII,mII} c)\} & -\mathbf{K}^{II-III} \\ \hline +\mathbf{K}^{III-I} & -\mathbf{K}^{III-II} & -\mathbf{I} + \text{diag}\{j \cot(k_{yt,yu}^{eIII,mIII} b)\} \end{array} \right] \begin{bmatrix} \mathbf{B}^I \\ \mathbf{B}^{II} \\ \mathbf{B}^{III} \end{bmatrix} = \\ \left[\begin{array}{c|c|c} -\mathbf{I} - \text{diag}\{j \cot(k_{zr,zs}^{eI,mI} c)\} & +\text{diag}\{j \csc(k_{zr,zs}^{eII,mII} c)\} & -\mathbf{K}^{I-III} \\ \hline +\text{diag}\{j \csc(k_{zr,zs}^{eI,mI} c)\} & -\mathbf{I} - \text{diag}\{j \cot(k_{zr,zs}^{eII,mII} c)\} & +\mathbf{K}^{II-III} \\ \hline -\mathbf{K}^{III-I} & +\mathbf{K}^{III-II} & -\mathbf{I} - \text{diag}\{j \cot(k_{yt,yu}^{eIII,mIII} b)\} \end{array} \right] \begin{bmatrix} \mathbf{A}^I \\ \mathbf{A}^{II} \\ \mathbf{A}^{III} \end{bmatrix} \end{aligned} \quad (2-24)$$

The coupling matrices, for example, have the following form

$$\mathbf{K}^{I-III} = \text{diag}\left(\sqrt{Z_{p,q}^{eI,mI}}\right) \begin{bmatrix} \mathbf{K}^{eI-eIII} & \mathbf{K}^{eI-mIII} \\ \frac{\sin k_{yt}^{eIII} b}{\mathbf{K}^{mI-eIII}} & \frac{\sin k_{yu}^{mIII} b}{\mathbf{K}^{mI-mIII}} \\ \sin k_{yt}^{eIII} b & \sin k_{yu}^{mIII} b \end{bmatrix} \text{diag}\left(\sqrt{Y_{t,u}^{eIII,mIII}}\right) \quad (2-25)$$

where the individual elements are given by

$$\begin{aligned}
K_{p,i}^{eI-eIII} &= \iint_{S^I} (\nabla_z \Psi_p^{eI}) \cdot \left(-j(\nabla_y \Phi_i^{eIII}) \cos k_{y_i}^{eIII} y + \frac{(k_c^2)^{eIII}}{jk_{y_i}^{eIII}} \Phi_i^{eIII} \sin k_{y_i}^{eIII} y \hat{u}_y \right) ds \\
K_{p,u}^{eI-mIII} &= \iint_{S^I} (\nabla_z \Psi_p^{eI}) \cdot \left(-(\hat{u}_y \times \nabla_y \Phi_u^{mIII}) \cos k_{y_u}^{mIII} y \right) ds \\
K_{q,i}^{mI-eIII} &= \iint_{S^I} (\hat{u}_z \times \nabla_z \Psi_q^{mI}) \cdot \left(-j(\nabla_y \Phi_i^{eIII}) \cos k_{y_i}^{eIII} y + \frac{(k_c^2)^{eIII}}{jk_{y_i}^{eIII}} \Phi_i^{eIII} \sin k_{y_i}^{eIII} y \hat{u}_y \right) ds \\
K_{q,u}^{mI-mIII} &= \iint_{S^I} (\hat{u}_z \times \nabla_z \Psi_q^{mI}) \cdot \left(-(\hat{u}_y \times \nabla_y \Phi_u^{mIII}) \cos k_{y_u}^{mIII} y \right) ds
\end{aligned} \tag{2-26}$$

The remaining coupling matrices of eq.(2-24) are expanded in similar fashion.

The matrix eq.(2-24) is solved for the generalized scattering matrix of a simple E -plane T-junction

$$\begin{bmatrix} \mathbf{B}^I \\ \mathbf{B}^{II} \\ \mathbf{B}^{III} \end{bmatrix} = \begin{bmatrix} \mathbf{S}_{11} & \mathbf{S}_{12} & \mathbf{S}_{13} \\ \mathbf{S}_{21} & \mathbf{S}_{22} & \mathbf{S}_{23} \\ \mathbf{S}_{31} & \mathbf{S}_{32} & \mathbf{S}_{33} \end{bmatrix} \begin{bmatrix} \mathbf{A}^I \\ \mathbf{A}^{II} \\ \mathbf{A}^{III} \end{bmatrix}. \tag{2-27}$$

The scattering matrix of three port junctions may be cascaded with scattering matrices of other multi-port junctions using the algorithms found in Appendix A.

3. T-SEPTUM WAVEGUIDE

3.1 INTRODUCTION

Prior to this point, a review of the standard approach to the mode-matching method has been presented as an introduction to the analysis of nonstandard multi-port waveguide discontinuities. This chapter now details the treatment of the T-septum waveguide. As indicated in Chapter 1, the T-septum is a development from the ridge waveguide whose preliminary analysis indicated an examination of this discontinuity for component design.

The chapter is divided into three sections. The first will examine the cross-sectional analysis to determine the microwave propagation characteristics and modal functions of the waveguide. Second, using this cross-sectional analysis, the scattering matrix of the rectangular-to-T-septum waveguide discontinuity will be calculated. Finally, various components will be designed based on the discontinuity thus determined.

3.2 EIGENVALUE PROBLEM

To begin with, the eigenvalues and eigenfunctions of the T-septum waveguide are calculated for prospective use in formulating the basic building block discontinuity for various computer-aided component design algorithms. Because of their successful application to the ridge waveguide two-dimensional analysis, two mode-matching formulations, namely, the transverse resonance method (TRM) [6, 87], and the

classical standing wave formulation (SWF) [15, 30], have been selected to solve rigorously the cross-sectional boundary value problem [eq.(2-3)]. Since the formulation significantly influences the solution of the related discontinuity problem in complexity, computational effort, and numerical accuracy in relation to the expansion terms considered, careful attention must be given to this choice.

The geometry of the T-septum waveguide with corresponding regional subdivisions for each formulation here described can be seen in Figure 3.1. Due to the symmetry of the cross-section, analysis is simplified by using a magnetic wall (m.w.) and an electric wall (e.w.) at $x = a/2$ and $y = 0$, respectively.

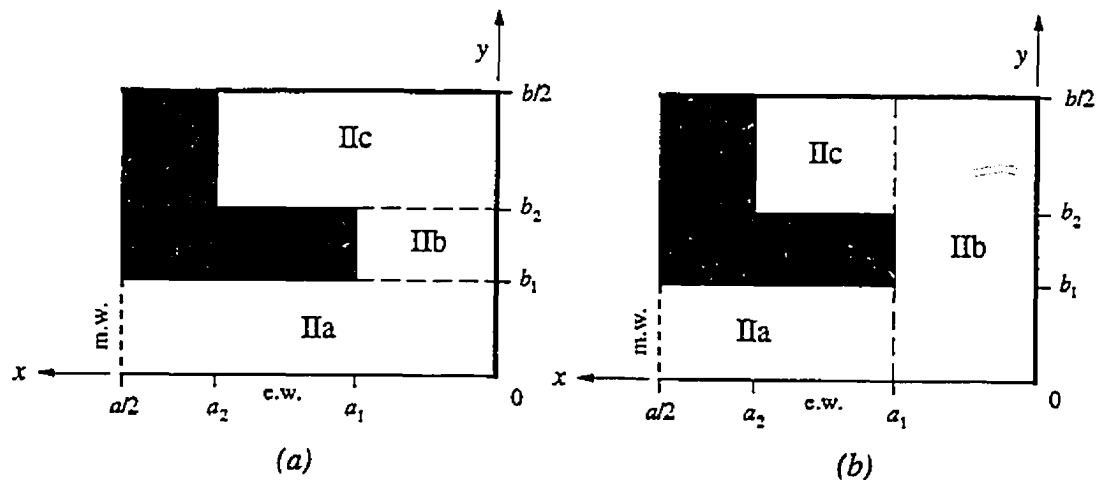


FIGURE 3.1 T-septum waveguide cross-section (quarter section): (a) dimensions and subregions for the transverse-resonance method (TRM); (b) dimensions and subregions for the standing wave formulation (SWF).

The transverse resonance method, as its name implies, consists of a transverse propagation of waves where the boundaries are incorporated as resonance conditions in the last step of the formulation. The classical standing-wave formulation assumes standing wave patterns in the cross-section's subregions and, therefore, introduces boundary conditions prior to subregion interface relations. Both methods produce their own homogeneous characteristic matrix equation which must be solved for the zeros of the determinant [88]. The standing-wave formulation has the advantage of

independently selecting the number of expansion terms in the separate subregions but suffers from having poles in the determinant. The transverse resonance method, on the other hand, has a determinant free of poles but is restricted to an equal number of expansion terms in each subregion resulting in computational instabilities.

The transverse resonance method defines partial propagating waves for the y -dependence of each subregion in the cross-section $i = \text{IIa, IIb, IIc}$ [cf. Figure 3.1(a)]:

$$\begin{aligned} P_r^{ei}(y) &= \frac{d}{dy} Q_r^{ei} = jk_{yr}^{ei} \left(-A_r^{ei} \exp(-jk_{yr}^{ei}y) + B_r^{ei} \exp(+jk_{yr}^{ei}y) \right) \\ Q_s^{mi}(y) &= \frac{d}{dy} P_s^{mi} = C_s^{mi} \exp(+jk_{ys}^{mi}y) + D_s^{mi} \exp(-jk_{ys}^{mi}y) \end{aligned} \quad (3-1)$$

Hence, the cross-section functions are specified for each sub-region as

$$\begin{aligned} \Psi^{e\text{IIa}} &= \sum_{r=1}^{n^{\text{IIa}}} Q_r^{e\text{IIa}}(y) \cos\left(\frac{(2r-1)\pi}{a}x\right) & \Psi^{m\text{IIa}} &= \sum_{r=1}^{n^{\text{IIa}}} P_r^{m\text{IIa}}(y) \sin\left(\frac{(2r-1)\pi}{a}x\right) \\ \Psi^{e\text{IIb}} &= \sum_{s=0}^{n^{\text{IIb}}} Q_s^{e\text{IIb}}(y) \frac{\cos(s\pi/a_1)x}{\sqrt{1+\delta_{or}}} & \Psi^{m\text{IIb}} &= \sum_{s=1}^{n^{\text{IIb}}} P_s^{m\text{IIb}}(y) \sin(s\pi/a_1)x \\ \Psi^{e\text{IIc}} &= \sum_{t=0}^{n^{\text{IIc}}} Q_t^{e\text{IIc}}(y) \frac{\cos(t\pi/a_2)x}{\sqrt{1+\delta_{or}}} & \Psi^{m\text{IIc}} &= \sum_{t=1}^{n^{\text{IIc}}} P_t^{m\text{IIc}}(y) \sin(t\pi/a_2)x \end{aligned} \quad (3-2)$$

where δ is the Kronecker delta and

$$\left\{ \begin{array}{l} \left(k_{yr}^{e\text{IIa}, m\text{IIa}}\right)^2 \\ \left(k_{ys}^{e\text{IIb}, m\text{IIb}}\right)^2 \\ \left(k_{yt}^{e\text{IIc}, m\text{IIc}}\right)^2 \end{array} \right\} = \omega^2 \mu_o \epsilon_o - \left\{ \begin{array}{l} \left((2r-1)\pi/a\right)^2 \\ \left(s\pi/a_1\right)^2 \\ \left(t\pi/a_2\right)^2 \end{array} \right\}. \quad (3-3)$$

Applying the field matching conditions for both the TE_z and TM_z modes at the common interfaces, i.e.,

$$\left. \begin{array}{l} \bar{\mathbf{E}}_{x,z}^{\text{IIa}} = \bar{\mathbf{E}}_{x,z}^{\text{IIb}} \\ \bar{\mathbf{H}}_{x,z}^{\text{IIa}} = \bar{\mathbf{H}}_{x,z}^{\text{IIb}} \end{array} \right\} \text{ at } y = b_1 \quad \text{and} \quad \left. \begin{array}{l} \bar{\mathbf{E}}_{x,z}^{\text{IIb}} = \bar{\mathbf{E}}_{x,z}^{\text{IIc}} \\ \bar{\mathbf{H}}_{x,z}^{\text{IIb}} = \bar{\mathbf{H}}_{x,z}^{\text{IIc}} \end{array} \right\} \text{ at } y = b_2 \quad (3-4)$$

and utilizing orthogonal properties, leads to a relationality between the functions of the subregions at $y = b_1$ and $y = b_2$ given by

$$\begin{aligned} \begin{bmatrix} \mathbf{P}^{eIIb}(b_1) \\ \mathbf{Q}^{eIIb}(b_1) \end{bmatrix} &= \begin{bmatrix} (\mathbf{J}^{eIIa-IIb})^{-1} & \mathbf{0} \\ \mathbf{0} & (\mathbf{J}^{eIIa-IIb})^T \end{bmatrix} \begin{bmatrix} \mathbf{P}^{eIIa}(b_1) \\ \mathbf{Q}^{eIIa}(b_1) \end{bmatrix} = \mathbf{K}^{eIIb-IIa} \begin{bmatrix} \mathbf{P}^{eIIa}(b_1) \\ \mathbf{Q}^{eIIa}(b_1) \end{bmatrix} \\ \begin{bmatrix} \mathbf{P}^{eIIc}(b_2) \\ \mathbf{Q}^{eIIc}(b_2) \end{bmatrix} &= \begin{bmatrix} (\mathbf{J}^{eIIb-IIc})^T & \mathbf{0} \\ \mathbf{0} & (\mathbf{J}^{eIIa-IIb})^{-1} \end{bmatrix} \begin{bmatrix} \mathbf{P}^{eIIb}(b_2) \\ \mathbf{Q}^{eIIb}(b_2) \end{bmatrix} = \mathbf{K}^{eIIc-IIb} \begin{bmatrix} \mathbf{P}^{eIIb}(b_2) \\ \mathbf{Q}^{eIIb}(b_2) \end{bmatrix} \end{aligned} \quad (3-5)$$

for the TE_r modes, and for the TM_r modes:

$$\begin{aligned} \begin{bmatrix} \mathbf{P}^{mIIa}(b_1) \\ \mathbf{Q}^{mIIa}(b_1) \end{bmatrix} &= \begin{bmatrix} \mathbf{J}^{mIIa-IIb} & \mathbf{0} \\ \mathbf{0} & (\mathbf{J}^{mIIa-IIb})^{-T} \end{bmatrix} \begin{bmatrix} \mathbf{P}^{mIIb}(b_1) \\ \mathbf{Q}^{mIIb}(b_1) \end{bmatrix} = \mathbf{K}^{mIIa-IIb} \begin{bmatrix} \mathbf{P}^{mIIb}(b_1) \\ \mathbf{Q}^{mIIb}(b_1) \end{bmatrix} \\ \begin{bmatrix} \mathbf{P}^{mIIb}(b_2) \\ \mathbf{Q}^{mIIb}(b_2) \end{bmatrix} &= \begin{bmatrix} (\mathbf{J}^{mIIb-IIc})^{-T} & \mathbf{0} \\ \mathbf{0} & \mathbf{J}^{mIIb-IIc} \end{bmatrix} \begin{bmatrix} \mathbf{P}^{mIIc}(b_2) \\ \mathbf{Q}^{mIIc}(b_2) \end{bmatrix} = \mathbf{K}^{mIIb-IIc} \begin{bmatrix} \mathbf{P}^{mIIc}(b_2) \\ \mathbf{Q}^{mIIc}(b_2) \end{bmatrix} \end{aligned} \quad (3-6)$$

where elements of the coupling matrices are

$$\begin{aligned} J_{rs}^{eIIa-IIb} &= \int_0^{a_1} \frac{2}{\sqrt{a}} \sqrt{\frac{2}{a_1}} \cos\left(\frac{(2r-1)\pi}{a}x\right) \frac{\cos(s\pi/a_1)x}{\sqrt{1+\delta_{os}}} dx \\ J_{st}^{eIIb-IIc} &= \int_0^{a_2} \sqrt{\frac{2}{a_1}} \sqrt{\frac{2}{a_2}} \frac{\cos(s\pi/a_1)x}{\sqrt{1+\delta_{os}}} \frac{\cos(t\pi/a_2)x}{\sqrt{1+\delta_{ot}}} dx \\ J_{rs}^{mIIa-IIb} &= \int_0^{a_1} \frac{2}{\sqrt{a}} \sqrt{\frac{2}{a_1}} \sin\left(\frac{(2r-1)\pi}{a}x\right) \sin(s\pi/a_1)x dx \\ J_{st}^{mIIb-IIc} &= \int_0^{a_2} \sqrt{\frac{2}{a_1}} \sqrt{\frac{2}{a_2}} \sin(s\pi/a_1)x \sin(t\pi/a_2)x dx \end{aligned} \quad (3-7)$$

By introducing a transmission matrix in the y -direction, which transforms the partial propagating wave functions \mathbf{P} and \mathbf{Q} from the lower boundary, b_l , to the upper boundary, b_u , or vice versa

$$\begin{bmatrix} \mathbf{P}^{ei}(b_u) \\ \mathbf{Q}^{ei}(b_u) \end{bmatrix} = \begin{bmatrix} \text{diag}(\cos k_{yn}^{ei}d) & \text{diag}(-k_{yn}^{ei} \sin k_{yn}^{ei}d) \\ \text{diag}\left(\frac{\sin k_{yn}^{ei}d}{k_{yn}^{ei}}\right) & \text{diag}(\cos k_{yn}^{ei}d) \end{bmatrix} \begin{bmatrix} \mathbf{P}^{ei}(b_l) \\ \mathbf{Q}^{ei}(b_l) \end{bmatrix} = \mathbf{U}^{ei} \begin{bmatrix} \mathbf{P}^{ei}(b_l) \\ \mathbf{Q}^{ei}(b_l) \end{bmatrix}$$

$$\begin{bmatrix} \mathbf{P}^{mi}(b_l) \\ \mathbf{Q}^{mi}(b_l) \end{bmatrix} = \begin{bmatrix} \text{diag}(\cos k_{yn}^{mi} d) & \text{diag}\left(\frac{-\sin k_{yn}^{mi} d}{k_{yn}^{mi}}\right) \\ \text{diag}(k_{yn}^{mi} \sin k_{yn}^{mi} d) & \text{diag}(\cos k_{yn}^{mi} d) \end{bmatrix} \begin{bmatrix} \mathbf{P}^{mi}(b_u) \\ \mathbf{Q}^{mi}(b_u) \end{bmatrix} = \mathbf{U}^{mi} \begin{bmatrix} \mathbf{P}^{mi}(b_u) \\ \mathbf{Q}^{mi}(b_u) \end{bmatrix} \quad (3-8)$$

where $d = b_u - b_l$, the following matrix equations may be derived

$$\begin{aligned} \begin{bmatrix} \mathbf{P}^{eIIc}(b/2) \\ \mathbf{Q}^{eIIc}(b/2) \end{bmatrix} &= \underbrace{\mathbf{U}^{eIIc} \mathbf{K}^{eIIc-IIb} \mathbf{U}^{eIIb} \mathbf{K}^{eIIb-IIa} \mathbf{U}^{eIIa}}_{\mathbf{W}^e} \begin{bmatrix} \mathbf{P}^{eIIa}(0) \\ \mathbf{Q}^{eIIa}(0) \end{bmatrix} \\ \begin{bmatrix} \mathbf{P}^{mIIa}(0) \\ \mathbf{Q}^{mIIa}(0) \end{bmatrix} &= \underbrace{\mathbf{U}^{mIIa} \mathbf{K}^{mIIa-IIb} \mathbf{U}^{mIIb} \mathbf{K}^{mIIb-IIc} \mathbf{U}^{mIIc}}_{\mathbf{W}^m} \begin{bmatrix} \mathbf{P}^{mIIc}(b/2) \\ \mathbf{Q}^{mIIc}(b/2) \end{bmatrix} \end{aligned} \quad (3-9)$$

The two remaining boundary conditions, commonly referred to as resonance conditions, at $y=0$ and $y=b/2$ are imposed on eqs.(3-9) to construct the homogeneous characteristic matrix equations

$$\mathbf{W}_{12}^e \mathbf{Q}^{eIIa}(0) = \mathbf{0} \quad \text{and} \quad \mathbf{W}_{12}^m \mathbf{Q}^{mIIc}(b/2) = \mathbf{0}. \quad (3-10)$$

where \mathbf{W}_{12} is a submatrix of \mathbf{W} . Eqs.(3-10) must be solved for the zeros of the determinant of \mathbf{W}_{12} by varying the frequency f . Every zero corresponds to a cut-off frequency of the T-septum waveguide eigenmode spectrum and a set of separation constants. Once a cut-off frequency is found, the corresponding eigenvector \mathbf{Q}^{eIIa} or \mathbf{Q}^{mIIc} may be determined from eqs.(3-10). Using the coupling matrices \mathbf{K} and the transmission matrices \mathbf{U} , the functions \mathbf{P} and \mathbf{Q} may be calculated for each subregion. That is, these functions are determined by

$$\begin{aligned} \mathbf{Q}^{eIIc}(b/2) &= \mathbf{W}_{22}^e \mathbf{Q}^{eIIa}(0) \\ \begin{bmatrix} \mathbf{P}^{eIIb}(b_2) \\ \mathbf{Q}^{eIIb}(b_2) \end{bmatrix} &= \mathbf{U}^{eIIb} \mathbf{K}^{eIIb-IIa} \mathbf{U}^{eIIa} \begin{bmatrix} \mathbf{0} \\ \mathbf{Q}^{eIIa}(0) \end{bmatrix} \end{aligned} \quad (3-11)$$

and

$$\mathbf{Q}^{mIIa}(0) = \mathbf{W}_{22}^m \mathbf{Q}^{mIIc}(b/2)$$

$$\begin{bmatrix} \mathbf{P}^{m\Pi b}(b_2) \\ \mathbf{Q}^{m\Pi b}(b_2) \end{bmatrix} = \mathbf{K}^{m\Pi b-\Pi c} \mathbf{U}^{e\Pi c} \begin{bmatrix} \mathbf{0} \\ \mathbf{Q}^{e\Pi c}(b/2) \end{bmatrix} \quad (3-12)$$

Hence, the cross-section functions are now completely specified for each sub-region as

$$\begin{aligned} \Psi^{e\Pi a} &= \sum_{r=1}^{n^{a2}} \cos\left(\frac{(2r-1)\pi}{a}x\right) Q_r^{e\Pi a}(0) \cos k_{yr}^{e\Pi a} y \\ \Psi^{e\Pi b} &= \sum_{s=0}^{n^{b1}} \frac{\cos(s\pi/a_1)x}{\sqrt{1+\delta_{os}}} \left[Q_s^{e\Pi b}(b_2) \cos k_{ys}^{e\Pi b}(b_2-y) - \frac{P_s^{e\Pi b}(b_2)}{k_{ys}^{e\Pi b}} \sin k_{ys}^{e\Pi b}(b_2-y) \right] \\ \Psi^{e\Pi c} &= \sum_{t=0}^{n^{c1}} \frac{\cos(t\pi/a_2)x}{\sqrt{1+\delta_{ot}}} Q_t^{e\Pi c}(b/2) \cos k_{yt}^{e\Pi c}\left(\frac{b}{2}-y\right) \end{aligned} \quad (3-13)$$

for the TE_z modes, and for the TM_z modes

$$\begin{aligned} \Psi^{m\Pi a} &= \sum_{r=1}^{n^{a2}} \sin\left(\frac{(2r-1)\pi}{a}x\right) \frac{Q_r^{m\Pi a}(0)}{k_{yr}^{m\Pi a}} \sin k_{yr}^{m\Pi a} y \\ \Psi^{m\Pi b} &= \sum_{s=1}^{n^{b1}} \sin(s\pi/a_1)x \left[P_s^{m\Pi b}(b_2) \cos k_{ys}^{m\Pi b}(b_2-y) - \frac{Q_s^{m\Pi b}(b_2)}{k_{ys}^{m\Pi b}} \sin k_{ys}^{m\Pi b}(b_2-y) \right] \\ \Psi^{m\Pi c} &= \sum_{t=1}^{n^{c1}} -\sin(t\pi/a_2)x \frac{Q_t^{m\Pi c}(b/2)}{k_{yt}^{m\Pi c}} \sin k_{yt}^{m\Pi c}\left(\frac{b}{2}-y\right) \end{aligned} \quad (3-14)$$

It is important to note that, due to the matrix inversions in eq.(3-5) and eq.(3-6), the number of expansion terms in the subregions Πa , Πb , and Πc must be equal. This tends to cause computational instabilities because of the extremely large numbers to be processed by the computer for configurations with large septum widths (as in a narrow region Πb). This results in an example from eq.(3-3), as a_1 approaches zero, the wave number becomes infinite. Furthermore, the transverse-resonance method cannot be applied in the x -direction, since the left-hand side boundaries of subregions Πa and Πc have different x -coordinates.

The standing wave formulation, on the other hand, incorporates the boundary conditions outlined in eq.(2-3) as a first step toward solution, and hence, becomes extremely flexible to the different patterns of subregion division. It may be noted, however, that unlike the transverse resonance method, it is difficult to incorporate

modifications to the T-septum cross-section without substantial alteration of the algorithm. When applying the standing wave formulation, the cross-section is again divided into three, as shown in Figure 3.1(b). By satisfying the known boundary conditions, the subregion functions for the TE_z modes are written as

$$\begin{aligned}\Psi^{e\Pi a} &= \sum_{r=0}^{n^{e\Pi a}} A_r^{e\Pi a} \frac{\sin k_{xr}^{e\Pi a} (x - a/2) \cos(r\pi/b_1)y}{k_{xr}^{e\Pi a} \sqrt{1 + \delta_{or}}} \\ \Psi^{e\Pi b} &= \sum_{s=0}^{n^{e\Pi b}} A_s^{e\Pi b} \cos k_{xs}^{e\Pi b} x \frac{\cos(2s\pi/b)y}{\sqrt{1 + \delta_{os}}} \\ \Psi^{e\Pi c} &= \sum_{t=0}^{n^{e\Pi c}} A_t^{e\Pi c} \cos k_{xt}^{e\Pi c} (x - a_2) \frac{\cos[(t\pi/d)(y - b_2)]}{\sqrt{1 + \delta_{ot}}}\end{aligned}\quad (3-15)$$

and for the TM_z modes they are

$$\begin{aligned}\Psi^{m\Pi a} &= \sum_{r=0}^{n^{m\Pi a}} A_r^{m\Pi a} \cos k_{xr}^{m\Pi a} (x - a/2) \sin(r\pi/b_1)y \\ \Psi^{m\Pi b} &= \sum_{s=0}^{n^{m\Pi b}} A_s^{m\Pi b} \frac{\sin k_{xs}^{m\Pi b} x}{k_{xs}^{m\Pi b}} \sin(2s\pi/b)y \\ \Psi^{m\Pi c} &= \sum_{t=0}^{n^{m\Pi c}} A_t^{m\Pi c} \frac{\sin k_{xt}^{m\Pi c} (x - a_2)}{k_{xt}^{m\Pi c}} \sin[(t\pi/d)(y - b_2)]\end{aligned}\quad (3-16)$$

with

$$\begin{Bmatrix} (k_{xr}^{e\Pi a})^2 \\ (k_{xs}^{e\Pi b})^2 \\ (k_{xt}^{e\Pi c})^2 \end{Bmatrix} = \omega^2 \mu_o \epsilon_o - \begin{Bmatrix} (r\pi/b_1)^2 \\ (2s\pi/b)^2 \\ (t\pi/d)^2 \end{Bmatrix}\quad (3-17)$$

and $d = (b/2) - b_2$.

Applying field matching conditions at the common interface of $x = a_1$, i.e., matching the subregion functions as well as their derivatives with respect to x , yields two sets of three matrix equations, each relating the unknown amplitude coefficients to each other. In order to minimize the number of matrix inversions, homogeneous characteristic equations are derived for the amplitude coefficients $A^{e\Pi b}$ and $A^{m\Pi b}$ in region IIb. These

are

$$\begin{aligned}
 & \left[\text{diag}(-k_{xz}^{e\text{IIb}} \sin k_{xz}^{e\text{IIb}} a_1) \right. \\
 & - (\mathbf{J}^{e\text{IIa-IIb}})^T \text{diag}(k_{xz}^{e\text{IIa}} \cot k_{xz}^{e\text{IIa}} (a_1 - a/2)) \mathbf{J}^{e\text{IIa-IIb}} \text{diag}(\cos k_{xz}^{e\text{IIb}} a_1) \\
 & \left. + \mathbf{J}^{e\text{IIb-IIc}} \text{diag}(k_{xz}^{e\text{IIc}} \tan k_{xz}^{e\text{IIc}} (a_1 - a_2)) (\mathbf{J}^{e\text{IIb-IIc}})^T \text{diag}(\cos k_{xz}^{e\text{IIb}} a_1) \right] \mathbf{A}^{e\text{IIb}} = \mathbf{0}
 \end{aligned} \quad (3-18)$$

and

$$\begin{aligned}
 & \left[\text{diag}\left(\frac{-\sin k_{xz}^{m\text{IIb}} a_1}{k_{xz}^{m\text{IIb}}}\right) \right. \\
 & - (\mathbf{J}^{m\text{IIa-IIb}})^T \text{diag}\left(\frac{\cot k_{xz}^{m\text{IIa}} (a_1 - a/2)}{k_{xz}^{m\text{IIa}}}\right) \mathbf{J}^{m\text{IIa-IIb}} \text{diag}(\cos k_{xz}^{m\text{IIb}} a_1) \\
 & \left. + \mathbf{J}^{m\text{IIb-IIc}} \text{diag}\left(\frac{\tan k_{xz}^{m\text{IIc}} (a_1 - a_2)}{k_{xz}^{m\text{IIc}}}\right) (\mathbf{J}^{m\text{IIb-IIc}})^T \text{diag}(\cos k_{xz}^{m\text{IIb}} a_1) \right] \mathbf{A}^{m\text{IIb}} = \mathbf{0}
 \end{aligned} \quad (3-19)$$

where the elements in the coupling matrices are

$$\begin{aligned}
 J_{rs}^{r\text{IIa-IIb}} &= \int_0^{b_1} \sqrt{\frac{2}{b_1}} \frac{2}{\sqrt{b}} \frac{\cos k_{yr}^{e\text{IIa}} y}{\sqrt{1 + \delta_{0r}}} \frac{\cos k_{ys}^{e\text{IIb}} y}{\sqrt{1 + \delta_{0s}}} dy \\
 J_{st}^{e\text{IIb-IIc}} &= \int_{b_2}^{b/2} \frac{2}{\sqrt{b}} \sqrt{\frac{2}{w}} \frac{\cos k_{ys}^{e\text{IIb}} y}{\sqrt{1 + \delta_{0s}}} \frac{\cos k_{yt}^{e\text{IIc}} (y - b_2)}{\sqrt{1 + \delta_{0t}}} dy \\
 J_{rs}^{m\text{IIa-IIb}} &= \int_0^{b_1} \sqrt{\frac{2}{b_1}} \frac{2}{\sqrt{b}} \sin k_{yr}^{m\text{IIa}} y \sin k_{ys}^{m\text{IIb}} y dy \\
 J_{st}^{m\text{IIb-IIc}} &= \int_{b_2}^{b/2} \frac{2}{\sqrt{b}} \sqrt{\frac{2}{w}} \sin k_{ys}^{m\text{IIb}} y \sin k_{yt}^{m\text{IIc}} (y - b_2) dy
 \end{aligned} \quad (3-20)$$

The terms in the square brackets in eq.(3-18) and eq.(3-19) represent the characteristic matrices for the TE_z and TM_z modes, respectively, and must be solved for the zeros of the determinant by varying the frequency f to specify the corresponding mode cut-off frequencies. The eigenvectors or amplitude coefficients $\mathbf{A}^{e\text{IIb}}$ and $\mathbf{A}^{m\text{IIb}}$ may once again be determined where a zero is detected. By using the coupling matrices and diagonal matrices, these, in turn, are related to the amplitude coefficients in regions IIa and IIc,

$$\begin{aligned}
\mathbf{A}^{e\Pi a} &= \text{diag}\left(k_{x'}^{e\Pi a} \csc k_{x'}^{e\Pi a} (a_1 - a/2)\right) \mathbf{J}^{e\Pi a - \Pi b} \text{diag}(\cos k_{x'}^{e\Pi b} a_1) \mathbf{A}^{e\Pi b} \\
\mathbf{A}^{e\Pi c} &= \text{diag}\left(k_{x'}^{e\Pi c} \sec k_{x'}^{e\Pi c} (a_1 - a_2)\right) (\mathbf{J}^{e\Pi b - \Pi c})^T \text{diag}(\cos k_{x'}^{e\Pi b} a_1) \mathbf{A}^{e\Pi b} \\
\mathbf{A}^{m\Pi a} &= \text{diag}\left(\frac{-\csc k_{x'}^{m\Pi a} (a_1 - a/2)}{k_{x'}^{m\Pi a}}\right) \mathbf{J}^{m\Pi a - \Pi b} \text{diag}(\cos k_{x'}^{m\Pi b} a_1) \mathbf{A}^{m\Pi b} \\
\mathbf{A}^{m\Pi c} &= \text{diag}(\cos k_{x'}^{m\Pi c} (a_1 - a_2)) (\mathbf{J}^{m\Pi b - \Pi c})^T \text{diag}(\cos k_{x'}^{m\Pi b} a_1) \mathbf{A}^{m\Pi b}
\end{aligned} \tag{3-21}$$

and, hence, the cross-section functions [eqs.(3-15) and (3-16)] are determined completely.

Two algorithms are employed to locate the zeros of the determinant for the characteristic equation. The first algorithm is one based on sign reversal of a logarithmic function of the determinant, given by

$$f(\det(\mathbf{M})) = \beta \cdot \text{sgn}[\det(\mathbf{M})] \cdot \log_{10}[1 + |\det(\mathbf{M})|] \tag{3-22}$$

where β is a scaling factor, sgn is the signum function, and $\det(\mathbf{M})$ denotes determinant. The second is a minimum search algorithm for the smallest singular value. The characteristic matrix \mathbf{M} , for which the zeros of the determinant are to be found, is decomposed into three matrices [89]:

$$\mathbf{M} = \mathbf{W}\mathbf{\Sigma}\mathbf{V}^T \tag{3-23}$$

where $\mathbf{\Sigma}$ is a diagonal matrix formed by the singular values σ ordered in decreasing value, and where the columns of \mathbf{W} and \mathbf{V} are the left and right singular vectors of \mathbf{M} , respectively. Using the property

$$\sigma_{\min} = 0, \quad \text{if and only if} \quad \det(\mathbf{M}) = 0 \tag{3-24}$$

the algorithm searches over the frequency spectrum for the minima of the last element σ_{\min} in the matrix $\mathbf{\Sigma}$.

Figure 3.2 compares the system determinant to the minimum singular value versus frequency for the transverse-resonance method and the standing-wave formulation. The zeros of the determinant, which coincide to the minima of the minimum singular value, correspond to the TE_z mode cut-off frequencies of the T-septum waveguide. Although the numerical search for a minimum is a somewhat more

difficult process compared to the sign reversal algorithm, the advantage of singular value decomposition, as illustrated by Figure 3.2, lies primarily in the fact that the procedure provides numerical stability independent of the presence of steep gradients, and, in the case of the standing-wave formulation, eliminates the presence of poles in the determinant function which can be extremely close to zeros. The assurance of a reliable detection of the determinant zeros on a computer with limited accuracy by singular value decomposition certainly outweighs the slight increase in complexity of a minima searching algorithm. Moreover, an increase in the minima of the σ_{\min} indicates a reduced accuracy in computation which may be incorporated into the algorithm when determining the optimum number of expansion terms.

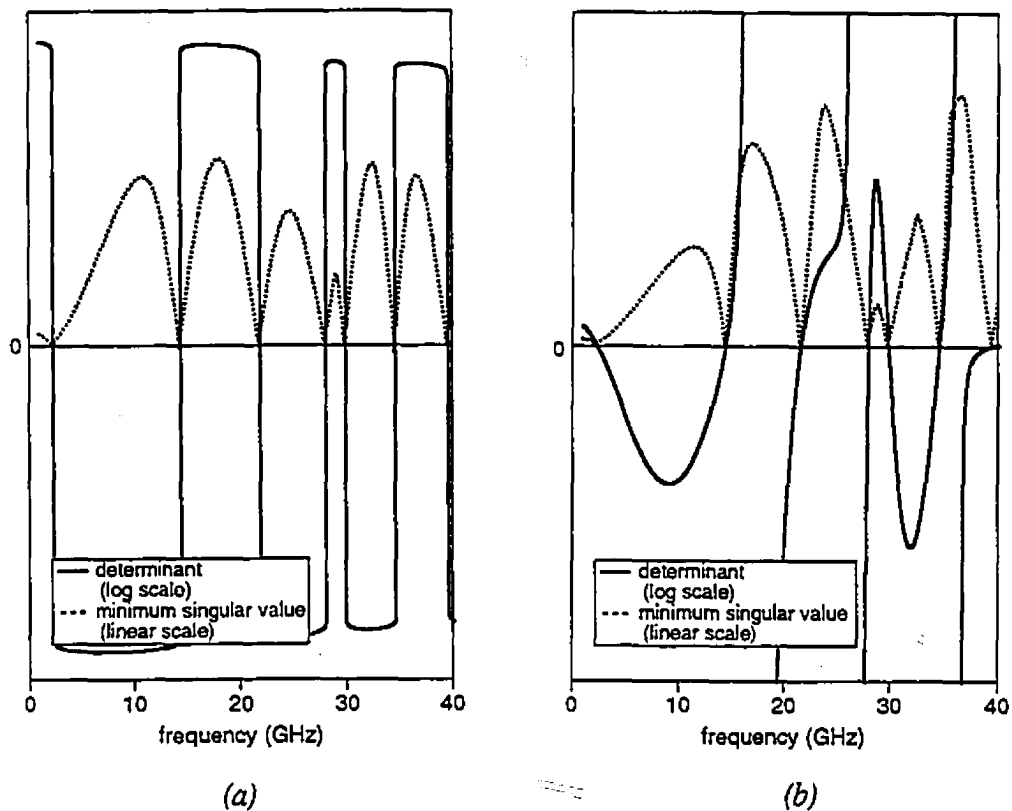


FIGURE 3.2 Typical behavior of system determinant and minimum singular value versus frequency: (a) transverse resonance method (TRM); (b) standing wave formulation (SWF). Dimensions (mm): $a = 22.86$, $b = 11.425$, $a_1 = 5.7125$, $a_2 = 10.2825$, $b_1 = 0.8569$, and $b_2 = 1.1425$ (cf. Figure 3.1).

As a result, when using singular value decomposition for both field matching techniques, the main advantage of the standing-wave formulation over the transverse resonance method, namely, the flexibility of allowing a selection of different subregion expansion term ratios, becomes obvious, particularly for small gap widths. It is precisely the smaller gap widths that are advantageous for component design by lowering the fundamental mode cut-off frequency. Figure 3.3 shows a convergence analysis of the first two mode cut-off frequencies using the two different mode-matching formulations and singular value decomposition. Due to the restriction of equal expansion terms in all subregions, the transverse resonance method can only be used up to $n^{\text{th}} = 8$ expansion terms. In the standing-wave formulation, the corresponding number of expansion terms is that of region IIb, whereas, the number of expansion terms in IIa and IIc is chosen according to a ratio of subregion dimensions. Convergence, using the standing-wave formulation, is achieved for the first and second mode cut-off wavelengths after ten expansion terms. In comparison, using the transverse resonance method, numerical instability appears prior to convergence being adequately demonstrated. The increase in the number of expansion terms necessary to reach convergence in the transverse resonance method requires an extended precision compiler. Using a double precision compiler, for example, the minimum width of region IIb that will allow computation of the propagation characteristics before numerical instabilities occur, has been shown to be one quarter of the waveguide's width [90].

With the flexible expansion term ratio and the singular value decomposition technique to circumvent the poles in the system determinant, the standing-wave formulation has a clear advantage over the transverse resonance method producing results closely in agreement with both the previously published T-septum waveguide cut-off frequencies. Therefore, the standing-wave formulation used in conjunction with the singular value decomposition has been incorporated into component design to calculate the cut-off frequencies and propagation constants of the T-septum waveguide. A detailed description of the effects of these two different cross-section eigenfunction formulations on three-dimensional mode-matching analysis for the ridge waveguide in component design can be found in [32, 61].

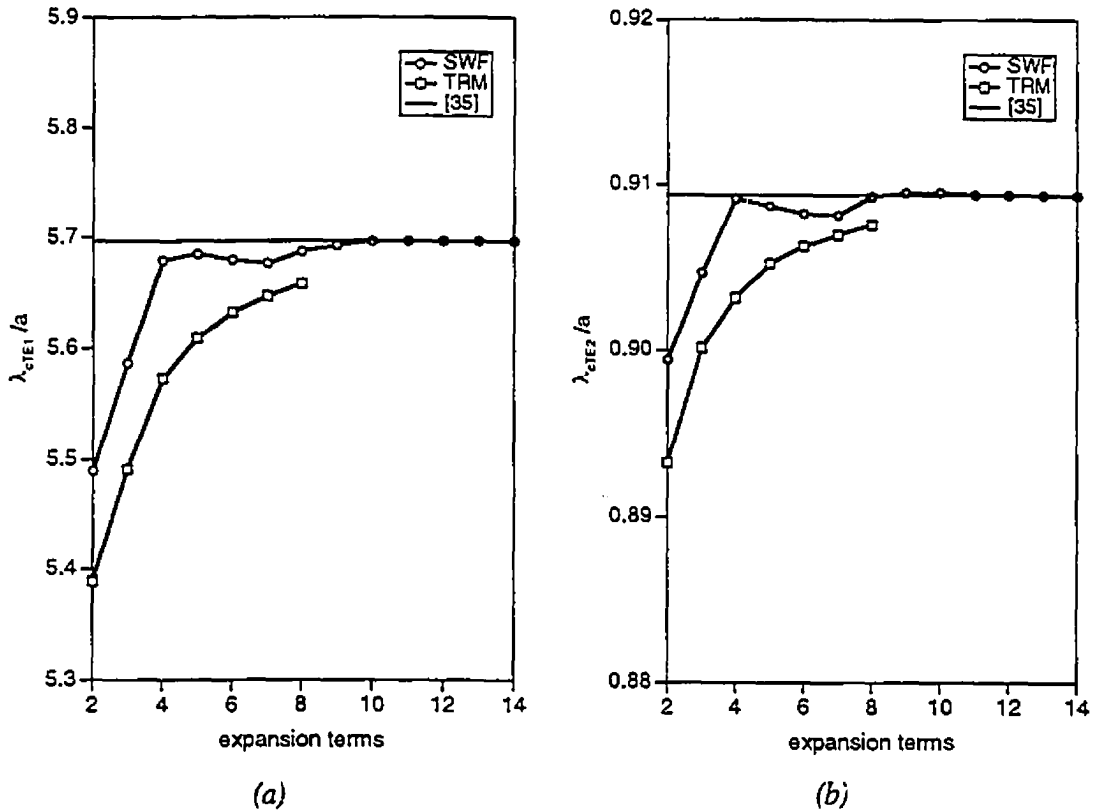


FIGURE 3.3 Convergence analysis and comparison with [35]: (a) normalized cut-off wavelength of fundamental-mode; (b) normalized cut-off wavelength of first higher mode. Dimensions same as in Figure 3.2.

As mentioned in Section 1.2.1, it is possible to consider the use of a variational method to solve the two-dimensional problem in conjunction with mode-matching to solve for the propagation direction. Such a solution would be necessary in the case of arbitrarily shaped cross-sections and might lose its computational time disadvantage in the case where the number of the subregions starts to become very large, or the cross-section becomes non-symmetrical. In such situations, the Finite Element Method [6, 69], the Method of Lines [6] or the Finite Difference Method [6, 7] might be considered. However, the major drawback of such a combination of methods is the difficulty in determining by the variational methods the modal amplitude coefficients required for the third-dimension mode-matching analysis. It is precisely a knowledge of these modal amplitude coefficients which allows for the efficient cascading of the discontinuities in the propagation direction (cf. Appendix A). The solution to the

eigenvalue problem proposed here encounters no such difficulty and indeed allows an easy computation of these amplitude coefficients. A further examination of these so-called 'combined methods' might be highly interesting and possibly productive; however, such an investigation is beyond the scope of this thesis.

3.3 RECTANGULAR-TO-T-SEPTUM WAVEGUIDE DISCONTINUITY

The geometry of the rectangular-to-T-septum waveguide discontinuity is shown in Figure 3.4. The derivation of the modal scattering matrix of this discontinuity is similar to that of the double-plane step in Chapter 2 with the exception that the cross-section functions of region II are those of the T-septum as determined in the preceding section.

Again, solutions to the Helmholtz equation are written in each region, $i = I$ and II, as in eq.(2-8), repeated here for convenience

$$\begin{aligned} \psi^{ei}(x, y, z) &= \sum_{p=1}^{n^i} \sqrt{Z_p^{ei}} \Psi_p^{ei}(x, y) \{A_p^{ei} \exp(-jk_{zp}^{ei} z) + B_p^{ei} \exp(+jk_{zp}^{ei} z)\} \\ \psi^{mi}(x, y, z) &= \sum_{q=1}^{n^i} \sqrt{Y_q^{mi}} \Psi_q^{mi}(x, y) \{A_q^{mi} \exp(-jk_{zq}^{mi} z) - B_q^{mi} \exp(+jk_{zq}^{mi} z)\} \end{aligned} \quad (2-8)$$

where the cross-section functions are ordered in modes of increasing cut-off frequencies.

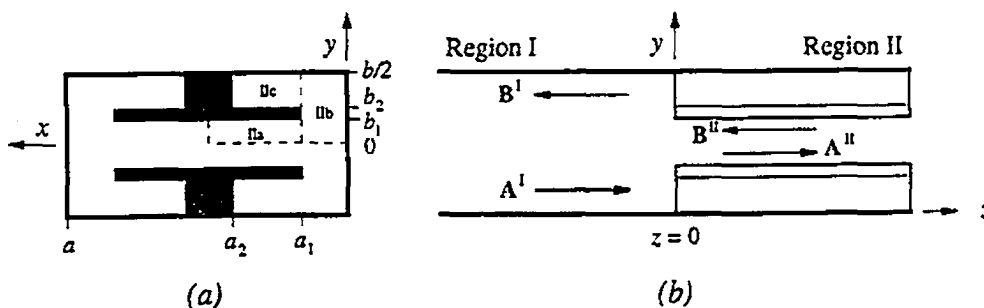


FIGURE 3.4 Geometry of a rectangular-to-T-septum waveguide discontinuity: (a) end view; (b) side view.

For waveguide I, using symmetry, the cross-section functions are

$$\begin{aligned}\Psi_p^{ei}(x, y) &= C_{mn}^I \cos\left(\frac{(2m-1)\pi}{a}x\right) \cos\left(\frac{2n\pi}{b}y\right) \\ \Psi_q^{mi}(x, y) &= D_{mn}^I \sin\left(\frac{(2m-1)\pi}{a}x\right) \sin\left(\frac{2n\pi}{b}y\right)\end{aligned}\quad (3-25)$$

where $m, n \rightarrow p$, $m, n \rightarrow q$. For waveguide II, the cross-section functions are a sum of the functions of each subregion, i.e.,

$$\begin{aligned}\Psi_p^{eII}(x, y) &= \sum_{r=1}^{n^{eIIa}} \Psi_r^{eIIa} + \sum_{s=1}^{n^{eIIb}} \Psi_s^{eIIb} + \sum_{t=1}^{n^{eIIc}} \Psi_t^{eIIc} \\ \Psi_q^{mII}(x, y) &= \sum_{r=1}^{n^{mIIa}} \Psi_r^{mIIa} + \sum_{s=1}^{n^{mIIb}} \Psi_s^{mIIb} + \sum_{t=1}^{n^{mIIc}} \Psi_t^{mIIc}\end{aligned}\quad (3-26)$$

[cf. eqs.(3-15) and (3-16)]. Notice that the functions, $\Psi^{e,mIIa}$, $\Psi^{e,mIIb}$ and $\Psi^{e,mIIc}$ within the subregions are themselves a summation over the eigenfunction expansions. Hence, each p and q in waveguide II corresponds to sets of indices r , s , and t determined in the T-septum eigenvalue problem (cf. Section 3.2).

The cross-section functions in each region I and II are now normalized by eq.(2-10) satisfying eq.(2-11). The field continuity equations for the discontinuity are applied

$$\left. \begin{aligned}\bar{\mathbf{E}}_T^I &= \bar{\mathbf{E}}_T^{II} && \text{on } IIa, IIb, IIc \\ \bar{\mathbf{E}}_T^I &= \mathbf{0} && \text{otherwise} \\ \bar{\mathbf{H}}_T^I &= \bar{\mathbf{H}}_T^{II} && \text{on } IIa, IIb, IIc\end{aligned}\right\} \text{at } z = 0 \quad (3-27)$$

which yield the modal scattering matrix [eq.(2-13)] of the discontinuity rendered in eqs.(2-14) to (2-16):

$$\begin{bmatrix} \mathbf{B}^I \\ \mathbf{A}^{II} \end{bmatrix} = \begin{bmatrix} \mathbf{S}_{11} & \mathbf{S}_{12} \\ \mathbf{S}_{21} & \mathbf{S}_{22} \end{bmatrix} \cdot \begin{bmatrix} \mathbf{A}^I \\ \mathbf{B}^{II} \end{bmatrix} \quad (2-13)$$

The elements in the coupling matrices [eq.(2-16)] are

$$M_{ij}^{e1-e\Pi} = 4C_i^1 \left[\sum_{r=0}^{n^{e1a}} A_{rj}^{e1a} (-J_{i,rj}^1 J_{i,rj}^2 + J_{i,rj}^3 J_{i,rj}^4) + \sum_{s=0}^{n^{e1b}} A_{rj}^{e1b} \delta_{i,sj} (-J_{i,sj}^5 + k_{yi}^{e1} k_{ysj}^{e1b} J_{i,sj}^6) + \sum_{t=0}^{n^{e1c}} A_{tj}^{e1c} (J_{i,tj}^7 J_{i,tj}^8 + J_{i,tj}^9 J_{i,tj}^{10}) \right] \quad (3-28)$$

where

$$\begin{aligned} J_{i,rj}^1 &= k_{xi}^{e1} \int_{a_1}^{a/2} \sin k_{xi}^{e1} x \cos k_{xj}^{e1a} (x - a/2) dx & J_{i,rj}^2 &= \sqrt{\frac{2}{b_1}} \int_0^{b_1} \frac{\cos k_{yi}^{e1} y}{\sqrt{1 + \delta_{0i}}} \frac{\cos k_{yrj}^{e1a} y}{\sqrt{1 + \delta_{0rj}}} dy \\ J_{i,rj}^3 &= \frac{1}{k_{xj}^{e1a}} \int_{a_1}^{a/2} \cos k_{xi}^{e1} x \sin k_{xj}^{e1a} (x - a/2) dx & J_{i,rj}^4 &= \sqrt{\frac{2}{b_1}} k_{yi}^{e1} k_{yrj}^{e1a} \int_0^{b_1} \sin k_{yi}^{e1} y \sin k_{yrj}^{e1a} y dy \\ J_{i,sj}^5 &= k_{xi}^{e1} k_{xj}^{e1b} \int_0^{a_1} \sin k_{xi}^{e1} x \sin k_{xj}^{e1b} x dx & J_{i,sj}^6 &= \int_0^{a_1} \cos k_{xi}^{e1} x \cos k_{xj}^{e1b} x dx \\ J_{i,tj}^7 &= k_{xi}^{e1} k_{xj}^{e1c} \int_{a_1}^{a_2} \sin k_{xi}^{e1} x \sin k_{xj}^{e1c} (x - a_2) dx & J_{i,tj}^8 &= \sqrt{\frac{2}{d}} \int_{b_2}^{b/2} \frac{\cos k_{yi}^{e1} y}{\sqrt{1 + \delta_{0i}}} \frac{\cos k_{ytj}^{e1c} (y - b_2)}{\sqrt{1 + \delta_{0tj}}} dy \\ J_{i,tj}^9 &= \int_{a_1}^{a_2} \cos k_{xi}^{e1} x \cos k_{xj}^{e1c} (x - a_2) dx & J_{i,tj}^{10} &= \sqrt{\frac{2}{d}} k_{yi}^{e1} k_{ytj}^{e1c} \int_{b_2}^{b/2} \sin k_{yi}^{e1} y \sin k_{ytj}^{e1c} (y - b_2) dy \end{aligned} \quad (3-29)$$

and

$$M_{ij}^{m1-e\Pi} = 4D_i^1 \left[\sum_{r=0}^{n^{m1a}} A_{rj}^{m1a} (-J_{i,rj}^1 J_{i,rj}^2 - J_{i,rj}^3 J_{i,rj}^4) + \sum_{s=0}^{n^{m1b}} A_{rj}^{m1b} \frac{\sqrt{b}}{2} \delta_{i,sj} (-k_{ysj}^{m1b} J_{i,sj}^5 + k_{yi}^{m1} J_{i,sj}^6) + \sum_{t=0}^{n^{m1c}} A_{tj}^{m1c} (-J_{i,tj}^7 J_{i,tj}^8 + J_{i,tj}^9 J_{i,tj}^{10}) \right] \quad (3-30)$$

where

$$\begin{aligned} J_{i,rj}^1 &= \frac{k_{xi}^{m1}}{k_{xj}^{m1a}} \int_{a_1}^{a/2} \cos k_{xi}^{m1} x \sin k_{xj}^{m1a} (x - a/2) dx & J_{i,rj}^2 &= \sqrt{\frac{2}{b_1}} k_{yrj}^{m1a} \int_0^{b_1} \sin k_{yi}^{m1} y \sin k_{yrj}^{m1a} y dy \\ J_{i,rj}^3 &= \int_{a_1}^{a/2} \sin k_{xi}^{m1} x \cos k_{xj}^{m1a} (x - a/2) dx & J_{i,rj}^4 &= \sqrt{\frac{2}{b_1}} k_{yi}^{m1} \int_0^{b_1} \cos k_{yi}^{m1} y \frac{\cos k_{yrj}^{m1a} y}{\sqrt{1 + \delta_{0rj}}} dy \end{aligned}$$

$$\begin{aligned}
J_{i,sj}^5 &= k_{xi}^{mI} \int_0^{a_1} \cos k_{xi}^{mI} x \cos k_{xj}^{eIIb} x \, dx & J_{i,sj}^6 &= k_{xj}^{eIIb} \int_0^{a_1} \sin k_{xi}^{mI} x \sin k_{xj}^{eIIb} x \, dx \\
J_{i,tj}^7 &= k_{xi}^{mI} \int_{a_1}^{a_2} \cos k_{xi}^{mI} x \cos k_{xj}^{eIIc} (x - a_2) \, dx & J_{i,tj}^8 &= \sqrt{\frac{2}{d}} k_{yj}^{eIIc} \int_{b_2}^{b/2} \sin k_{yi}^{mI} y \sin k_{yj}^{eIIc} (y - b_2) \, dy \\
J_{i,tj}^9 &= k_{xj}^{eIIc} \int_{a_1}^{a_2} \sin k_{xi}^{mI} x \sin k_{xj}^{eIIc} (x - a_2) \, dx & J_{i,tj}^{10} &= \sqrt{\frac{2}{d}} k_{yi}^{mI} \int_{b_2}^{b/2} \cos k_{yi}^{mI} y \frac{\cos k_{yj}^{eIIc} (y - b_2)}{\sqrt{1 + \delta_{0ij}}} \, dy
\end{aligned} \tag{3-31}$$

and

$$\begin{aligned}
M_{ij}^{mI-mII} &= 4D_i^I \left[\sum_{r=0}^{n^{mIIa}} A_{rj}^{mIIa} (-J_{i,rj}^1 J_{i,rj}^2 + J_{i,rj}^3 J_{i,rj}^4) + \right. \\
&\quad \left. \sum_{s=0}^{n^{mIb}} A_{rj}^{mIb} \frac{\sqrt{b}}{2} \delta_{i,sj} (J_{i,sj}^5 + k_{yi}^{mI} k_{ysj}^{mIb} J_{i,sj}^6) + \sum_{t=0}^{n^{mIc}} A_{tj}^{mIc} (J_{i,tj}^7 J_{i,tj}^8 + J_{i,tj}^9 J_{i,tj}^{10}) \right]
\end{aligned} \tag{3-32}$$

where

$$\begin{aligned}
J_{i,rj}^1 &= k_{xi}^{mI} k_{xj}^{mIIa} \int_{a_1}^{a/2} \cos k_{xi}^{mI} x \sin k_{xj}^{mIIa} \left(x - \frac{a}{2} \right) dx & J_{i,rj}^2 &= \sqrt{\frac{2}{b_1}} k_{yrj}^{mIIa} \int_0^{b_1} \sin k_{yi}^{mI} y \sin k_{yrj}^{mIIa} y \, dy \\
J_{i,rj}^3 &= \int_{a_1}^{a/2} \sin k_{xi}^{mI} x \cos k_{xj}^{mIIa} \left(x - \frac{a}{2} \right) dx & J_{i,rj}^4 &= \sqrt{\frac{2}{b_1}} k_{yi}^{mI} k_{yrj}^{mIIa} \int_0^{b_1} \cos k_{yi}^{mI} y \cos k_{yrj}^{mIIa} y \, dy \\
J_{i,sj}^5 &= k_{xi}^{mI} \int_0^{a_1} \cos k_{xi}^{mI} x \cos k_{xj}^{mIb} x \, dx & J_{i,sj}^6 &= \frac{1}{k_{xj}^{mIb}} \int_0^{a_1} \sin k_{xi}^{mI} x \sin k_{xj}^{mIb} x \, dx \\
J_{i,tj}^7 &= k_{xi}^{mI} \int_{a_1}^{a_2} \cos k_{xi}^{mI} x \cos k_{xj}^{eIIc} (x - a_2) \, dx & J_{i,tj}^8 &= \sqrt{\frac{2}{d}} \int_{b_2}^{b/2} \sin k_{yi}^{mI} y \sin k_{yj}^{eIIc} (y - b_2) \, dy \\
J_{i,tj}^9 &= k_{xj}^{eIIc} \int_{a_1}^{a_2} \sin k_{xi}^{mI} x \sin k_{xj}^{eIIc} (x - a_2) \, dx & J_{i,tj}^{10} &= \sqrt{\frac{2}{d}} k_{yi}^{mI} k_{ytj}^{eIIc} \int_{b_2}^{b/2} \cos k_{yi}^{mI} y \cos k_{ytj}^{eIIc} (y - b_2) \, dy
\end{aligned} \tag{3-33}$$

(recall $d = (b/2) - b_2$). Since this modal scattering matrix is for a lossless and reciprocal discontinuity, it satisfies the symmetrical and orthogonal relations [91], i.e.,

$$\mathbf{S} = \mathbf{S}^T = \mathbf{S}^{-1} \tag{3-34}$$

and this was used as one of the criteria to verify the accuracy of the computer algorithm.

Convergence analysis on a single discontinuity indicated it was achieved by using 25 modes in regions I and II, with 8 expansion terms for the cross-section functions of region IIb. The number of expansion terms in regions IIa and IIc are always determined from a ratio of subregion dimensions.

Also note, to derive the scattering matrix for the corresponding inverse discontinuity, namely, the T-septum-to-rectangular waveguide, the submatrix elements are interchanged in the scattering matrix of the original structure, that is,

$$\begin{bmatrix} \mathbf{A}^{\text{II}} \\ \mathbf{B}^{\text{I}} \end{bmatrix} = \begin{bmatrix} \mathbf{S}_{22} & \mathbf{S}_{21} \\ \mathbf{S}_{12} & \mathbf{S}_{11} \end{bmatrix} \cdot \begin{bmatrix} \mathbf{B}^{\text{II}} \\ \mathbf{A}^{\text{I}} \end{bmatrix}. \quad (3-35)$$

Using the Generalized S-matrix Method in Appendix A, these scattering matrices may now be combined or cascaded with any other discontinuity.

The interested reader is referred to Appendix B for the electric field distribution at the rectangular-to-T-septum waveguide discontinuity, which shows the convergence by increasing the number of modes of the electric field.

3.4 COMPONENT DESIGN

The advantages of the T-septum waveguide can be clearly demonstrated in component design. This section presents rigorous computer-aided design for three classes of components, namely, bandpass filters, transformers and diplexers. The three basic building block discontinuities employed in these components are rectangular-to-T-septum waveguide, the double-plane step, and the *E*-plane T-junction.

3.4.1. Bandpass Filters

The introduction of a T-septum into a rectangular waveguide results in a significant lowering of the dominant mode cut-off frequency and, therefore, it can be used to produce evanescent-mode waveguide filters. These filters are well known for their wide stopbands and their small size compared to conventional coupled resonator filters. Evanescent-mode filters, which are the microwave analog of lumped inductance

filters with series inductance coupling, are constructed from resonators within a below cut-off waveguide. Resonators are formed by introducing appropriate capacitive obstacles at suitable intervals along the waveguide; the magnitude of the series inductance is dictated by the separation between these capacitive obstacles. Currently, the common techniques applied to create a resonator in the below cut-off waveguide include capacitive screws [92], round posts [93, 95], ridges [14, 61, 95] and E -plane fins [60]. In T-septum waveguide filter design, the T-septums provide the necessary capacitance for the resonator elements.

The length of an evanescent-mode filter structure decreases with a corresponding reduction in the dimension of the cross-section for the waveguide operating below cut-off. This tendency, however, imposes higher requirements on the resonator structure because its cross-section must provide for a reduction in the cut-off frequency of the below cut-off waveguide to approximately that of the much larger input/output waveguide. Since the T-septum offers better performance in terms of bandwidth enhancement and cut-off frequency reduction [36] compared with the alternate approaches, this technology is ideally suited for evanescent-mode filter applications.

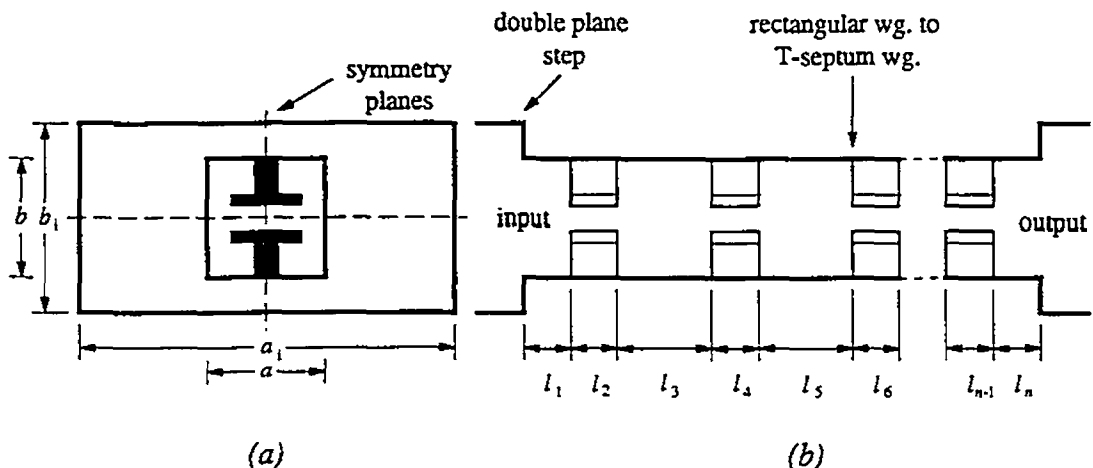


FIGURE 3.5 Structure of an evanescent-mode bandpass filter: (a) end view; (b) side view (cf. Figure 1.4(a) for a cut-away view of the filter).

The structure of an evanescent-mode bandpass filter with T-septums is shown in Figure 3.5. The filter structure is decomposed into two key building block discontinuities: a double-plane step discontinuity from the above cut-off input waveguide to the below cut-off filter section, and the rectangular-to-T-septum waveguide discontinuity. Note that for the corresponding inverse structure (e.g., the discontinuity from the below cut-off to above cut-off waveguide), the related modal scattering matrix is derived by interchanging the corresponding submatrix elements in the original structure as demonstrated in Section 3.3. The scattering matrix of the complete filter structure is calculated by cascading these discontinuities with known scattering matrices of the intermediate homogeneous waveguide sections of finite length using the algorithms in Appendix A.

The design of the T-septum waveguide evanescent-mode filter is carried out in four steps. First, the below cut-off waveguide dimensions are selected for a fundamental-mode cut-off at approximately twice the midband frequency of the filter. Second, the dimensions of the T-septum are determined to provide a cut-off frequency at approximately that of the input/output waveguide. Third, assuming as a rough approximation that the behavior for the below-cutoff coupling sections is purely inductive, the number of resonators as well as the initial lengths of the T-septum and below cut-off sections are calculated using standard filter theory and impedance inverters [96]. Fourth, individual section lengths are systematically altered by optimization procedures to approximate the specified filter characteristic. For this last step, an error function, defined by least squares, is minimized by random search for a global minimum or by the Fletcher-Reeves method for a local minimum, with respect to a parameter vector that contains the coupling and resonator lengths. All the filter designs in this section were optimized using 25 modes and 8 expansion terms in region IIb of the T-septum cross-section. The CPU time for the analysis of the filter parameters per frequency point is less than two minutes on an IBM RISC 6000/530 workstation.

Figure 3.6 shows the response of a three-resonator evanescent-mode filter for 9.94 GHz in the X-band. The design is optimized for a bandwidth of 482 MHz and a return loss better than 25 dB. Although the cut-off frequency of the waveguide in the filter section is 21.2 GHz, the second passband is shifted beyond 28.0 GHz. For a symmetric configuration, the next higher mode in the X-band output waveguide begins to

propagate at 19.7 GHz. As the dashed line shows, this fact does not contribute to any deterioration of the filter response at higher frequencies. Note that at the second harmonic frequency of 30 GHz, attenuation values greater than 55 dB are obtained making the design suitable for X-band communication systems. The total component length is 18.22 mm.

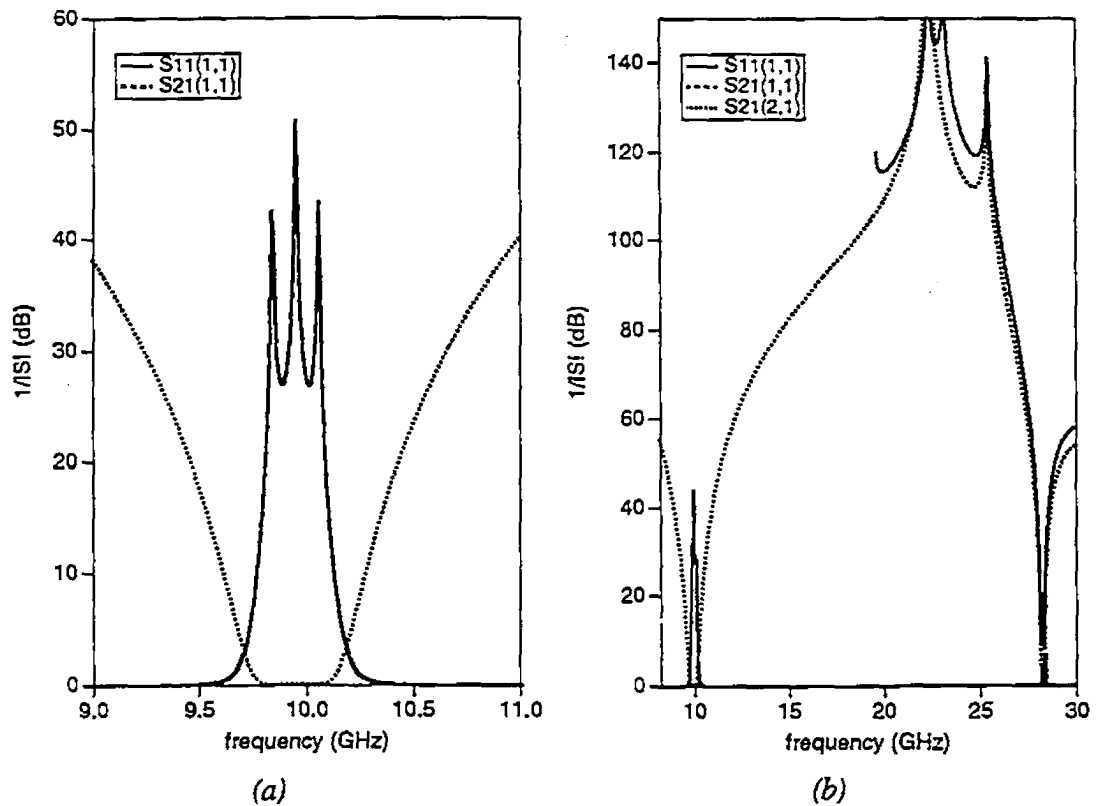


FIGURE 3.6 (a) Calculated transmission and reflection of an X-band three-resonator evanescent-mode T-septum waveguide filter; (b) stopband response. Dimensions (mm): $a_i = 22.86$, $b_i = 10.16$, $a = 7.06$, $b = 6.98$, $a_1 = 1.0$, $a_2 = 2.556$, $b_1 = 0.5$, $b_2 = 1.5$, $l_1 = l_7 = 0.49$, $l_2 = l_6 = 0.51$, $l_3 = l_5 = 7.60$ and $l_4 = 1.20$ (cf. Figures 3.1 and 3.5).

Figure 3.7 shows a five-resonator structure with a center frequency of 9.97 GHz and bandwidth of 366 MHz for comparison with Figure 3.6. Note that, not only is the skirt selectivity and stopband attenuation significantly improved as might be expected by adding two resonators, but also the attenuation of the second harmonic (30 GHz) is

almost doubled. However, the length of the filter is twice that of the three-resonator filter. A three-resonator millimeter-wave Ka-band filter design for a centre frequency of 31.96 GHz and a bandwidth of 1.55 GHz is illustrated in Figure 3.8. The calculated minimum passband return loss is 27 dB. The optimized filter component has a length of only 5.7 mm and excellent stopband characteristics.

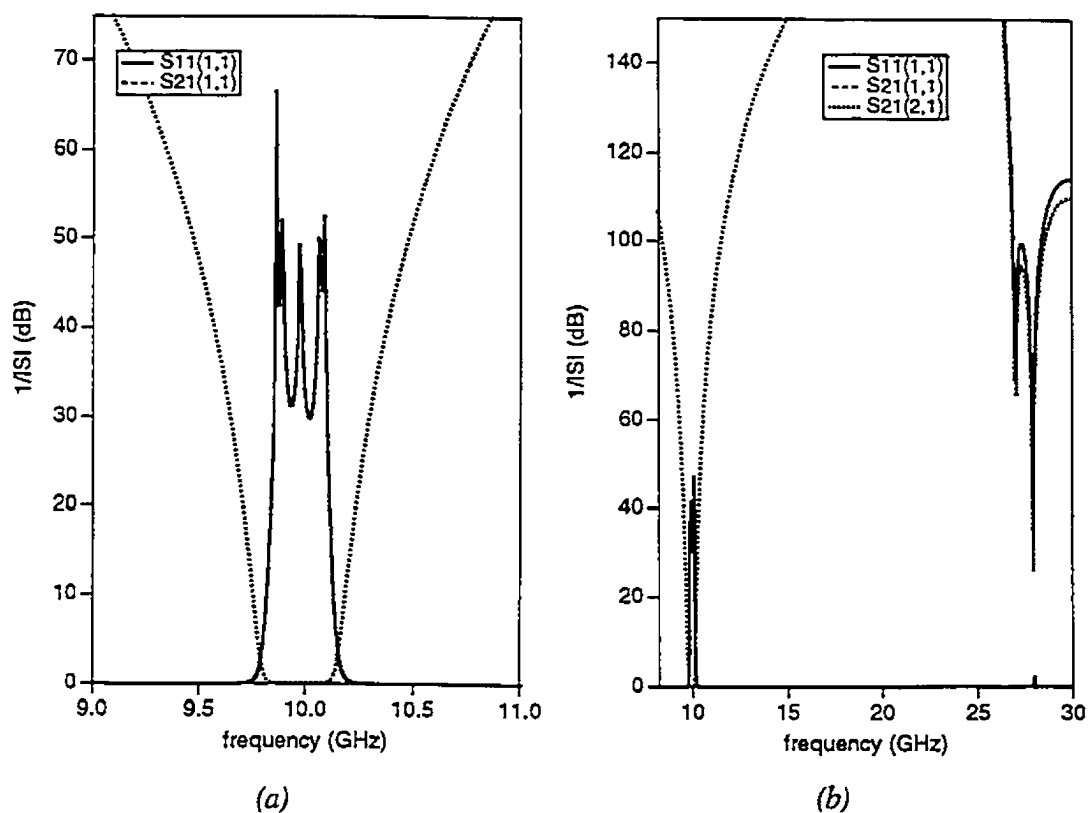


FIGURE 3.7 (a) Calculated transmission and reflection of an X-band five-resonator evanescent-mode T-septum waveguide filter; (b) stopband response. Dimensions (mm): $a_i = 22.86$, $b_i = 10.16$, $a = 7.06$, $b = 6.98$, $a_1 = 1.0$, $a_2 = 2.53$, $b_1 = 0.49$, $b_2 = 1.49$, $l_1 = l_{11} = 0.47$, $l_2 = l_{10} = 0.488$, $l_3 = l_9 = 7.85$, $l_4 = l_8 = 0.983$, $l_5 = l_7 = 8.59$ and $l_6 = 0.983$ (cf. Figures 3.1 and 3.5).

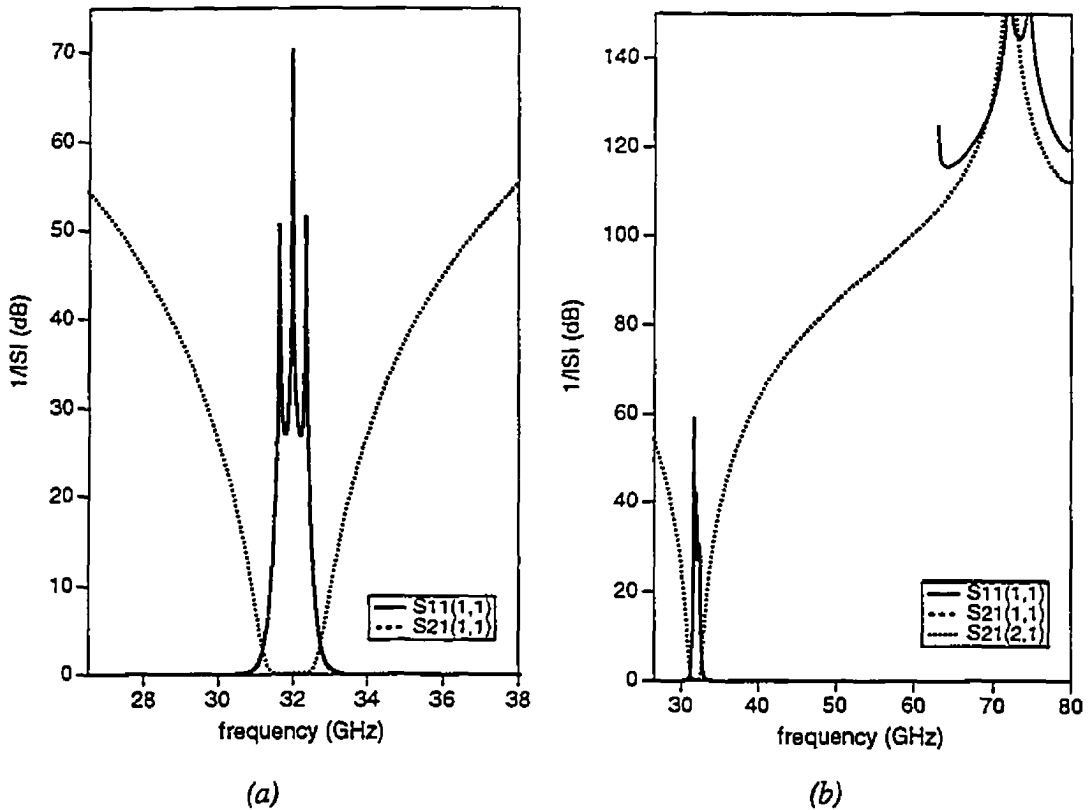


FIGURE 3.8 (a) Calculated transmission and reflection of a Ka-band three-resonator evanescent-mode T-septum waveguide filter; (b) stopband response. Dimensions (mm): $a_i = 7.112$, $b_i = 3.161$, $a = 2.1964$, $b = 2.1716$, $a_1 = 0.3111$, $a_2 = 0.7952$, $b_1 = 0.1556$, $b_2 = 0.4667$, $l_1 = l_7 = 0.1524$, $l_2 = l_6 = 0.1587$, $l_3 = l_5 = 2.2644$ and $l_4 = 0.3174$ (cf. Figures 3.1 and 3.5).

In order to verify the computer-aided analysis and design procedure, the theoretically predicted filter response is compared with measured results of the three-resonator X-band prototype in Figure 3.9. Good agreement is demonstrated with the experimental measurements taken from the filter prototype with one notable exception, namely, a dissipation loss of 2.5 dB within the passband. Because a similar result occurs with measurements from a diplexer to be presented later in the thesis, a discussion of the reason for the loss will be deferred until then (cf. Section 3.4.3). Figure 3.9(a) shows this dissipation loss, but it also shows a low return loss of 13 dB. This low return loss is in agreement with revised predictions based on the manufactured prototype, which failed to reproduce the precisely centred double-plane step from the X-band waveguide to the

below cutoff waveguide filter structure called for in the design. This flaw in construction accounts for the return loss. Referring to Figure 3.9(b) it should be noted that the out-of-band return loss behaviour is in excellent agreement with predicted results up to 40 GHz. Beyond 12.4 GHz a series of waveguide transformers have been used to extend the measurements into the Ka-band. Overmoding in the X-band input/output waveguides seems to be responsible for the measured noise beyond 12.4 GHz.

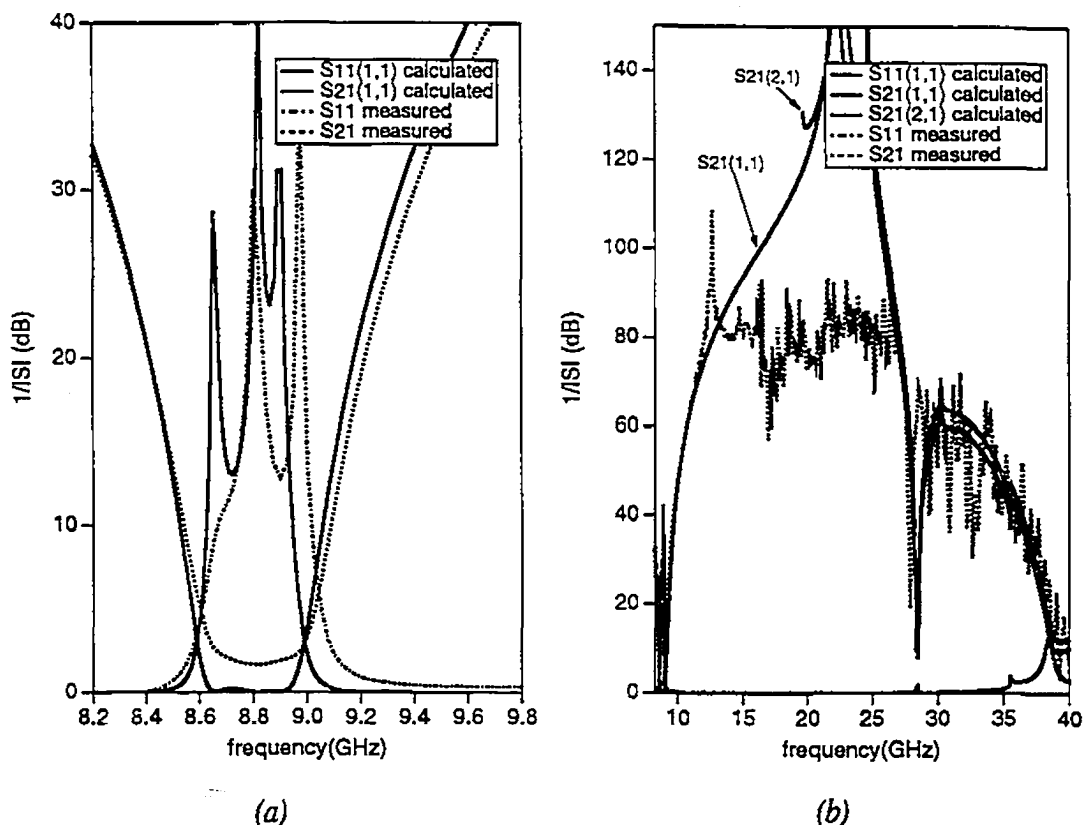


FIGURE 3.9 (a) Comparison between the measured and calculated response of an X-band three-resonator filter prototype; (b) stopband response. Dimensions (mm): $a_i = 22.86$, $b_i = 10.16$, $a = 7.0$, $b = 6.95$, $a_1 = 0.94$, $a_2 = 2.49$, $b_1 = 0.3$, $b_2 = 1.32$, $l_1 = l_7 = 0.54$, $l_2 = l_6 = 0.5$, $l_3 = l_5 = 7.68$ and $l_4 = 0.9$ (cf. Figures 3.1 and 3.5).

A photograph of this evanescent-mode T-septum waveguide filter prototype (displayed in a partially assembled state) with its feeding X-band waveguide is shown in Figure 3.10. A split-block waveguide housing is used to sandwich the two T-

septum inserts. Note that the filter component is extremely small compared to a ridge waveguide design for a comparable frequency range [61]. This is so because of the large bandwidth of the T-septum waveguide, i.e., its capability to reduce significantly the cut-off frequency. With an overall length of less than 20 mm, this design is one of the most space efficient bandpass configurations proposed thus far.

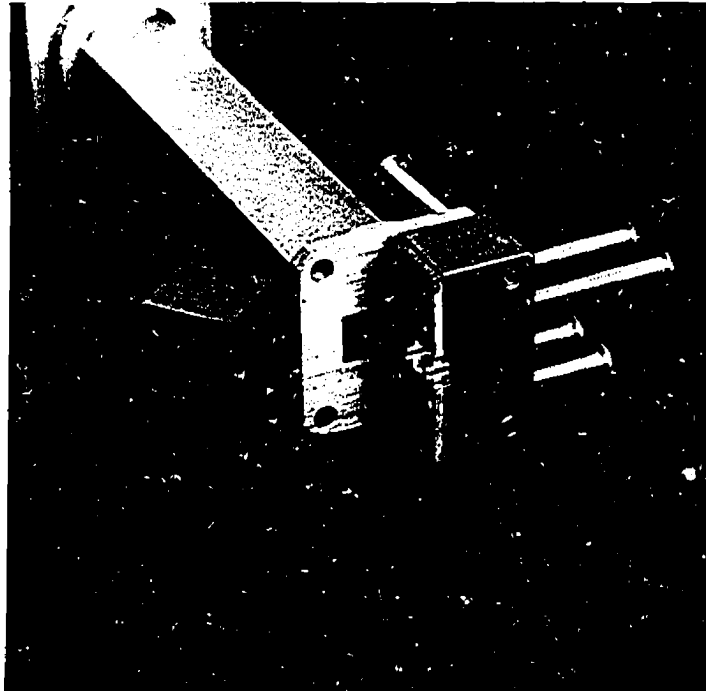


FIGURE 3.10 *Photograph of the opened evanescent-mode T-septum waveguide filter prototype with feeding X-band waveguide.*

3.4.2. Transformers

Filter theory may also be applied to the design of impedance transformers used for broadband matching into discrete discontinuities, such as input sections to low-pass waveguide filters. Figure 3.11 shows the geometry of a typical T-septum waveguide transformer. It is composed of a series of T-septum waveguides of different cross-section dimensions located between a standard rectangular waveguide input and a T-septum waveguide output. The dominant mode cut-off frequency of the rectangular input waveguide is approximately equal to the dominant mode cut-off frequency of the T-

septum output waveguide which is of significantly smaller physical dimension. Similar transformers have been successfully designed with ridge waveguide technology [97].

The two basic building block discontinuities employed in the design of such a transformer are the rectangular-to-T-septum waveguide as in the input to section 1 of Figure 3.11 and the T-septum-to-T-septum waveguide as seen in the rest of diagram. The scattering matrix of this latter discontinuity is arrived at by cascading the scattering matrices of the three discontinuities, namely, the T-septum-to-rectangular waveguide, the double-plane waveguide step, and the rectangular-to-T-septum waveguide, while reducing the length to zero.

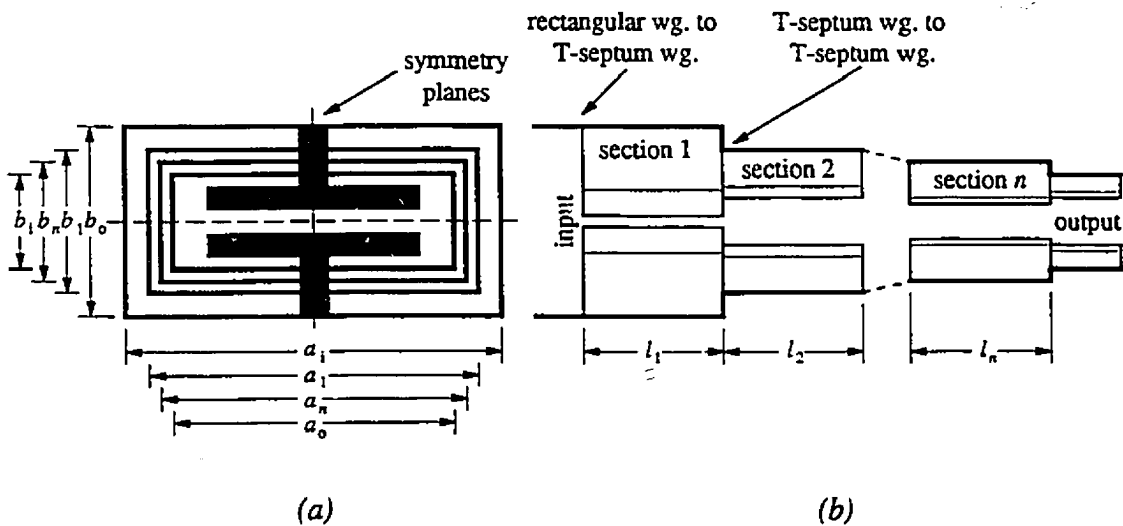


FIGURE 3.11 Structure of a T-septum waveguide transformer: (a) end view; (b) side view (cf. Figure 1.4(b) for a cut-away view of the transformer).

The design procedure is based on the standard quarter wavelength impedance transformation theory to yield high return loss specifications. The transformer is designed by first calculating the characteristic impedance of each section assuming that their lengths are quarter wavelength. From this are then calculated the cross-section dimensions of each T-septum of the component. Finally, the design is completed by inclusion within an optimization routine.

Figure 3.12 depicts the return loss of an X-band three section transformer

at a design centre frequency of 10.5 GHz. A return loss behaviour better than 30 dB is maintained within the frequency band of the transformer. As in the case of the filter components, the design data is easily transferable to other common waveguide bands by suitable frequency scaling relations for the dimensions.

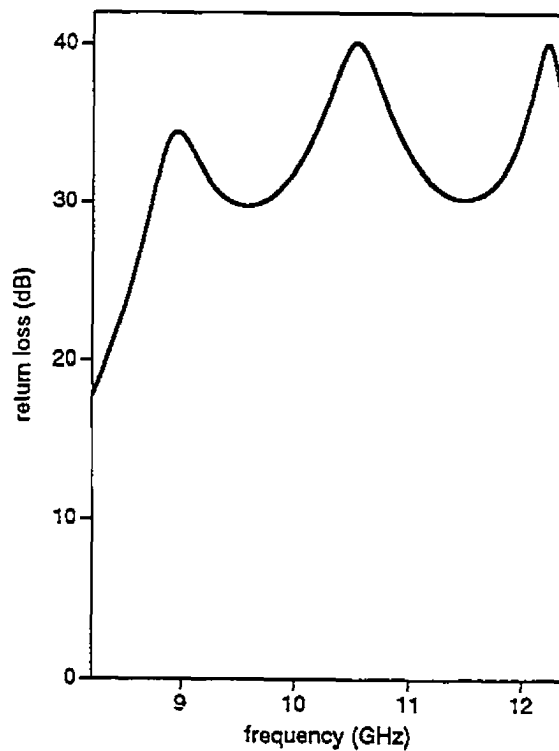


FIGURE 3.12 Input return loss of an optimized three-section transformer.
Dimensions (mm):

SECTION #	a	b	a_1	a_2	b_1	b_2	l
input:	22.860	11.430					
Section 1:	21.150	10.575	6.345	9.518	4.354	4.618	8.200
Section 2:	17.250	8.625	5.175	7.763	2.562	2.778	8.000
Section 3:	14.150	7.075	4.245	6.368	1.487	1.664	8.400
output:	13.000	6.500	3.900	5.850	1.139	1.302	

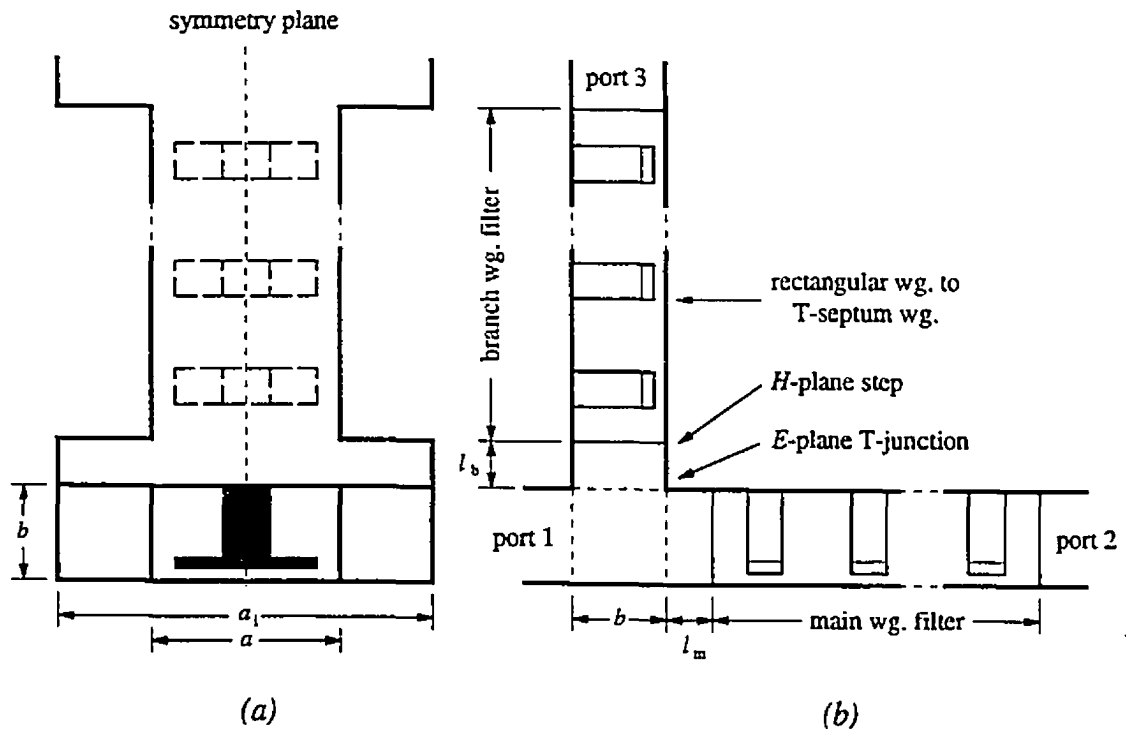


FIGURE 3.13 Structure of a T-septum waveguide diplexer: (a) end view; (b) side view (cf. Figure 1.5(a) for a cut-away view of the diplexer).

3.4.3. Diplexers

This section introduces an integrated waveguide diplexer based on T-septum waveguide filter technology; the diplexer is illustrated in Figure 3.13. The advent of integrated waveguide *E*-plane technology places an increasing demand on millimeter-wave diplexing units for transmit-receive channel separation. While physical channel separation is commonly accomplished by waveguide N-furcations or T-junctions, the filter configurations and their performance distinguish the different designs. Designs to date have included *E*-plane filters [72-74], elliptic function filters [98], and lowpass-highpass arrangements [99]. Until now, the relatively large physical size of these components makes them less attractive for use in modern integrated microwave communication systems. By utilizing T-septum waveguide technology, the resulting smaller filter configurations will automatically contribute to light-weight, and compact multiplexer designs. The rigorous numerical model for the diplexer will eliminate the

need for discontinuity-compensating irises and steps which are currently in use to improve diplexer performance.

As shown in Figure 3.13, three basic building block discontinuities are used for this component: the E -plane T-junction, the H -plane step, and the rectangular-to-T-septum waveguide. The scattering matrix of the overall component is calculated by the combination of the scattering matrices of these three basic discontinuities within the component. For the rectangular-to-T-septum waveguide discontinuity, the analysis follows closely that of Sections 3.2 and 3.3, with the exception that the T-septum cross-section functions are modified because single T-septums are used for component compactness.

The design of the diplexer is carried out in two steps. First, the evanescent-mode T-septum channel filters are designed using the procedure described in Section 3.4.1. Second, the filters are connected to the waveguide T-junction, and only the lengths between the T-junction and the H -plane steps are optimized by the same routines used in the filter design. An overall optimization, with the filter sections, may be included to fine tune the diplexer's response by improving the return loss in the passbands. General design procedures for waveguide diplexers and multiplexers are presented in [100, 101].

Figure 3.14 presents the transmission and input return loss responses of the X-band integrated T-septum waveguide diplexer for center frequencies of 8.75/9.97 GHz with bandwidths of approximately 4.1 percent. The cross-sections of the waveguide ports are 22.86 mm by 3.5 mm, those of the evanescent-mode sections are 7.112 mm by 3.5 mm. Both filters are less than 22 mm long with typically 22 mm connecting lengths to the T-junction. These dimensions make it possible to manufacture the diplexer from a cube of less than 45 mm. As shown, the crossover attenuation is 26 dB, and the input return loss is better than 25 dB. Figure 3.14(b) displays the excellent stopband characteristics of the diplexer up to 28 GHz. As indicated in Section 3.4.1, this is a fundamental advantage of T-septum waveguide filter technology.

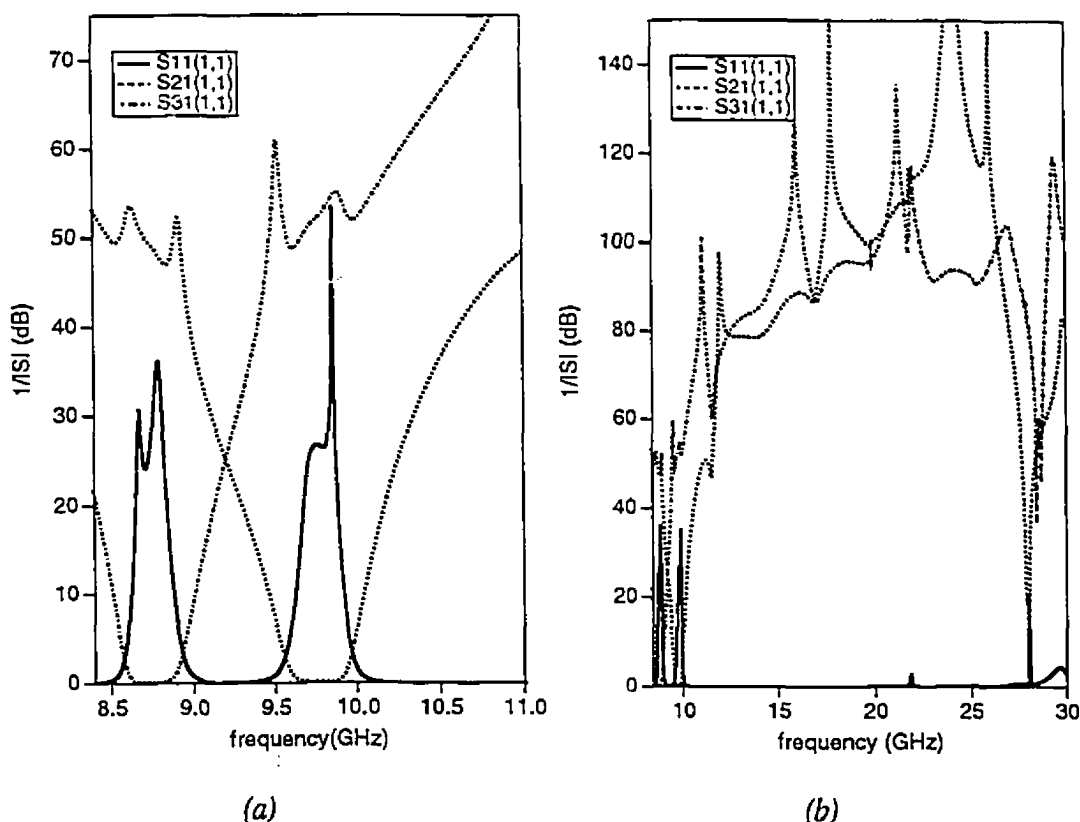


FIGURE 3.14 (a) Transmission and input reflection behavior of an integrated T-septum X-band waveguide diplexer; (b) stopband response. Dimensions (mm): $a_1 = 22.86$, $a = 7.112$, $b = 3.5$. Main waveguide filter: $a_1 = 1.0$, $a_2 = 2.556$, $b_1 = 0.5$, $b_2 = 1.5$, $l_1 = l_7 = 0.905$, $l_2 = l_6 = 0.895$, $l_3 = l_5 = 7.73$ and $l_4 = 1.17$. Branch waveguide filter: $a_1 = 1.0$, $a_2 = 2.556$, $b_1 = 0.5$, $b_2 = 1.5$, $l_1 = l_7 = 0.3750$, $l_2 = l_6 = 2.17$, $l_3 = l_5 = 7.15$ and $l_4 = 2.836$ (cf. Figures 3.1 and 3.12).

The diplexer design can be scaled to any other waveguide band having an identical frequency behaviour with respect to the fundamental-mode frequency of the input-port waveguide. This is demonstrated in Figure 3.15 for operation in Ka-band. The channel passbands are centered at 28.14/31.37 GHz with bandwidths of 4.1 percent, and a stopband beyond 80 GHz is obtained.

In order to verify the computer-aided analysis and design procedure, the theoretically predicted transmission and reflected response is compared with measured results of an integrated T-septum waveguide diplexer with two three-resonator evanescent-mode filters (Figure 3.16). Excellent agreement with predicted results is

achieved with the exception of a high dissipation loss in the magnitude of 2.5 dB within the passbands of both filters. The dissipation loss measured from both the diplexer and the filter mentioned in Section 3.4.1 suggests that such loss is inherent in this particular configuration of the design. The dissipation loss, in general, can be attributed to two sources, namely, attenuation occurring along the longitudinal axis and the energy dissipated on the metallic faces of the double-plane step and/or rectangular-to-T-septum discontinuities. Some simple calculations will demonstrate that the latter of these two will prove to be the major locus of the problem.

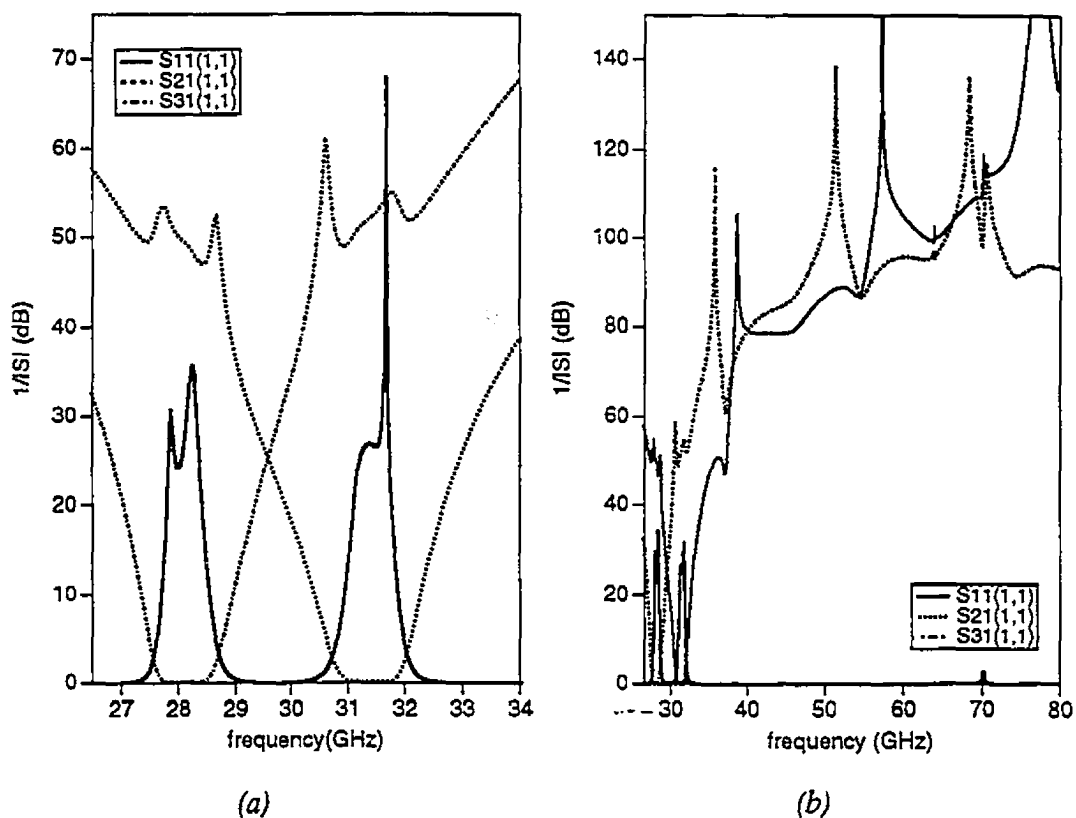


FIGURE 3.15 (a) Transmission and input reflection behavior of an integrated T-septum Ka-band waveguide diplexer; (b) stopband response. Dimensions (mm): $a_1 = 7.112$, $a = 2.2126$, $b = 1.089$. Main waveguide filter: $a_1 = 0.3111$, $a_2 = 0.7952$, $b_1 = 0.1556$, $b_2 = 0.4667$, $l_1 = l_7 = 0.2815$, $l_2 = l_5 = 0.2784$, $l_3 = l_5 = 2.4149$ and $l_4 = 0.364$. Branch waveguide filter: $a_1 = 0.3111$, $a_2 = 0.7952$, $b_1 = 0.1556$, $b_2 = 0.4667$, $l_1 = l_7 = 0.1166$, $l_2 = l_6 = 0.6751$, $l_3 = l_5 = 2.2244$ and $l_4 = 0.4412$ (cf. Figures 3.1 and 3.12).

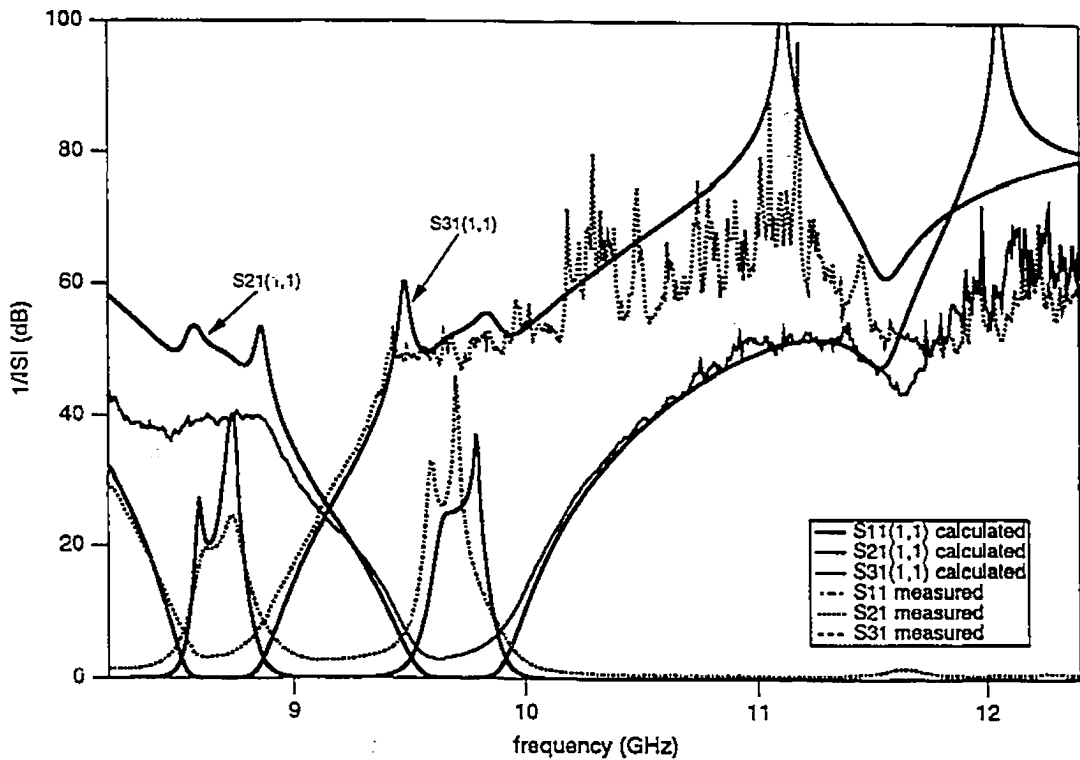


FIGURE 3.16 Comparison between measured and calculated responses of an integrated X-band T-septum diplexer prototype. Dimensions (mm): $a_1 = 22.86$, $a = 7.112$, $b = 3.5$. Main waveguide filter: $a_1 = 1.0$, $a_2 = 2.556$, $b_1 = 0.49$, $b_2 = 1.49$, $l_1 = l_7 = 0.905$, $l_2 = l_6 = 0.895$, $l_3 = l_5 = 7.73$ and $l_4 = 1.17$. Branch waveguide filter: $a_1 = 1.0$, $a_2 = 2.556$, $b_1 = 0.49$, $b_2 = 1.49$, $l_1 = l_7 = 0.3750$, $l_2 = l_6 = 2.17$, $l_3 = l_5 = 7.15$ and $l_4 = 2.836$ (cf. Figures 3.1 and 3.12).

If the waveguide walls have finite conductivity, there will be a continuous longitudinal loss of power to these walls as the modes propagate through the filter. To account for these losses in the model, the propagation constants jk_z may be slightly modified to become $\alpha + jk_z$, where α is an attenuation constant that specifies the rate at which the mode amplitude decays as it progresses. The attenuation constant of a T-septum waveguide normalized to that of a standard rectangular waveguide with the same dominant mode cutoff frequency and outer dimension ratio, has been published by Zhang and Joines in [38]. For the prototype, assuming a conductivity of 17.4 MS/m, the attenuation constant of the T-septum resonator sections is approximately 25 times that of standard or -0.0023 dB/mm at 10 GHz. Thus, with an overall length of 3 mm for the T-

septum sections, the total longitudinal loss is calculated to be -0.007 dB.

Power losses caused by the finite conductivity of the metallic faces in the double-plane step and/or rectangular-to-T-septum discontinuities may be approximated by using the perturbation method [4]. The currents on a lossy metallic surface S are assumed to be the same as the loss-free currents and, hence, are related to the tangential magnetic field by

$$\mathbf{J}_s = \mathbf{n} \times \vec{\mathbf{H}} \quad (3-36)$$

where \mathbf{n} is a unit vector outward directed normal on S . With a finite conductivity σ , the metallic surface may be characterized as exhibiting a surface impedance given by

$$Z_m = \frac{1+j}{\sigma \delta_{sd}} = (1+j)R_m \quad (3-37)$$

where δ_{sd} is the skin depth:

$$\delta_{sd} = \sqrt{\frac{2}{\omega \mu_o \sigma}} \quad (3-38)$$

By integrating the surface currents over S the power loss may be estimated:

$$P_l = \frac{R_m}{2} \iint_S \mathbf{J}_s \cdot \mathbf{J}_s^* ds \quad (3-39)$$

Assuming an input power of 1W and a conductivity of 17.4 MS/m, and by using appropriate generalized scattering matrices and the magnetic field expressions given in eqs.(2-6), the surface currents may be calculated at any transverse metallic face within the filter structure. The results of this calculation have shown that the first and last T-septum resonator sections dissipate approximately 0.32 W. The other surfaces, i.e., the middle resonator and the faces of the double-plane step account for significantly less of the power loss. The total calculated loss for the filter structure by eq.(3-39) is approximately -2.1 dB. The remainder of the loss measured (or -0.4 dB) may be attributed to surface roughness and other minor discrepancies expected within a prototype of this technology. It is precisely the combination of a large double plane step followed in close proximity by

a T-septum resonator that generates the high magnetic field which contributes to the large dissipation loss. A gradual reduction of the X-band input/output waveguide to the below cutoff waveguide could reduce these high magnetic field values. Another solution might be to use T-septum waveguide technology throughout the component system thus eliminating the need for the double-plane step connection.

A photograph of this diplexer prototype is shown in Figure 3.17. A split-block housing is used to sandwich the two T-septum inserts into their corresponding below cut-off waveguide. This photograph shows the compactness of structure achievable by the utilization of the described design technology. The technology is applicable to a wide variety of similar components, the discussion of which, however, is beyond the scope of this thesis.

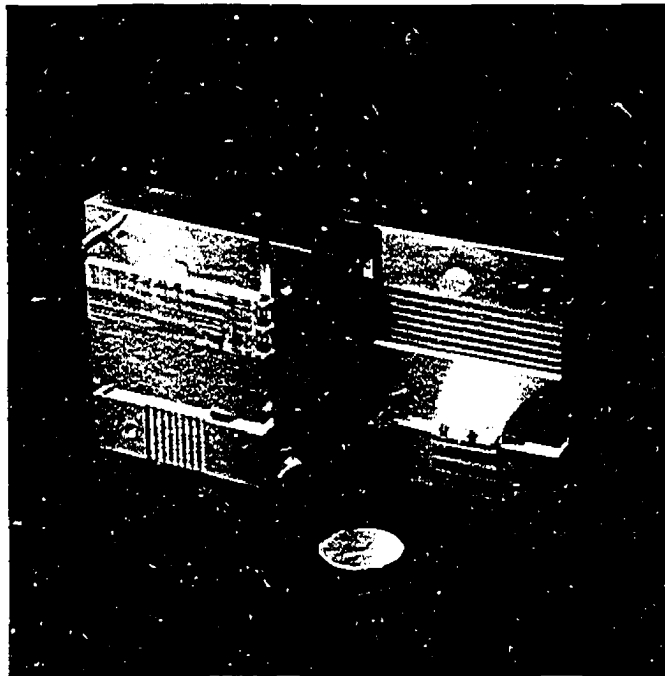


FIGURE 3.17 *Photograph of the opened integrated evanescent-mode T-septum waveguide diplexer prototype.*

4. DISCONTINUITY-DISTORTED T-JUNCTIONS

4.1. INTRODUCTION

A natural progression from nonstandard cross-sections in the two-port waveguide junction is to expand the theoretical and numerical analysis to include nonstandard multi-port junctions. This chapter proposes a new formulation for determining the generalized scattering matrix for such nonstandard multiports with application to waveguide corners and T-junctions having a discontinuity-distorted resonator region.

Waveguide corners and T-junctions form integral parts in the design and realization of waveguide components and systems. For example, as mentioned in Chapter 1, waveguide corners occur naturally in antenna feed systems, and the T-junction is used extensively in waveguide components such as bandstop resonator cavity filters [3], multiplexers [70], power-dividers [75], orthomode transducers [76], and couplers [66]. Chapter 2 calculated the generalized scattering matrix of the simple *E*-plane T-junction. It should be noted that, with respect to its scattering matrix, the waveguide corner may be thought of as a special case of the T-junction, wherein port 2 (cf. Figure 2.2) is short circuited. Hence, the solution presented here for the T-junction is equally applicable to waveguide corners.

With regard to the choice of analytical techniques, as indicated earlier, one of the main advantages of the mode-matching method is that it produces a generalized scattering matrix for the discontinuity. Hence, discontinuities may be cascaded and combined using the algorithms in Appendix A with no restriction resulting from their

physical proximity. Inherent to the nature of the Generalized S-matrix Method is the incorporation of higher-order mode coupling effects. This was demonstrated in Chapter 3 in the case of the T-septum diplexer, where the generalized scattering matrix of the T-junction was combined with that of the filters. The key to the development of accurate computer-aided component design is the precise calculation of the generalized scattering matrices for discontinuities within the component.

In the literature, a rigorous calculation of the T-junction with a discontinuity-distorted resonator has been proposed by Alessandri et al. [102] and Liang et al. [45]. This approach has been appropriately named by Liang as the three plane mode-matching method. Although the resulting matrix for the T-junction is one obtained through a rigorous mode-matching method and does include higher order mode interactions of the discontinuities within the resonator, it is not a generalized scattering matrix, but rather a fundamental-mode scattering matrix. If one is interested only in the dominant mode characteristics of a T-junction, this analysis will suffice (as in, for example, [103]). However, if the intent is to include the T-junction as a building block in a component with other discontinuities, then the generalized scattering matrix will be required so that the higher order modes can be incorporated when these other discontinuities are cascaded in close proximity to the resonator region.

The approach proposed by Alessandri and the similar one by Liang is to model a resonator region with the built-in discontinuities by simulating resonator experiments which result in a modification of the structure and, therefore, avoid the eigenfunction-defective regions. In these experiments, short circuits are placed on the side arm of the T-junction some distance away from the actual resonator region. Using three different positions for the short circuit on the side arm, the scattering matrices of the resulting set of two port junctions are calculated. The fundamental-mode scattering matrix of the overall T-junction is then extracted from this set of two-port scattering matrices.

This three plane mode-matching method is illustrated in Figure 4.1 and is mathematically described as follows: The three shorts are first connected with the reflection coefficients $\Gamma^i, i = 1, 2, 3$ to port 3. The scattering matrices of each of the resulting two-port networks $S^{ci}, i = 1, 2, 3$ (port 1 to port 2) are determined by a rigorous

mode-matching method, i.e.,

$$S^{ci} = \left[\begin{array}{c|c} S_{11}^{ci} & S_{12}^{ci} \\ \hline S_{21}^{ci} & S_{22}^{ci} \end{array} \right] \text{ for } i = 1, 2, 3 \quad (4-1)$$

Then, assuming the scattering matrix of the T-junction is

$$S = \left[\begin{array}{c|c|c} S_{11} & S_{21}^T & S_{31}^T \\ \hline S_{21} & S_{22} & S_{32}^T \\ \hline S_{31} & S_{32} & S_{33} \end{array} \right] \quad (4-2)$$

the relationship between S^{ci} and S can easily be derived:

$$\left. \begin{aligned} S_{11}^{ci} &= S_{11} - S_{13}\Gamma^i(\mathbf{I} + S_{33}\Gamma^i)^{-1}S_{13}^T \\ S_{21}^{ci} &= S_{12}^T - S_{23}\Gamma^i(\mathbf{I} + S_{33}\Gamma^i)^{-1}S_{13}^T \\ S_{22}^{ci} &= S_{22} - S_{23}\Gamma^i(\mathbf{I} + S_{33}\Gamma^i)^{-1}S_{23}^T \end{aligned} \right\} \text{ for } i = 1, 2, 3. \quad (4-3)$$

In the case where the scattering matrices are reduced in size to a single element, solutions to eqs.(4-3) may be found for the fundamental-mode; however, due to the non-linear dependencies in them, the generalized scattering matrix of the T-junction cannot be extracted even when applying the reciprocity and symmetry properties.

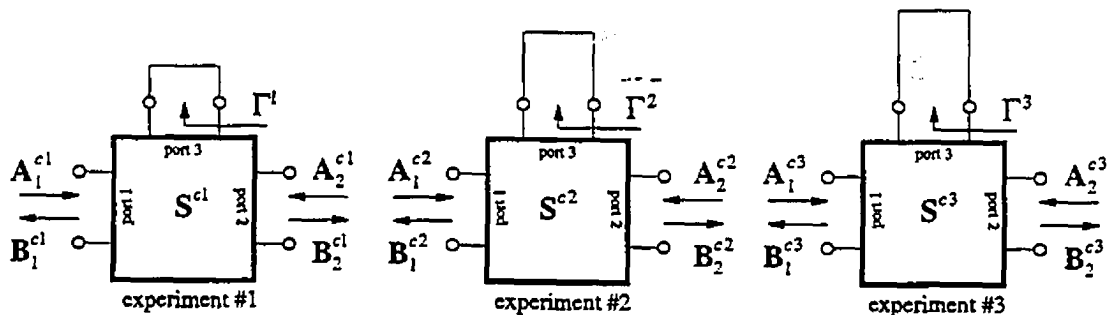


FIGURE 4.1 A three-plane mode-matching method to determine the scattering parameters of a T-junction with discontinuity-distorted resonator region.

Variations of the three-plane mode-matching method, for example, a rotation of the ports from which the experiments are conducted, have been demonstrated in [104]. The generalized theory that proposes experiments on multi-ports to calculate either scattering matrices or reflection coefficients, when one or more of the ports are short circuited, and then to extract the scattering parameters of the original junction, is presented by Ma and Yamashita in [105]. This paper demonstrates the validity of the port reflection coefficient method for the two-port, the three-port, and multi-port cases, as well as the non-linearity inherent therein. However, besides the fundamental-mode limitation, another distinct disadvantage lies in its inclusive nature, particularly when the component to be analyzed contains multiple discontinuities inside and outside the resonator region. The port reflection coefficient method requires the analysis of the entire component including all the discontinuities and extrapolating from this result. On the other hand, the theory proposed in this thesis analyzes discrete building blocks individually and cascades or combines them to construct the design of an eventual component. This process results in a more detailed description of each building block and the interaction between them.

A new approach to the general solution of the scattering matrix for a T-junction with discontinuity-distorted resonator region will be presented in the next section. This technique is based on a rigorous field theory treatment of the discontinuities within the resonator region and the complete mode-matching conditions at the T-junction waveguide apertures. Section 4.3 will apply the general theory to a stepped T-junction, following which, as confirmation of the approach, it will be used to model mitered waveguide corners. The results of this will then be compared with experimental measurements and the finite-element method. The chapter concludes by employing the T-junction as a basic building block in the design of new compact power splitters and orthomode transducers. The orthomode transducer is an excellent example of the cascading of discontinuities in close proximity to the resonator region. Without a generalized scattering matrix of the T-junction, this would not be possible.

4.2. T-JUNCTION WITH DISCONTINUITY-DISTORTED RESONATOR REGION

A general E -plane T-junction with discontinuity-distorted resonator region is depicted in Figure 4.2. It should be noted that, as suggested by the figure, this formulation accommodates discontinuities within the resonator region having variations along any of the coordinate axes. The only restriction required by this approach is the use of mode-matching to calculate the generalized scattering matrices of the discontinuities, with respect to the z -coordinate (looking in from port 1) and with respect to the y -coordinate (looking in from port 3) with electric walls placed at each port opening. In Figure 4.2, for example, the discontinuities along the z -axis are either rectangular-to-ridge waveguide or single E -plane steps, and the discontinuities along the y -axis are either bifurcations or single E -plane steps, all of which lend themselves to analysis using the mode-matching method. Noteworthy is the fact that this restriction also applies to the port reflection coefficient method previously described.

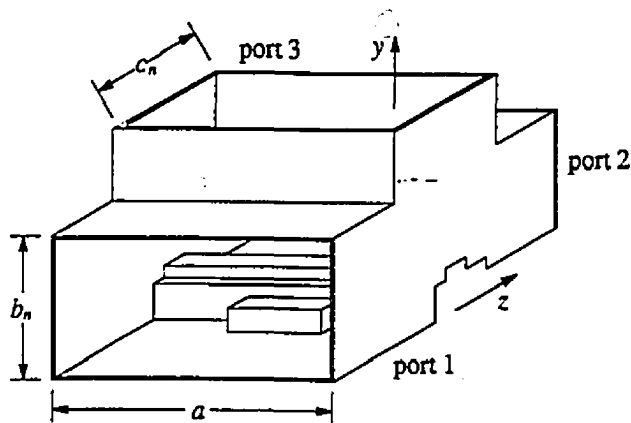


FIGURE 4.2 E -plane T-junction with discontinuity-distorted resonator region viewed from port 1 along the z -axis.

4.2.1 Theoretical Formulation

Before beginning the formulation, it is advantageous to review briefly the approach used to solve for the generalized scattering matrix of the simple T-junction in Chapter 2. The approach is based on the superposition of three solutions for the resonator region with a deliberate placement of short circuits. Each of these solutions is expressed in terms of a single unknown coefficient. Then, by matching the electric field in the port openings, the three unknown coefficients are related to the wave amplitudes in the connecting waveguides. Finally, matching the magnetic field generates the necessary matrix equation for the desired generalized scattering matrix. This formulation also uses the superposition principle for the boundary conditions toward a solution of the Helmholtz equation in the resonator region prior to applying the field continuity conditions at the T-junction apertures.

To formulate the electromagnetic field representation of the discontinuity-distorted T-junction, the configuration is first subdivided into the three cross-sectional regions I, II, and III and the discontinuity-distorted resonator region IV, connected to the three waveguides I to III, as in the simple E -plane T-junction described in Chapter 2. The electromagnetic fields are expressed in waveguides I, II, and III by the longitudinal component of the vector potential, repeated here for convenience

$$\begin{aligned}\bar{F}^I &= \hat{u}_z \psi^{eI}(x, y, z) & \bar{A}^I &= \hat{u}_z \psi^{mI}(x, y, z) \\ \bar{F}^{II} &= \hat{u}_z \psi^{eII}(x, y, z) & \bar{A}^{II} &= \hat{u}_z \psi^{mII}(x, y, z) \\ \bar{F}^{III} &= \hat{u}_z \phi^{eIII}(x, y, z) & \bar{A}^{III} &= \hat{u}_z \phi^{mIII}(x, y, z)\end{aligned}\quad (2-17)$$

where $\psi^{e,m}$ and $\phi^{e,m}$ are the wave potentials given by the general form of eq.(2-2), with appropriate traveling wave amplitudes as shown in Figure 4.3. Recall that the wave potential $\phi^{e,m}$ in region III is simply a cyclic interchange of x, y, z on $\psi^{e,m}$. Using the rectangular waveguide cross-section functions, the expressions for the tangential field components in waveguides I to III are written:

$$\begin{aligned}\bar{\mathbf{E}}_T^I &= [\bar{\mathbf{e}}_T^{eI} \mid \bar{\mathbf{e}}_T^{mI}] \cdot \text{diag}(\sqrt{Z_{p,q}^{e,mI}}) \\ &\quad \left[\text{diag}(\exp[-jk_{p,q}^{e,mI}z])\mathbf{A}^I + \text{diag}(\exp[jk_{p,q}^{e,mI}z])\mathbf{B}^I \right]\end{aligned}$$

$$\begin{aligned} \bar{\mathbf{H}}_T^I &= [\bar{\mathbf{h}}_T^{ei} \mid \bar{\mathbf{h}}_T^{mi}] \cdot \text{diag}(\sqrt{Y_{p,q}^{e,mi}}) \cdot \\ &\quad \left[\text{diag}(\exp[-jk_{z,p,q}^{e,mi}z])\mathbf{A}^I - \text{diag}(\exp[jk_{z,p,q}^{e,mi}z])\mathbf{B}^I \right] \end{aligned} \quad (4-4)$$

$$\begin{aligned} \bar{\mathbf{E}}_T^{\text{II}} &= [\bar{\mathbf{e}}_T^{e\text{II}} \mid \bar{\mathbf{e}}_T^{m\text{II}}] \cdot \text{diag}(\sqrt{Z_{p,q}^{e,m\text{II}}}) \cdot \\ &\quad \left[\text{diag}(\exp[-jk_{z,p,q}^{e,m\text{II}}(z-c_n)])\mathbf{B}^{\text{II}} + \text{diag}(\exp[jk_{z,p,q}^{e,m\text{II}}(z-c_n)])\mathbf{A}^{\text{II}} \right] \\ \bar{\mathbf{H}}_T^{\text{II}} &= [\bar{\mathbf{h}}_T^{e\text{II}} \mid \bar{\mathbf{h}}_T^{m\text{II}}] \cdot \text{diag}(\sqrt{Y_{p,q}^{e,m\text{II}}}) \cdot \\ &\quad \left[\text{diag}(\exp[-jk_{z,p,q}^{e,m\text{II}}(z-c_n)])\mathbf{B}^{\text{II}} - \text{diag}(\exp[jk_{z,p,q}^{e,m\text{II}}(z-c_n)])\mathbf{A}^{\text{II}} \right] \end{aligned} \quad (4-5)$$

$$\begin{aligned} \bar{\mathbf{E}}_T^{\text{III}} &= [\bar{\mathbf{e}}_T^{e\text{III}} \mid \bar{\mathbf{e}}_T^{m\text{III}}] \cdot \text{diag}(\sqrt{Z_{p,q}^{e,m\text{III}}}) \cdot \\ &\quad \left[\text{diag}(\exp[-jk_{y,p,q}^{e,m\text{III}}(y-b_n)])\mathbf{B}^{\text{III}} + \text{diag}(\exp[jk_{y,p,q}^{e,m\text{III}}(y-b_n)])\mathbf{A}^{\text{III}} \right] \\ \bar{\mathbf{H}}_T^{\text{III}} &= [\bar{\mathbf{h}}_T^{e\text{III}} \mid \bar{\mathbf{h}}_T^{m\text{III}}] \cdot \text{diag}(\sqrt{Y_{p,q}^{e,m\text{III}}}) \cdot \\ &\quad \left[\text{diag}(\exp[-jk_{y,p,q}^{e,m\text{III}}(y-b_n)])\mathbf{B}^{\text{III}} - \text{diag}(\exp[jk_{y,p,q}^{e,m\text{III}}(y-b_n)])\mathbf{A}^{\text{III}} \right] \end{aligned} \quad (4-6)$$

where the elements in the mode functions are

$$\left. \begin{aligned} \bar{\mathbf{e}}_{Tp}^{ei} &= \hat{u}_z \times \nabla_z \Psi_p^{ei} & \text{and} & & \bar{\mathbf{e}}_{Tq}^{mi} &= -\nabla_z \Psi_q^{mi} \\ \bar{\mathbf{h}}_{Tp}^{ei} &= -\nabla_z \Psi_p^{ei} & & & \bar{\mathbf{h}}_{Tq}^{mi} &= -\hat{u}_z \times \nabla_z \Psi_q^{mi} \end{aligned} \right\} \text{for } i = \text{I, II} \quad (4-7)$$

and

$$\left. \begin{aligned} \bar{\mathbf{e}}_{Tp}^{e\text{III}} &= \hat{u}_y \times \nabla_y \Phi_p^{e\text{III}} & \text{and} & & \bar{\mathbf{e}}_{Tq}^{m\text{III}} &= -\nabla_y \Phi_q^{m\text{III}} \\ \bar{\mathbf{h}}_{Tp}^{e\text{III}} &= -\nabla_y \Phi_p^{e\text{III}} & & & \bar{\mathbf{h}}_{Tq}^{m\text{III}} &= -\hat{u}_y \times \nabla_y \Phi_q^{m\text{III}} \end{aligned} \right\} \quad (4-8)$$

The objective is to relate the amplitude coefficients $\mathbf{A}^I, \mathbf{B}^I, \mathbf{A}^{\text{II}}, \mathbf{B}^{\text{II}}$, and $\mathbf{A}^{\text{III}}, \mathbf{B}^{\text{III}}$ in eqs.(4-4) to (4-6) to each other by the generalized scattering matrix of the T-junction:

$$\begin{bmatrix} \mathbf{B}^I \\ \mathbf{B}^{\text{II}} \\ \mathbf{B}^{\text{III}} \end{bmatrix} = \begin{bmatrix} \mathbf{S}_{11} & \mathbf{S}_{12} & \mathbf{S}_{13} \\ \mathbf{S}_{21} & \mathbf{S}_{22} & \mathbf{S}_{23} \\ \mathbf{S}_{31} & \mathbf{S}_{32} & \mathbf{S}_{33} \end{bmatrix} \begin{bmatrix} \mathbf{A}^I \\ \mathbf{A}^{\text{II}} \\ \mathbf{A}^{\text{III}} \end{bmatrix} \quad (4-9)$$

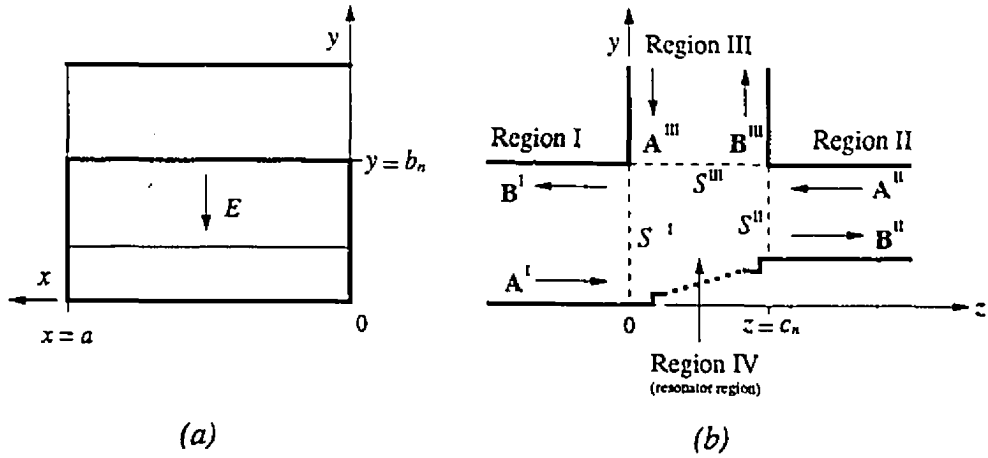


FIGURE 4.3 Discontinuity-distorted E-plane T-junction of three rectangular waveguides: (a) end view; (b) side view.

For the discontinuity-distorted resonator region IV, the electric and magnetic vector potentials are composed of three solutions corresponding to the number of apertures. These are determined by applying the principle of superposition to the non-homogeneous boundary conditions of the Helmholtz equation. That is, the solution is a sum of the three functions $\psi^{e,m(1)}$, $\psi^{e,m(2)}$, and $\phi^{e,m(3)}$ satisfying eqs.(2-3) and eq.(2-4), where solution (1) is obtained when short circuits are introduced in the boundary planes S^{II} and S^{III} , and the boundary plane S^I remains open; solutions (2) and (3) are found analogously:

$$\begin{aligned} \bar{F}^{IV} &= \hat{u}_z (\psi^{e(1)}(x, y, z) + \psi^{e(2)}(x, y, z)) + \hat{u}_y \phi^{e(3)}(x, y, z) \\ \bar{A}^{IV} &= \hat{u}_z (\psi^{m(1)}(x, y, z) + \psi^{m(2)}(x, y, z)) \pm \hat{u}_x \phi^{m(3)}(x, y, z) \end{aligned} \quad (2-18)$$

Figure 4.4 depicts regions IV(1), IV(2), and IV(3) corresponding to solutions (1), (2), and (3) with their boundary conditions. To determine these solutions $\psi^{e,m(1)}$, $\psi^{e,m(2)}$, and $\phi^{e,m(3)}$ of the Helmholtz equation, these regions IV are appropriately subdivided into two sets of subregions. The first set, applicable to IV(1) and IV(2), is a subdivision of region IV having all subregion interfaces perpendicular to the z-axis and the second set, pertaining to IV(3), having the subregion interfaces perpendicular to the y-axis. These subregions are labeled IVm1, IVm2, . . . , IVmn, and IVb1, IVb2, . . . , IVbn, respectively,

where n is the total number of subregions in each direction (cf. Figures 4.5 - 4.7).

It is essential here to note that the subregions IVm1, IVmn, and IVb1 must have the same cross-section dimensions as waveguides I, II and III, respectively. Though this requirement applies universally, it is equally important to note that there is no loss of generality because of it. Furthermore, Figure 4.4 shows no variation along the x -axis even though this formulation will accommodate such a variation. Both of these situations will be addressed in greater detail later.

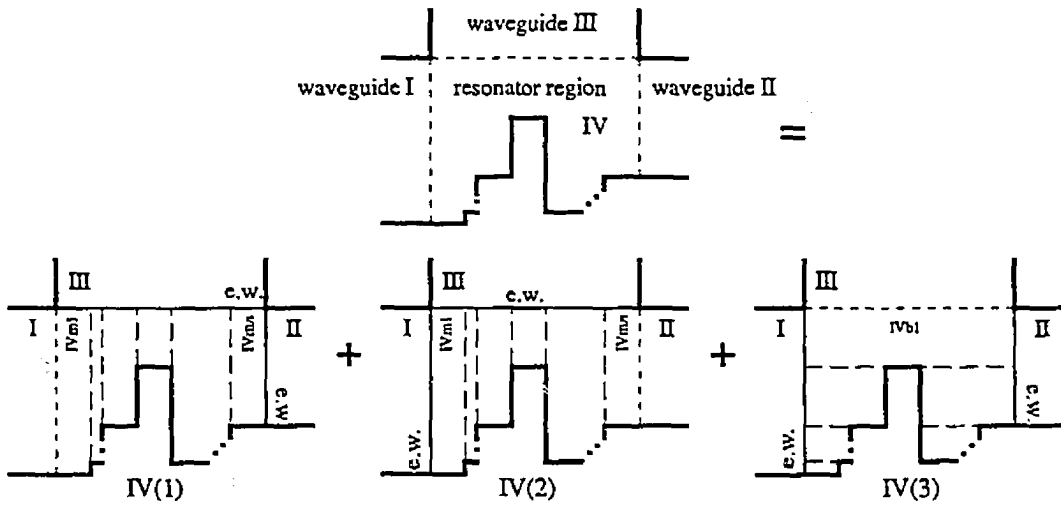


FIGURE 4.4 Superposition of the resonator region for field theory treatment.

Electric and magnetic potentials may be now assigned to solutions (1), (2) and (3) as a summation over the subregions:

$$\psi^{e(1)} = \psi^{e(2)} = \sum_{i=1}^n \psi^{eIVmi}(x, y, z) = \sum_{i=1}^n \sum_{p=1}^{n^{eIVm}} \sqrt{Z_p^{eIVmi}} \Psi_p^{eIVmi}(x, y) \zeta_p^{eIVmi}(z)$$

$$\psi^{m(1)} = \psi^{m(2)} = \sum_{i=1}^n \psi^{mIVmi}(x, y, z) = \sum_{i=1}^n \sum_{q=1}^{n^{mIVm}} \sqrt{Y_q^{mIVmi}} \Psi_q^{mIVmi}(x, y) \zeta_q^{mIVmi}(z)$$

$$\phi^{e(3)} = \sum_{i=1}^n \phi^{eIVbi}(x, y, z) = \sum_{i=1}^n \sum_{p=1}^{n^{eIVb}} \sqrt{Z_p^{eIVbi}} \Phi_p^{eIVbi}(x, z) \xi_p^{eIVbi}(y)$$

$$\phi^{m(3)} = \sum_{i=1}^n \phi^{mIVbi}(x, y, z) = \sum_{i=1}^n \sum_{q=1}^{n^{mIVb}} \sqrt{Y_q^{mIVbi}} \Phi_q^{mIVbi}(x, z) \xi_q^{mIVbi}(y) \quad (4-10)$$

where the functions $\zeta_{p,q}^{e,m}(z)$ and $\xi_{p,q}^{e,m}(y)$ contain the unknown amplitudes of the traveling waves according to eq.(2-4), and the cross-section functions $\Psi^{e,m}$ and $\Phi^{e,m}$ are determined by eq.(2-3). Again, the indices p and q represent double-indexed modal eigenfunctions in each subregion ordered in increasing cut-off frequencies. Formulating the electromagnetic fields from these vector potentials to facilitate matching at the interfaces between waveguides I to III, and the resonator region IV, requires determining the scattering matrix between each subregion. This will reduce the number of unknown wave amplitude vectors in the discontinuity-distorted resonator region to three. After defining the required internal scattering matrices for solutions (1), (2) and (3), the overall matching conditions are applied.

Starting with solution (1), where region IV(1) is detailed in Figure 4.5, the tangential electromagnetic fields in each region IVmi are written

$$\begin{aligned} \bar{\mathbf{E}}_T^{IVmi} &= [\bar{\mathbf{e}}_T^{eIVmi} \mid \bar{\mathbf{e}}_T^{mIVmi}] \cdot \text{diag}(\sqrt{Z_{p,q}^{e,mIVmi}}) \cdot \\ &\quad \left[\text{diag}(\exp[-jk_{z,p,q}^{e,mIVmi}(z - c_{j-1})]) \cdot \mathbf{A}^{IV(1)i} + \text{diag}(\exp[jk_{z,p,q}^{e,mIVmi}(z - c_{j-1})]) \cdot \mathbf{B}^{IV(1)i} \right] \\ \bar{\mathbf{H}}_T^{IVmi} &= [\bar{\mathbf{h}}_T^{eIVmi} \mid \bar{\mathbf{h}}_T^{mIVmi}] \cdot \text{diag}(\sqrt{Y_{p,q}^{e,mIVmi}}) \cdot \\ &\quad \left[\text{diag}(\exp[-jk_{z,p,q}^{e,mIVmi}(z - c_{j-1})]) \cdot \mathbf{A}^{IV(1)i} - \text{diag}(\exp[jk_{z,p,q}^{e,mIVmi}(z - c_{j-1})]) \cdot \mathbf{B}^{IV(1)i} \right] \end{aligned} \quad (4-11)$$

where elements of the mode functions are

$$\begin{aligned} \bar{e}_{Tp}^{eIVmi} &= \hat{u}_z \times \nabla_z \Psi_p^{eIVbi} & \bar{e}_{Tq}^{mIVmi} &= -\nabla_z \Psi_q^{mIVmi} \\ \bar{h}_{Tp}^{eIVmi} &= -\nabla_z \Psi_p^{eIVbi} & \bar{h}_{Tq}^{mIVmi} &= -\hat{u}_z \times \nabla_z \Psi_q^{mIVmi} \end{aligned} \quad (4-12)$$

The tangential electric and magnetic fields are matched at the common interfaces $z = c_j$ for $j=1,2,3,\dots,n-1$ between the subregions to yield the scattering matrix at each interface

$$\begin{bmatrix} \mathbf{B}^{(1)i} \\ \mathbf{A}^{(1)i+1} \end{bmatrix} = \begin{bmatrix} \mathbf{S}_{11}^{(1)i} & \mathbf{S}_{12}^{(1)i} \\ \mathbf{S}_{21}^{(1)i} & \mathbf{S}_{22}^{(1)i} \end{bmatrix} \begin{bmatrix} \mathbf{A}^{(1)i} \\ \mathbf{B}^{(1)i+1} \end{bmatrix} \text{ at } z = c_j. \quad (4-13)$$

These scattering matrices are cascaded, along with the homogeneous empty waveguide sections between them, by the Generalized S-matrix Method found in Appendix A to yield a scattering matrix from any z -coordinate plane to another in region IV(1). For example, from discontinuity $i \rightarrow j$ or from coordinates, $z = c_i \rightarrow z = c_j$

$$\begin{bmatrix} \mathbf{B}^{(1)i}(z = c_i) \\ \mathbf{A}^{(1)j}(z = c_j) \end{bmatrix} = \begin{bmatrix} \mathbf{S}_{11i \rightarrow j}^{IVm} & \mathbf{S}_{12i \rightarrow j}^{IVm} \\ \mathbf{S}_{21i \rightarrow j}^{IVm} & \mathbf{S}_{22i \rightarrow j}^{IVm} \end{bmatrix} \begin{bmatrix} \mathbf{A}^{(1)i}(z = c_i) \\ \mathbf{B}^{(1)j}(z = c_j) \end{bmatrix} \quad (4-14)$$

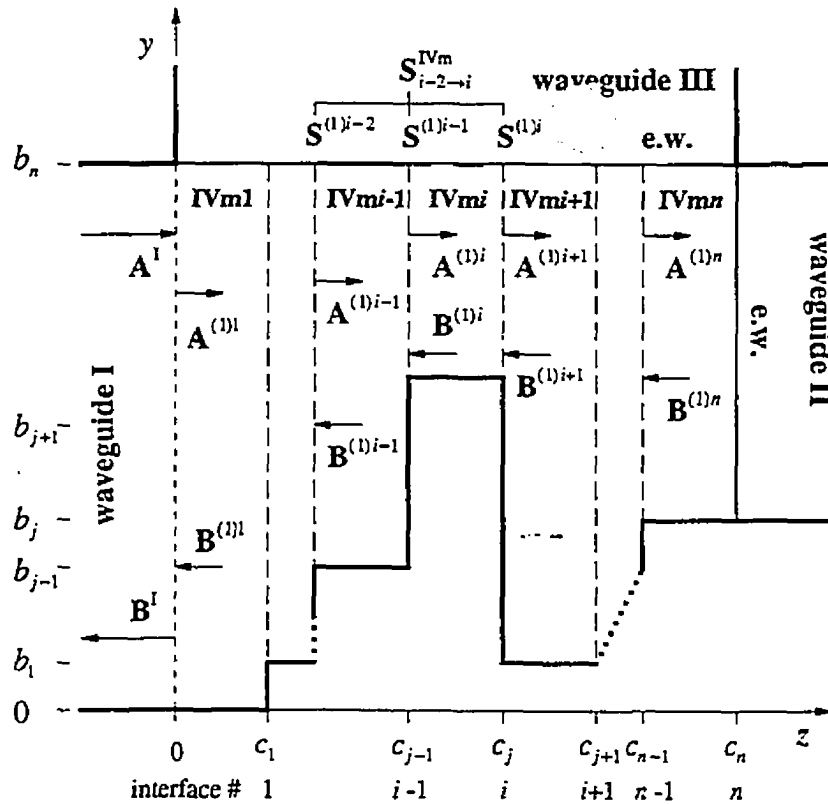


FIGURE 4.5 Detailed description of the subregions corresponding to solution (1).

Now, with a short circuit at $z = c_n$ according to the construction of solution (1) the following relation holds

$$\mathbf{B}^{(1)n} = -\mathbf{A}^{(1)n} \} \text{ at } z = c_n \quad (4-15)$$

and a reflection coefficient may be defined at each interface $z = c_j$ for $j = 1, 2, 3, \dots, n-1$ by

$$\mathbf{B}^{(1)i} = \Gamma_{i-1}^{(1)} \mathbf{A}^{(1)i} = \left[\mathbf{S}_{11i-1 \rightarrow n}^{IVm} - \mathbf{S}_{12i-1 \rightarrow n}^{IVm} (\mathbf{I} + \mathbf{S}_{22i-1 \rightarrow n}^{IVm})^{-1} \mathbf{S}_{21i-1 \rightarrow n}^{IVm} \right] \mathbf{A}^{(1)i} \quad (4-16)$$

Using this modal reflection coefficient and introducing transfer matrices, $\mathbf{T}_{Ai-1}^{(1)}$ and $\mathbf{T}_{Bi-1}^{(1)}$, the amplitudes of the traveling waves in each subregion may be expressed in terms of the amplitude of the forward traveling wave in subregion IVm1. That is, the wave amplitudes $\mathbf{A}^{(1)i}$ and $\mathbf{B}^{(1)i}$ in the i th region are related to the wave amplitude $\mathbf{A}^{(1)1}$ in region IVm1 by

$$\mathbf{A}^{(1)i} = \underbrace{(\mathbf{I} - \mathbf{S}_{220 \rightarrow i-1}^{IVm} \Gamma_{i-1}^{(1)}) \mathbf{S}_{210 \rightarrow i-1}^{IVm}}_{\mathbf{T}_{Ai-1}^{(1)}} \mathbf{A}^{(1)1} \quad (4-17)$$

and

$$\mathbf{B}^{(1)i} = \Gamma_{i-1}^{(1)} \mathbf{A}^{(1)i} = \underbrace{\Gamma_{i-1}^{(1)} \mathbf{T}_{Ai-1}^{(1)}}_{\mathbf{T}_{Bi-1}^{(1)}} \mathbf{A}^{(1)1} \quad (4-18)$$

Notice, as expected, the transfer matrices at $z = 0$ are

$$\mathbf{T}_{A0}^{(1)} = \mathbf{I} \quad \text{and} \quad \mathbf{T}_{B0}^{(1)} = \Gamma_0^{(1)} = \Gamma^I \quad \dots \quad (4-19)$$

where the latter is the reflection coefficient at waveguide I with ports 2 and 3 short circuited. From eqs.(4-17) and (4-18), electromagnetic fields according to solution (1) may be written in terms of the single amplitude coefficient $\mathbf{A}^{(1)1}$ [cf. eq.(4-10)]. The presentation of these field expressions will be made in conjunction with solutions (2) and (3) once they are completed.

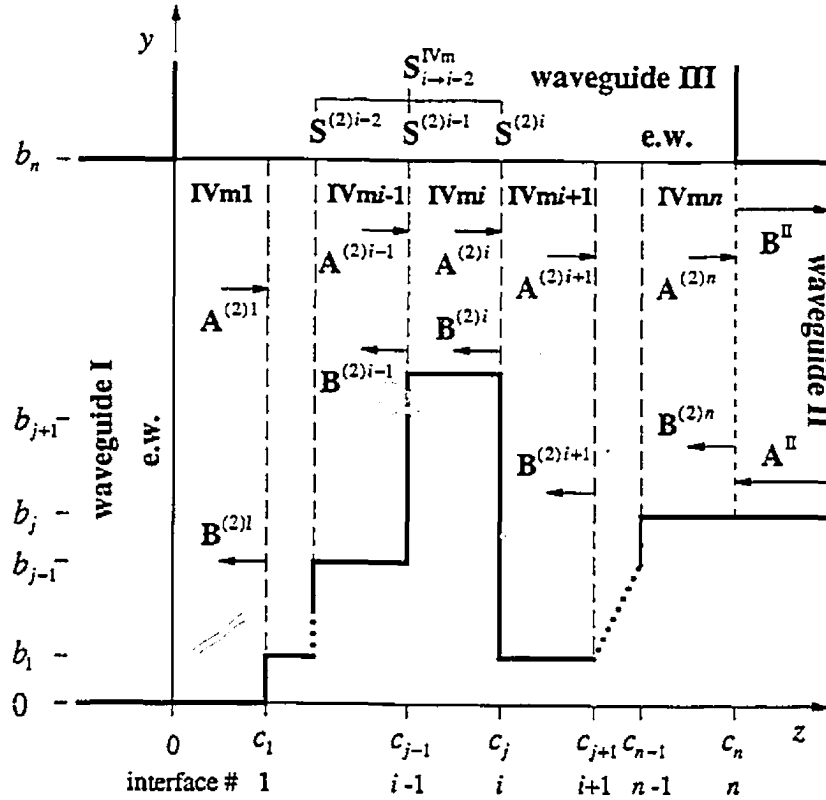


FIGURE 4.6 Detailed description of the subregions corresponding to solution (2).

Following upon this, and because the subdivision for solutions (1) and (2) are identical, the scattering matrices calculated at each interface $z=c_j$ for $j=1,2,3,\dots,n-1$ in solution (1) may be applied to solution (2) by switching the appropriate submatrices. The scattering matrix between subregions $IVmi+1$ and $IVmi$ as seen in Figure 4.6 is

$$\begin{bmatrix} \mathbf{A}^{(2)i+1} \\ \mathbf{B}^{(2)i} \end{bmatrix} = \begin{bmatrix} \mathbf{S}_{22}^{(1)i} & \mathbf{S}_{21}^{(1)i} \\ \mathbf{S}_{21}^{(1)i} & \mathbf{S}_{11}^{(1)i} \end{bmatrix} \begin{bmatrix} \mathbf{B}^{(2)i+1} \\ \mathbf{A}^{(2)i} \end{bmatrix} = \begin{bmatrix} \mathbf{S}_{11}^{(2)i} & \mathbf{S}_{12}^{(2)i} \\ \mathbf{S}_{21}^{(2)i} & \mathbf{S}_{22}^{(2)i} \end{bmatrix} \begin{bmatrix} \mathbf{B}^{(2)i+1} \\ \mathbf{A}^{(2)i} \end{bmatrix} \quad \text{at } z=c_j \quad (4-20)$$

Hence, the scattering matrix can be determined between any two z -coordinate planes within region $IV(2)$. For example, the scattering matrix between $z=c_j$ and $z=c_i$ is

$$\begin{bmatrix} \mathbf{A}^{(2)j}(z=c_j) \\ \mathbf{B}^{(2)i}(z=c_i) \end{bmatrix} = \begin{bmatrix} \mathbf{S}_{11j \rightarrow i}^{\text{IVm}} & \mathbf{S}_{12j \rightarrow i}^{\text{IVm}} \\ \mathbf{S}_{21j \rightarrow i}^{\text{IVm}} & \mathbf{S}_{22j \rightarrow i}^{\text{IVm}} \end{bmatrix} \begin{bmatrix} \mathbf{B}^{(2)j}(z=c_j) \\ \mathbf{A}^{(2)i}(z=c_i) \end{bmatrix} \quad (4-21)$$

Applying the boundary condition at $z = 0$ for solution (2), a modal reflection coefficient and the transfer matrices may once again be defined at the interfaces

$$\mathbf{A}^{(2)i} = \Gamma_i^{(2)} \mathbf{B}^{(2)i} = \left[\mathbf{S}_{11i \rightarrow 0}^{\text{IVm}} - \mathbf{S}_{12i \rightarrow 0}^{\text{IVm}} (\mathbf{I} + \mathbf{S}_{22i \rightarrow 0}^{\text{IVm}})^{-1} \mathbf{S}_{21i \rightarrow 0}^{\text{IVm}} \right] \mathbf{B}^{(2)i} \quad (4-22)$$

and

$$\begin{aligned} \mathbf{B}^{(2)i} &= (\mathbf{I} - \mathbf{S}_{22i \rightarrow 0}^{\text{IVm}} \Gamma_i^{(2)}) \mathbf{S}_{21i \rightarrow 0}^{\text{IVm}} \mathbf{B}^{(2)n} = \mathbf{T}_{\text{Bi}}^{(2)} \mathbf{B}^{(2)n} \\ \mathbf{A}^{(2)i} &= \Gamma_{i-1}^{(2)} \mathbf{B}^{(2)i} = \Gamma_{i-1}^{(2)} \mathbf{T}_{\text{Bi}-1}^{(2)} \mathbf{B}^{(2)n} = \mathbf{T}_{\text{Ai}-1}^{(2)} \mathbf{B}^{(2)n} \end{aligned} \quad (4-23)$$

As anticipated, the transfer matrices in region IVm*n* at $z = c_n$ are

$$\mathbf{T}_{\text{Bn}}^{(2)} = \mathbf{I} \quad \text{and} \quad \mathbf{T}_{\text{An}}^{(2)} = \Gamma_n^{(2)} = \Gamma^n. \quad (4-24)$$

Now, all the amplitude coefficients for solution (2) can be expressed in a single unknown amplitude coefficient $\mathbf{B}^{(2)n}$ in region IVm*n*.

Finally, for solution (3), the region IV(3) is subdivided according to Figure 4.7, and the tangential fields for each subregion are written as

$$\begin{aligned} \vec{\mathbf{E}}_T^{\text{IVbi}} &= [\vec{\mathbf{e}}_T^{\text{eIVbi}} \mid \vec{\mathbf{e}}_T^{\text{mIVbi}}] \cdot \text{diag}(\sqrt{Z_{p,q}^{\text{e,mIVbi}}}) \cdot \\ &\quad \left[\text{diag}(\exp[-jk_{yp,q}^{\text{e,mIVbi}}(y-b_{n-i+1})]) \mathbf{B}^{(3)i} + \text{diag}(\exp[jk_{yp,q}^{\text{e,mIVbi}}(y-b_{n-i+1})]) \mathbf{A}^{(3)i} \right] \\ \vec{\mathbf{H}}_T^{\text{IVbi}} &= [\vec{\mathbf{h}}_T^{\text{eIVbi}} \mid \vec{\mathbf{h}}_T^{\text{mIVbi}}] \cdot \text{diag}(\sqrt{Y_{p,q}^{\text{e,mIVbi}}}) \cdot \\ &\quad \left[\text{diag}(\exp[-jk_{yp,q}^{\text{e,mIVbi}}(y-b_{n-i+1})]) \mathbf{B}^{(3)i} - \text{diag}(\exp[jk_{yp,q}^{\text{e,mIVbi}}(y-b_{n-i+1})]) \mathbf{A}^{(3)i} \right] \end{aligned} \quad (4-25)$$

where the elements of the mode functions are

$$\begin{aligned} \vec{e}_{Tp}^{\text{eIVbi}} &= \hat{u}_y \times \nabla_y \Phi_p^{\text{eIVbi}} & \vec{e}_{Tq}^{\text{mIVbi}} &= -\nabla_y \Phi_q^{\text{mIVbi}} \\ \vec{h}_{Tp}^{\text{eIVbi}} &= -\nabla_y \Phi_p^{\text{eIVbi}} & \vec{h}_{Tq}^{\text{mIVbi}} &= -\hat{u}_y \times \nabla_y \Phi_q^{\text{mIVbi}} \end{aligned} \quad (4-26)$$

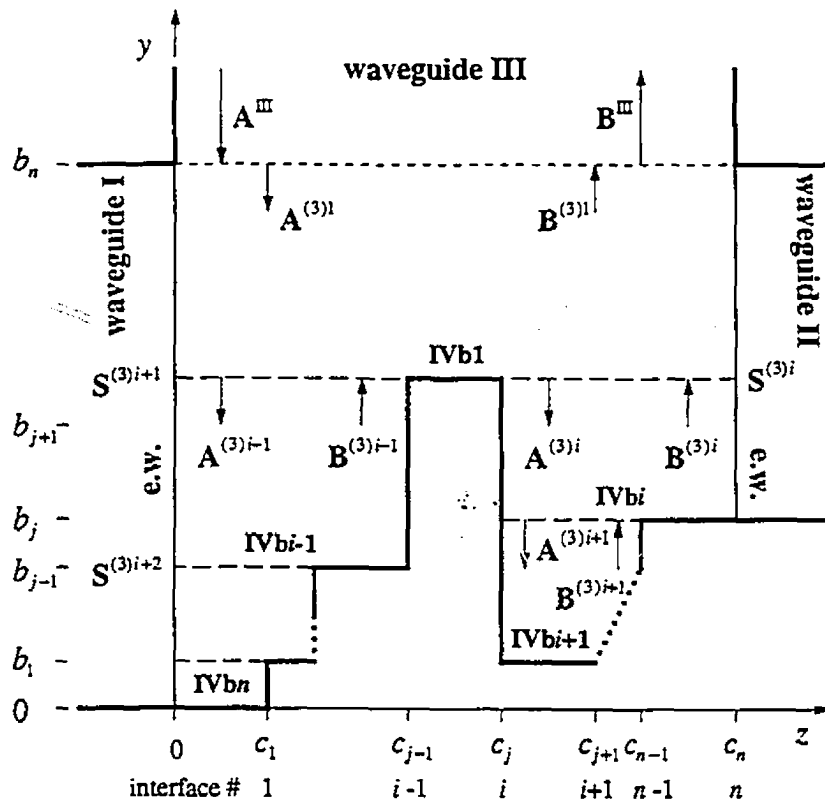


FIGURE 4.7 Detailed description of the subregions corresponding to solution (3).

Again, the fields are matched at the common interfaces to yield the scattering matrices. For example, the scattering matrix between region IVbi and IVbi+1 is

$$\begin{bmatrix} \mathbf{B}^{(3)i} \\ \mathbf{A}^{(3)i+1} \end{bmatrix} = \begin{bmatrix} \mathbf{S}_{11}^{(3)i} & \mathbf{S}_{12}^{(3)i} \\ \mathbf{S}_{21}^{(3)i} & \mathbf{S}_{22}^{(3)i} \end{bmatrix} \begin{bmatrix} \mathbf{A}^{(3)i} \\ \mathbf{B}^{(3)i+1} \end{bmatrix} \text{ at } y = b_{n-i} \quad (4-27)$$

Once the scattering matrices at each interface are found, an overall scattering matrix between any two y-coordinate planes in region IV(3) may be calculated. Between the $y = b_i$ and $y = b_j$ planes, the scattering matrix is

$$\begin{bmatrix} \mathbf{B}^{(3)i}(y = b_i) \\ \mathbf{A}^{(3)j}(y = b_j) \end{bmatrix} = \begin{bmatrix} \mathbf{S}_{11i \rightarrow j}^{IVb} & \mathbf{S}_{12i \rightarrow j}^{IVb} \\ \mathbf{S}_{21i \rightarrow j}^{IVb} & \mathbf{S}_{22i \rightarrow j}^{IVb} \end{bmatrix} \begin{bmatrix} \mathbf{A}^{(3)i}(y = b_i) \\ \mathbf{B}^{(3)j}(y = b_j) \end{bmatrix} \quad (4-28)$$

Since the boundary condition at $y = 0$ requires that

$$\mathbf{B}^{(3)n} = -\mathbf{A}^{(3)n} \} \text{ at } y = 0$$

a reflection coefficient and the transfer matrices, similar to those of solutions (1) and (2), may be defined for each subregion interface as

$$\mathbf{B}^{(3)i} = \Gamma_{n-i+1}^{(3)} \mathbf{A}^{(3)i} = \left[\mathbf{S}_{11n-i+1 \rightarrow 0}^{IVb} - \mathbf{S}_{12n-i+1 \rightarrow 0}^{IVb} (\mathbf{I} + \mathbf{S}_{22n-i+1 \rightarrow 0}^{IVb})^{-1} \mathbf{S}_{21n-i+1 \rightarrow 0}^{IVb} \right] \mathbf{A}^{(3)i} \quad (4-29)$$

and

$$\begin{aligned} \mathbf{A}^{(3)i} &= (\mathbf{I} - \mathbf{S}_{22n \rightarrow n-i+1}^{IVb} \Gamma_{n-i+1}^{(3)})^{-1} \mathbf{S}_{21n \rightarrow n-i+1}^{IVb} \mathbf{A}^{(3)1} = \mathbf{T}_{An-i+1}^{(3)} \mathbf{A}^{(3)1} \\ \mathbf{B}^{(3)i} &= \Gamma_{n-i+1}^{(3)} \mathbf{A}^{(3)i} = \Gamma_{n-i+1}^{(3)} \mathbf{T}_{An-i+1}^{(3)} \mathbf{A}^{(3)1} = \mathbf{T}_{Bn-i+1}^{(3)} \mathbf{A}^{(3)1} \end{aligned} \quad (4-30)$$

Hence, all the amplitude coefficients in region IV(3) may now be expressed in terms of the single unknown coefficient $\mathbf{A}^{(3)1}$. Again, the transfer matrices in region IVb1 are

$$\mathbf{T}_{A1}^{(3)} = \mathbf{I} \quad \text{and} \quad \mathbf{T}_{B1}^{(3)} = \Gamma_1^{(3)} = \Gamma^{\text{III}} \quad (4-31)$$

where Γ^{III} is the reflection coefficient at port 3 with ports 1 and 2 shorted.

In summary, all the fields within the resonator region for solutions (1), (2), and (3) can now be expressed in terms of three still unknown coefficients in the subregions adjacent to waveguides I, II and III. To illustrate, the complete electric field within the resonator region according to eq.(2-18) and (4-10) is written as

$$\bar{\mathbf{E}}^{IV}(x, y, z) = \sum_{i=1}^n (\bar{\mathbf{E}}^{(1)i} + \bar{\mathbf{E}}^{(2)i} + \bar{\mathbf{E}}^{(3)i}) \quad (4-32)$$

where

$$\begin{aligned} \bar{\mathbf{E}}^{(1)i} &= \left\{ \left[\bar{\mathbf{e}}_T^{eIVmi} \mid \bar{\mathbf{e}}_T^{mIVmi} + e_z^{mIVmi} \hat{u}_z \right] \text{diag} \left(\sqrt{Z_{p,q}^{e,mIVmi}} \exp[-jk_{z,p,q}^{e,mIVmi} (z - c_{i-1})] \right) \mathbf{T}_{Ai-1}^{(1)} \right. \\ &\quad \left. + \left[\bar{\mathbf{e}}_T^{eIVmi} \mid \bar{\mathbf{e}}_T^{mIVmi} - e_z^{mIVmi} \hat{u}_z \right] \text{diag} \left(\sqrt{Z_{p,q}^{e,mIVmi}} \exp[jk_{z,p,q}^{e,mIVmi} (z - c_{i-1})] \right) \mathbf{T}_{Bi-1}^{(1)} \right\} \mathbf{A}^{(1)i} \end{aligned}$$

$$\begin{aligned}
\bar{\mathbf{E}}^{(2)i} &= \left\{ \left[\bar{\mathbf{e}}_T^{mIVmi} \mid \bar{\mathbf{e}}_T^{mIVmi} + e_z^{mIVmi} \hat{u}_z \right] \text{diag} \left(\sqrt{Z_{p,q}^{e,mIVmi}} \exp \left[-jk_{z,p,q}^{e,mIVmi} (z - c_i) \right] \right) \mathbf{T}_{\Lambda_i}^{(2)} \right. \\
&\quad \left. + \left[\bar{\mathbf{e}}_T^{mIVmi} \mid \bar{\mathbf{e}}_T^{mIVmi} - e_z^{mIVmi} \hat{u}_z \right] \text{diag} \left(\sqrt{Z_{p,q}^{e,mIVmi}} \exp \left[jk_{z,p,q}^{e,mIVmi} (z - c_i) \right] \right) \mathbf{T}_{\mathbf{B}_i}^{(2)} \right\} \mathbf{B}^{(2)n} \\
\bar{\mathbf{E}}^{(3)i} &= \left\{ \left[\bar{\mathbf{e}}_T^{mIVbi} \mid \bar{\mathbf{e}}_T^{mIVbi} + e_y^{mIVbi} \hat{u}_y \right] \text{diag} \left(\sqrt{Z_{p,q}^{e,mIVbi}} \exp \left[-jk_{y,p,q}^{e,mIVbi} (y - b_{n-i+1}) \right] \right) \cdot \mathbf{T}_{\mathbf{B}_{n-i+1}}^{(3)} \right. \\
&\quad \left. + \left[\bar{\mathbf{e}}_T^{mIVbi} \mid \bar{\mathbf{e}}_T^{mIVbi} - e_y^{mIVbi} \hat{u}_y \right] \text{diag} \left(\sqrt{Z_{p,q}^{e,mIVbi}} \exp \left[jk_{y,p,q}^{e,mIVbi} (y - b_{n-i+1}) \right] \right) \cdot \mathbf{T}_{\mathbf{A}_{n-i+1}}^{(3)} \right\} \mathbf{A}^{(3)l} \quad (4-33)
\end{aligned}$$

The transverse components of the mode functions are given in eqs.(4-12) and (4-26) and the longitudinal components are

$$e_{zq}^{mIVmi} = \frac{(k_c^2)_q^{mIVmi}}{jk_{zq}^{mIVmi}} \Psi_q^{mIVmi} \quad \text{and} \quad e_{yq}^{mIVbi} = \frac{(k_c^2)_q^{mIVbi}}{jk_{yq}^{mIVbi}} \Phi_q^{mIVbi}. \quad (4-34)$$

It is now possible using eqs.(4-33) to match the electric tangential fields at the interfaces $z = 0, c_n$ and $y = b_n$ between waveguides I, II, and III and the discontinuity-distorted resonator region IV. Expressions for the magnetic fields will be presented and matched subsequent to completing the electric field.

The field continuity condition at $z = 0$ for the tangential electric field is

$$\left. \begin{aligned}
\bar{\mathbf{E}}_{x,y}^I &= \bar{\mathbf{E}}_{x,y}^{IV} = \sum_{i=1}^n \left(\bar{\mathbf{E}}_{x,y}^{(1)i} + \bar{\mathbf{E}}_{x,y}^{(2)i} + \bar{\mathbf{E}}_{x,y}^{(3)i} \right) \\
&= \bar{\mathbf{E}}_{x,y}^{(1)l}
\end{aligned} \right\} \text{at } z = 0. \quad (4-35)$$

It is important to observe that, as a consequence of the choice of solutions (1), (2) and (3), only one single term remains in the summation over the subregions. The value of the electric field is zero at $z = 0$ for the regions corresponding to solutions (2) and (3). Applying the matching equation for the electric fields in eqs.(4-4) and (4-33), as well as orthogonality, and integrating over S^I yields the following relationship between the amplitude coefficients in waveguide I and the resonator region:

$$\mathbf{A}^{(1)l} = (\mathbf{I} + \mathbf{\Gamma}^I)^{-1} (\mathbf{A}^I + \mathbf{B}^I). \quad (4-36)$$

Similarly, equating the electric fields at $z = c_n$ and $y = b_n$

$$\bar{\mathbf{E}}_{x,y}^{\text{II}} = \bar{\mathbf{E}}_{x,y}^{(2)n} \quad \text{and} \quad \bar{\mathbf{E}}_{x,z}^{\text{III}} = \bar{\mathbf{E}}_{x,z}^{(3)l} \quad (4-37)$$

the resulting relations are

$$\begin{aligned} \mathbf{B}^{(2)n} &= (\mathbf{I} + \Gamma^{\text{II}})^{-1} (\mathbf{A}^{\text{II}} + \mathbf{B}^{\text{II}}) \\ \mathbf{B}^{(3)l} &= (\mathbf{I} + \Gamma^{\text{III}})^{-1} (\mathbf{A}^{\text{III}} + \mathbf{B}^{\text{III}}) \end{aligned} \quad (4-38)$$

Using eq.(4-36) and eqs.(4-38) the magnetic fields in the resonator region may be completely expressed in terms of the amplitude coefficients in waveguides I, II, and III:

$$\bar{\mathbf{H}}^{\text{IV}}(x, y, z) = \sum_{i=1}^n (\bar{\mathbf{H}}^{(1)i} + \bar{\mathbf{H}}^{(2)i} + \bar{\mathbf{H}}^{(3)i}) \quad (4-39)$$

where

$$\begin{aligned} \bar{\mathbf{H}}^{(1)i} &= \left\{ \left[\bar{\mathbf{h}}_T^{e\text{IVmi}} + h_z^{e\text{IVmi}} \hat{u}_z \mid \bar{\mathbf{h}}_T^{m\text{IVmi}} \right] \text{diag} \left(\sqrt{Y_{p,q}^{e,m\text{IVmi}}} \exp \left[-jk_{z,p,q}^{e,m\text{IVmi}} (z - c_{i-1}) \right] \right) \mathbf{T}_{\Lambda_{i-1}}^{(1)} \right. \\ &\quad \left. - \left[\bar{\mathbf{h}}_T^{e\text{IVmi}} - h_z^{e\text{IVmi}} \hat{u}_z \mid \bar{\mathbf{h}}_T^{m\text{IVmi}} \right] \text{diag} \left(\sqrt{Y_{p,q}^{e,m\text{IVmi}}} \exp \left[jk_{z,p,q}^{e,m\text{IVmi}} (z - c_{i-1}) \right] \right) \mathbf{T}_{\Lambda_{i-1}}^{(1)} \right\} \mathbf{M}^{\text{I}} (\mathbf{A}^{\text{I}} + \mathbf{B}^{\text{I}}) \\ \bar{\mathbf{H}}^{(2)i} &= \left\{ \left[\bar{\mathbf{h}}_T^{e\text{IVmi}} + h_z^{e\text{IVmi}} \hat{u}_z \mid \bar{\mathbf{h}}_T^{m\text{IVmi}} \right] \text{diag} \left(\sqrt{Y_{p,q}^{e,m\text{IVmi}}} \exp \left[-jk_{z,p,q}^{e,m\text{IVmi}} (z - c_i) \right] \right) \mathbf{T}_{\Lambda_i}^{(2)} \right. \\ &\quad \left. - \left[\bar{\mathbf{h}}_T^{e\text{IVmi}} - h_z^{e\text{IVmi}} \hat{u}_z \mid \bar{\mathbf{h}}_T^{m\text{IVmi}} \right] \text{diag} \left(\sqrt{Y_{p,q}^{e,m\text{IVmi}}} \exp \left[jk_{z,p,q}^{e,m\text{IVmi}} (z - c_i) \right] \right) \mathbf{T}_{\Lambda_i}^{(2)} \right\} \mathbf{M}^{\text{II}} (\mathbf{A}^{\text{II}} + \mathbf{B}^{\text{II}}) \\ \bar{\mathbf{H}}^{(3)i} &= \left\{ \left[\bar{\mathbf{h}}_T^{e\text{IVbi}} + h_y^{e\text{IVbi}} \hat{u}_y \mid \bar{\mathbf{h}}_T^{m\text{IVbi}} \right] \text{diag} \left(\sqrt{Y_{p,q}^{e,m\text{IVbi}}} \exp \left[-jk_{y,p,q}^{e,m\text{IVbi}} (y - b_j) \right] \right) \cdot \mathbf{T}_{\Lambda_j}^{(3)} \right. \\ &\quad \left. - \left[\bar{\mathbf{h}}_T^{e\text{IVbi}} - h_y^{e\text{IVbi}} \hat{u}_y \mid \bar{\mathbf{h}}_T^{m\text{IVbi}} \right] \text{diag} \left(\sqrt{Y_{p,q}^{e,m\text{IVbi}}} \exp \left[jk_{y,p,q}^{e,m\text{IVbi}} (y - b_j) \right] \right) \cdot \mathbf{T}_{\Lambda_j}^{(3)} \right\} \mathbf{M}^{\text{III}} (\mathbf{A}^{\text{III}} + \mathbf{B}^{\text{III}}) \end{aligned} \quad (4-40)$$

and where

$$\mathbf{M}^{\text{I}} = (\mathbf{I} - \Gamma^{\text{I}})^{-1}, \quad \mathbf{M}^{\text{II}} = (\mathbf{I} - \Gamma^{\text{II}})^{-1}, \quad \mathbf{M}^{\text{III}} = (\mathbf{I} - \Gamma^{\text{III}})^{-1}, \quad (4-41)$$

and the longitudinal components of the mode functions are

$$h_{zp}^{eIVmi} = \frac{(k_c^2)^{eIVmi}}{jk_p^{eIVmi}} \Psi_p^{eIVmi} \quad \text{and} \quad h_{yp}^{eIVbi} = \frac{(k_c^2)^{eIVbi}}{jk_{yp}^{eIVbi}} \Psi_p^{eIVbi}. \quad (4-42)$$

The transverse components of the mode functions are given in eqs.(4-12) and (4-26).

Matching the magnetic fields at the interfaces between waveguides I, II and III with the discontinuity-distorted resonator region IV relates the amplitude coefficients to yield the desired modal scattering matrix of the T-junction. The continuity equations at $z = 0, c_n$ and $y = b_n$ for the tangential magnetic fields are

$$\left. \begin{aligned} \bar{\mathbf{H}}_{x,y}^I &= \bar{\mathbf{H}}_{x,y}^{IV} = \sum_{i=1}^n \left(\bar{\mathbf{H}}_{x,y}^{(1)i} + \bar{\mathbf{H}}_{x,y}^{(2)i} + \bar{\mathbf{H}}_{x,y}^{(3)i} \right) \\ &= \bar{\mathbf{H}}_{x,y}^{(1)l} + \bar{\mathbf{H}}_{x,y}^{(2)l} + \sum_{i=1}^n \bar{\mathbf{H}}_{x,y}^{(3)i} \end{aligned} \right\} \text{at } z = 0 \quad (4-43)$$

$$\bar{\mathbf{H}}_{x,y}^{II} = \bar{\mathbf{H}}_{x,y}^{(1)n} + \bar{\mathbf{H}}_{x,y}^{(2)n} + \sum_{i=1}^n \bar{\mathbf{H}}_{x,y}^{(3)i} \left\} \text{at } z = c_n \quad (4-44)$$

and

$$\bar{\mathbf{H}}_{x,z}^{III} = \sum_{i=1}^n \bar{\mathbf{H}}_{x,z}^{(1)i} + \sum_{i=1}^n \bar{\mathbf{H}}_{x,z}^{(2)i} + \bar{\mathbf{H}}_{x,z}^{(3)l} \left\} \text{at } y = b_n \quad (4-45)$$

which, when integrated over S^I , S^{II} , and S^{III} respectively, and employing the principles of orthogonality, result in the matrix equation

$$\left[\begin{array}{c|c|c} -\mathbf{I} - (\mathbf{I} - \Gamma^I) \mathbf{M}^I & -(\mathbf{U}_A^{(2)} \mathbf{T}_{\Lambda 0}^{(2)} - \mathbf{U}_B^{(2)} \mathbf{T}_{B 0}^{(2)}) \mathbf{M}^{II} & -\mathbf{V}^{I-(3)} \mathbf{M}^{III} \\ \hline -(\mathbf{U}_A^{(1)} \mathbf{T}_{\Lambda n-1}^{(1)} - \mathbf{U}_B^{(1)} \mathbf{T}_{B n-1}^{(1)}) \mathbf{M}^I & \mathbf{I} + (\mathbf{I} - \Gamma^{II}) \mathbf{M}^{II} & -\mathbf{V}^{II-(2)} \mathbf{M}^{III} \\ \hline -\mathbf{V}^{III-(1)} \mathbf{M}^I & -\mathbf{V}^{III-(2)} \mathbf{M}^{II} & \mathbf{I} + (\mathbf{I} - \Gamma^{III}) \mathbf{M}^{III} \end{array} \right] \begin{bmatrix} \mathbf{B}^I \\ \mathbf{B}^{II} \\ \mathbf{B}^{III} \end{bmatrix} = \left[\begin{array}{c|c|c} -\mathbf{I} + (\mathbf{I} - \Gamma^I) \mathbf{M}^I & +(\mathbf{U}_A^{(2)} \mathbf{T}_{\Lambda 0}^{(2)} - \mathbf{U}_B^{(2)} \mathbf{T}_{B 0}^{(2)}) \mathbf{M}^{II} & \mathbf{V}^{I-(3)} \mathbf{M}^{III} \\ \hline +(\mathbf{U}_A^{(1)} \mathbf{T}_{\Lambda n-1}^{(1)} - \mathbf{U}_B^{(1)} \mathbf{T}_{B n-1}^{(1)}) \mathbf{M}^I & \mathbf{I} - (\mathbf{I} - \Gamma^{II}) \mathbf{M}^{II} & \mathbf{V}^{II-(2)} \mathbf{M}^{III} \\ \hline \mathbf{V}^{III-(1)} \mathbf{M}^I & \mathbf{V}^{III-(2)} \mathbf{M}^{II} & \mathbf{I} - (\mathbf{I} - \Gamma^{III}) \mathbf{M}^{III} \end{array} \right] \begin{bmatrix} \mathbf{A}^I \\ \mathbf{A}^{II} \\ \mathbf{A}^{III} \end{bmatrix} \quad (4-46)$$

where

$$\begin{aligned}
\mathbf{U}_A^{(1)} &= \text{diag}\left(\exp\left[-jk_{z,p,q}^{e,mIVmn}(c_n - c_{n-1})\right]\right) \\
\mathbf{U}_B^{(1)} &= \text{diag}\left(\exp\left[+jk_{z,p,q}^{e,mIVmn}(c_n - c_{n-1})\right]\right) \\
\mathbf{U}_A^{(2)} &= \text{diag}\left(\exp\left[+jk_{z,p,q}^{e,mIVm1}c_1\right]\right) \\
\mathbf{U}_B^{(2)} &= \text{diag}\left(\exp\left[-jk_{z,p,q}^{e,mIVm1}c_1\right]\right)
\end{aligned} \tag{4-47}$$

The matrices \mathbf{V} in eq.(4-46) contain the coupling matrices for the T-junction and are of the form

$$\begin{aligned}
\mathbf{V}^{I-(3)} &= \sum_{i=1}^n \left(+\mathbf{K}^{I-(3)i} \mathbf{T}_{Bn-i+1}^{(3)} - \mathbf{K}^{I-(3)i} \mathbf{T}_{An-i+1}^{(3)} \right) \\
\mathbf{V}^{II-(3)} &= \sum_{i=1}^n \left(+\mathbf{K}^{II-(3)i} \mathbf{T}_{Bn-i+1}^{(3)} - \mathbf{K}^{II-(3)i} \mathbf{T}_{An-i+1}^{(3)} \right) \\
\mathbf{V}^{III-(1)} &= \sum_{i=1}^n \left(+\mathbf{K}^{III-(1)i} \mathbf{T}_{Ai-i}^{(1)} - \mathbf{K}^{III-(1)i} \mathbf{T}_{Ai-i}^{(1)} \right) \\
\mathbf{V}^{III-(2)} &= \sum_{i=1}^n \left(+\mathbf{K}^{III-(2)i} \mathbf{T}_{Ai}^{(2)} - \mathbf{K}^{I-(2)i} \mathbf{T}_{Bi}^{(2)} \right)
\end{aligned} \tag{4-48}$$

These coupling matrices are, for $\vartheta = I, II$

$$\pm \mathbf{K}^{\vartheta-(3)} = \begin{bmatrix} \pm \mathbf{K}_{11}^{\vartheta-(3)} & \pm \mathbf{K}_{12}^{\vartheta-(3)} \\ \pm \mathbf{K}_{21}^{\vartheta-(3)} & \pm \mathbf{K}_{22}^{\vartheta-(3)} \end{bmatrix} \tag{4-49}$$

where

$$\begin{aligned}
\pm K_{11pq}^{\vartheta-(3)i} &= \sqrt{Z_p^{ej}} \sqrt{Y_q^{eIVbi}} \iint_{S^v} \bar{\mathbf{h}}_{Tp}^{ej} \cdot (\bar{\mathbf{h}}_{Tq}^{eIVbi} \pm h_y^{eIVbi} \hat{u}_y) \exp(\mp jk_{yq}^{eIVbi} [y - b_{(\vartheta)i}]) ds \\
\pm K_{12pq}^{\vartheta-(3)i} &= \sqrt{Z_p^{ej}} \sqrt{Y_q^{mIVbi}} \iint_{S^v} \bar{\mathbf{h}}_{Tp}^{ej} \cdot \bar{\mathbf{h}}_{Tq}^{mIVbi} \exp(\mp jk_{yq}^{mIVbi} [y - b_{(\vartheta)i}]) ds \\
\pm K_{21pq}^{\vartheta-(3)i} &= \sqrt{Z_p^{mj}} \sqrt{Y_q^{eIVbi}} \iint_{S^v} \bar{\mathbf{h}}_{Tp}^{mj} \cdot (\bar{\mathbf{h}}_{Tq}^{eIVbi} \pm h_y^{eIVbi} \hat{u}_y) \exp(\mp jk_{yq}^{eIVbi} [y - b_{(\vartheta)i}]) ds \\
\pm K_{22pq}^{\vartheta-(3)i} &= \sqrt{Z_p^{mj}} \sqrt{Y_q^{mIVbi}} \iint_{S^v} \bar{\mathbf{h}}_{Tp}^{mj} \cdot \bar{\mathbf{h}}_{Tq}^{mIVbi} \exp(\mp jk_{yq}^{mIVbi} [y - b_{(\vartheta)i}]) d
\end{aligned} \tag{4-50}$$

and for $v = 1, 2$

$$\pm \mathbf{K}^{\text{III}-(\nu)} = \begin{bmatrix} \pm \mathbf{K}_{11}^{\text{III}-(\nu)} & \pm \mathbf{K}_{12}^{\text{III}-(\nu)} \\ \pm \mathbf{K}_{21}^{\text{III}-(\nu)} & \pm \mathbf{K}_{22}^{\text{III}-(\nu)} \end{bmatrix} \quad (4-51)$$

where

$$\begin{aligned} \pm K_{11pq}^{\text{III}-(\nu)i} &= \sqrt{Z_p^{e\text{III}}} \sqrt{Y_q^{e\text{IVmi}}} \iint_{S^{\text{III}}} \bar{\mathbf{h}}_{Tp}^{e\text{III}} \cdot (\bar{\mathbf{h}}_{Tq}^{e\text{IVmi}} \pm h_{zq}^{e\text{IVmi}} \hat{u}_z) \exp(\mp jk_{zq}^{e\text{IVmi}} [z - c_{(\nu)i}]) ds \\ \pm K_{12pq}^{\text{III}-(\nu)i} &= \sqrt{Z_p^{e\text{III}}} \sqrt{Y_q^{m\text{IVmi}}} \iint_{S^{\text{III}}} \bar{\mathbf{h}}_{Tp}^{e\text{III}} \cdot \bar{\mathbf{h}}_{Tq}^{m\text{IVmi}} \exp(\mp jk_{zq}^{m\text{IVmi}} [z - c_{(\nu)i}]) ds \\ \pm K_{21pq}^{\text{III}-(\nu)i} &= \sqrt{Z_p^{m\text{III}}} \sqrt{Y_q^{e\text{IVmi}}} \iint_{S^{\text{III}}} \bar{\mathbf{h}}_{Tp}^{m\text{III}} \cdot (\bar{\mathbf{h}}_{Tq}^{e\text{IVmi}} \pm h_{zq}^{e\text{IVmi}} \hat{u}_z) \exp(\mp jk_{zq}^{e\text{IVmi}} [z - c_{(\nu)i}]) ds \\ \pm K_{22pq}^{\text{III}-(\nu)i} &= \sqrt{Z_p^{m\text{III}}} \sqrt{Y_q^{m\text{IVmi}}} \iint_{S^{\text{III}}} \bar{\mathbf{h}}_{Tp}^{m\text{III}} \cdot \bar{\mathbf{h}}_{Tq}^{m\text{IVmi}} \exp(\mp jk_{zq}^{m\text{IVmi}} [z - c_{(\nu)i}]) ds \end{aligned} \quad (4-52)$$

and the subscripts on b and c are the coordinate shifts for each region. In an interesting aside, it may be noted that the submatrices in eqs.(4-49) and (4-51) cover all the possible combinations of modal coupling, i.e., TE-TE, TE-TM, TM-TE, and TM-TM.

The scattering matrix has now been determined for the discontinuity distorted T-junction and is given by eq.(4-46), which can, of course, be solved by simple inversion; however, computation efficiency can best be served by another approach, namely, applying the algorithm in Appendix C. This algorithm minimizes the largest matrix to be inverted to one third the size of the matrix in eq.(4-46) by solving the submatrices individually.

Now it is possible to address the two points deferred earlier in this section. First, the formulation can be demonstrated to accommodate discontinuities with variations along the x -axis. The incorporation of such a discontinuity is accomplished by applying either the transverse resonance method or the standing wave formulation (both described in Chapter 3) to determine its scattering matrix. The formulation follows as above with the possibility now of a subregion in IV being further subdivided and producing an internal summation of its own. Second, with regard to the condition requiring that adjacent subregions to connecting waveguides have the same cross-sectional dimensions, in configurations where discontinuities appear in an aperture, the problem may be addressed by the insertion of the required subregion and the mathematical reduction of its length to zero.

4.3. T-JUNCTION WITH STEPPED RESONATOR REGION

This section now explores a T-junction with stepped resonator region. Because of the geometry of the structure with its subdivided resonator region, as depicted in Figure 4.8, the theory can be somewhat simplified. First, the junction has no variation to the x -coordinate throughout the resonator region and connecting waveguides. Therefore, the eigenfunctions with x -dependence in waveguides I, II, and III, as well as in all subregions within the stepped resonator region, are equal. The steps either ascend or descend along a coordinate axis; therefore, all discontinuities within the resonator region are single-plane steps, either in the y -coordinate or in the z -coordinate, and their scattering matrices may be calculated as in Section 2.2. Finally, it is noted that there is a single subregion in IV(3) connected to waveguide II that reduces the number of coupling matrices between the two regions. What follows is a derivation of the formula as presented in the foregoing Section 4.2 with the appropriate mathematical alterations to fit the requirements of this specific configuration.

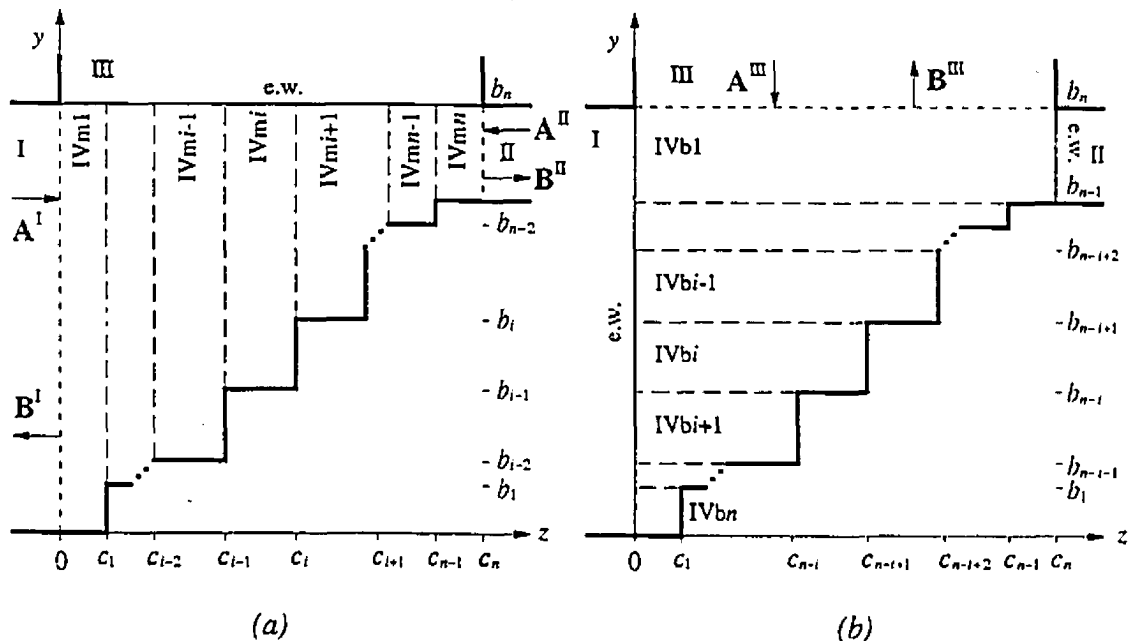


FIGURE 4.8 Subdivision assignment for the E-plane T-junction stepped resonator region: (a) subregions for solutions (1) and (2); (b) subregions for solution (3).

Beginning with the calculation of the scattering matrices within the resonator region, the cross-section functions in each subregion are

$$\begin{aligned}\Psi_{mn}^{eIVmi}(x, y) &= C_{mn}^{IVmi} \frac{\cos k_{xm}^e x}{\sqrt{1 + \delta_{om}}} \frac{\cos k_{ym}^{eIVmi}(y - b_{i-1})}{\sqrt{1 + \delta_{om}}} \\ \Psi_{mn}^{mIVmi}(x, y) &= D_{mn}^{IVmi} \sin k_{xm}^m x \sin k_{ym}^{eIVmi}(y - b_{i-1})\end{aligned}\quad (4-53)$$

and

$$\begin{aligned}\Phi_{mn}^{eIVbi}(x, y) &= C_{mn}^{IVbi} \frac{\cos k_{xm}^e x}{\sqrt{1 + \delta_{om}}} \frac{\cos k_{yn}^{eIVbi} z}{\sqrt{1 + \delta_{on}}} \\ \Phi_{mn}^{mIVbi}(x, y) &= D_{mn}^{IVbi} \sin k_{xm}^m x \sin k_{yn}^{mIVbi} z\end{aligned}\quad (4-54)$$

where

$$k_{xm}^{e,m} = \frac{m\pi}{a}, \quad k_{yn}^{e,mIVmi} = \frac{n\pi}{b_n - b_{i-1}}, \quad k_{yn}^{e,mIVmi} = \frac{n\pi}{c_{n-i+1}}, \quad (4-55)$$

and where the indices $m, n = 0, 1, 2, \dots$, ($m = n = 0$ excepted). The modes are ordered in increasing cut-off frequencies, as $m, n \rightarrow p$, $m, n \rightarrow q$. Notice, as required by the formulation, the cross-section functions of waveguide I are equal to that of subregion IVm1. Similarly, this holds true for the cross-section functions in waveguides II and III being equal to that of subregions IVm*n* and IVb1, respectively.

For solutions (1) and (2), the scattering matrices

$$\left[\begin{array}{c} \mathbf{B}^{(1)i} \\ \mathbf{A}^{(1)i+1} \end{array} \right] = \left[\begin{array}{c|c} \mathbf{S}_{11}^{(1)i} & \mathbf{S}_{12}^{(1)i} \\ \mathbf{S}_{21}^{(1)i} & \mathbf{S}_{22}^{(1)i} \end{array} \right] \left[\begin{array}{c} \mathbf{A}^{(1)i} \\ \mathbf{B}^{(1)i+1} \end{array} \right] \quad \text{at } z = c_{i-1} \quad (4-56)$$

at the interfaces $z = c_i$ for $i = 1, 2, \dots, n-1$ within the stepped resonator region are found by eqs.(2-14) to (2-16). The elements of the coupling matrices in eq.(2-16) are

$$M_{pq}^{e-e} = \sqrt{Y_p^{eIVmi}} \sqrt{Z_q^{eIVmi+1}} C_p^{IVmi} C_q^{IVmi+1} \left[J_{pq}^1 J_{pq}^2 + J_{pq}^3 J_{pq}^4 \right] \quad (4-57)$$

where

$$\begin{aligned}
J_{pq}^1 &= k_{xp}^{ei} k_{xq}^{ei+1} \int_0^a \sin k_{xp}^{ei} x \sin k_{xq}^{ei+1} x \, dx \\
J_{pq}^2 &= \int_{b_{n-1}}^{b_n} \frac{\cos k_{yp}^{eIVmi} (y - b_{i-1})}{\sqrt{1 + \delta_{0p}}} \frac{\cos k_{yq}^{eIVmi+1} (y - b_i)}{\sqrt{1 + \delta_{0q}}} \, dy \\
J_{pq}^3 &= \int_0^a \frac{\cos k_{xp}^{ei} x}{\sqrt{1 + \delta_{0p}}} \frac{\cos k_{xq}^{ei+1} x}{\sqrt{1 + \delta_{0q}}} \, dx \\
J_{pq}^4 &= k_{yp}^{eIVmi} k_{yq}^{eIVmi+1} \int_{b_{n-1}}^{b_n} \sin k_{yp}^{eIVmi} (y - b_{i-1}) \sin k_{yq}^{eIVmi+1} (y - b_i) \, dy
\end{aligned} \tag{4-58}$$

and

$$M_{pq}^{m-e} = \sqrt{Y_p^{mIVmi}} \sqrt{Z_q^{eIVmi+1}} D_p^{IVmi} C_q^{IVmi+1} [-J_{pq}^1 J_{pq}^2 + J_{pq}^3 J_{pq}^4] \tag{4-59}$$

where

$$\begin{aligned}
J_{pq}^1 &= k_{xp}^{mi} \int_0^a \cos k_{xp}^{mi} x \frac{\cos k_{xq}^{ei+1} x}{\sqrt{1 + \delta_{0q}}} \, dx \\
J_{pq}^2 &= k_{yq}^{eIVmi+1} \int_{b_{n-1}}^{b_n} \sin k_{yp}^{mIVmi} (y - b_{i-1}) \sin k_{yq}^{eIVmi+1} (y - b_i) \, dy \\
J_{pq}^3 &= k_{xq}^{ei+1} \int_0^a \sin k_{xp}^{mi} x \sin k_{xq}^{ei+1} x \, dx \\
J_{pq}^4 &= k_{yp}^{mIVmi} \int_{b_{n-1}}^{b_n} \cos k_{yp}^{mIVmi} (y - b_{i-1}) \frac{\cos k_{yq}^{eIVmi+1} (y - b_i)}{\sqrt{1 + \delta_{0q}}} \, dy
\end{aligned} \tag{4-60}$$

and

$$M_{pq}^{m-m} = \sqrt{Y_p^{mIVmi}} \sqrt{Z_q^{mIVmi+1}} D_p^{IVmi} D_q^{IVmi+1} [J_{pq}^1 J_{pq}^2 + J_{pq}^3 J_{pq}^4] \tag{4-61}$$

where

$$\begin{aligned}
J_{pq}^1 &= k_{xp}^{mi} k_{xq}^{mi+1} \int_0^a \cos k_{xp}^{mi} x \cos k_{xq}^{mi+1} x \, dx \\
J_{pq}^2 &= \int_{b_{n-1}}^{b_n} \sin k_{yp}^{mIVmi} (y - b_{i-1}) \sin k_{yq}^{mIVmi+1} (y - b_i) \, dy
\end{aligned}$$

$$\begin{aligned}
J_{pq}^3 &= \int_0^a \sin k_{xp}^{mi} x \sin k_{xq}^{mi+1} x dx \\
J_{pq}^4 &= k_{yp}^{mIVmi} k_{yq}^{mIVmi+1} \int_{b_{n-i+1}}^{b_n} \cos k_{yp}^{mIVmi} (y - b_{i-1}) \cos k_{yq}^{mIVmi+1} (y - b_i) dy
\end{aligned} \tag{4-62}$$

Furthermore, since the discontinuities within region IV(3) are also single plane steps, the scattering matrices at the interfaces within the region are determined from the coupling matrices of the same form as presented above in eqs.(4-57) to (4-62) with the exception of the appropriate interchange $y \rightarrow z$. Having determined these scattering matrices, the reflection coefficients may be calculated along with the required transfer matrices at each subregion interface as defined in the previous section [cf. eqs.(4-16), (4-22) and (4-29)]. It is now possible to write the field expressions within region IV in terms of three unknown coefficients and they are of the form seen in eqs.(4-33) and eqs.(4-40).

Applying the continuity equations for the tangential electromagnetic fields at each aperture produces an overall matrix equation for the stepped T-junction following the model of eq.(4-46). For this configuration the matrices V are similar to eqs.(4-48) with the difference that the coupling between waveguide II and region IV(3) is reduced to a single term summation, since there is only one subregion in IV(3) adjacent to waveguide II (cf. Figure 4.8). That is, for the coupling between regions IV(3) and II, the matrix V reads

$$\mathbf{V}^{\text{II-(3)}} = +\mathbf{K}^{\text{II-(3)}} \Gamma^{\text{III}} - \mathbf{K}^{\text{II-(3)}} \tag{4-63}$$

Hence, referring to eqs.(4-49) and (4-51), the coupling matrices for $\vartheta = \text{I, II}$ are

$$\begin{aligned}
\pm K_{11pq}^{\vartheta-(3)i} &= \sqrt{Z_p^j} \sqrt{Y_q^{eIVbi}} C_p^\vartheta C_q^{IVbi} \frac{\cos(k_{zq}^{eIVbi} c_{(\vartheta)})}{\sqrt{1 + \delta_{0q}}} [J_{pq}^1 J_{pq}^2 \pm J_{pq}^3 J_{pq}^4] \\
\pm K_{12pq}^{\vartheta-(3)i} &= \sqrt{Z_p^j} \sqrt{Y_q^{mIVbi}} C_p^\vartheta D_q^{IVbi} k_{zq}^{mIVbi} \cos(k_{zq}^{mIVbi} c_{(\vartheta)}) [-J_{pq}^5 J_{pq}^6] \\
\pm K_{21pq}^{\vartheta-(3)i} &= \sqrt{Z_p^{mj}} \sqrt{Y_q^{eIVbi}} D_p^\vartheta C_q^{IVbi} \frac{\cos(k_{zq}^{eIVbi} c_{(\vartheta)})}{\sqrt{1 + \delta_{0q}}} [J_{pq}^7 J_{pq}^8 \mp J_{pq}^9 J_{pq}^{10}] \\
\pm K_{22pq}^{\vartheta-(3)i} &= \sqrt{Z_p^{mj}} \sqrt{Y_q^{mIVbi}} D_p^\vartheta D_q^{IVbi} k_{zq}^{mIVbi} \cos(k_{zq}^{mIVbi} c_{(\vartheta)}) [-J_{pq}^5 J_{pq}^6]
\end{aligned} \tag{4-64}$$

where

$$\begin{aligned}
J_{pq}^1 &= k_{xp}^{ej} k_{xq}^{eIVbi} \int_0^a \sin k_{xp}^{ej} x \sin k_{xq}^{eIVbi} x dx & J_{pq}^2 &= \int_{b_w}^{b_{w+1}} \frac{\cos k_{yp}^{ej} y}{\sqrt{1+\delta_{0p}}} \exp(\mp j k_{yq}^{eIVbi} (y-b_{w+1})) dy \\
J_{pq}^3 &= (k_c^2)_p^{eIVbi} \int_0^a \frac{\cos k_{xp}^{ej} x}{\sqrt{1+\delta_{0p}}} \frac{\cos k_{xq}^{eIVbi} x}{\sqrt{1+\delta_{0q}}} dx & J_{pq}^4 &= \frac{k_{yp}^{ej}}{j k_{yq}^{eIVbi}} \int_{b_w}^{b_{w+1}} \sin k_{yp}^{ej} y \exp(\mp j k_{yq}^{eIVbi} (y-b_{w+1})) dy \\
J_{pq}^5 &= k_{xp}^{ej} \int_0^a \sin k_{xp}^{ej} x \sin k_{xq}^{eIVbi} x dx & J_{pq}^6 &= \int_{b_w}^{b_{w+1}} \frac{\cos k_{yp}^{ej} y}{\sqrt{1+\delta_{0p}}} \exp(\mp j k_{yq}^{mIVbi} (y-b_{w+1})) dy \\
J_{pq}^7 &= k_{xq}^{eIVbi} \int_0^a \sin k_{xp}^{mj} x \sin k_{xq}^{eIVbi} x dx & J_{pq}^8 &= k_{yp}^{ml} \int_{b_w}^{b_{w+1}} \cos k_{yp}^{mj} y \exp(\mp j k_{yq}^{eIVbi} (y-b_{w+1})) dy \\
J_{pq}^9 &= k_{xp}^{mj} (k_c^2)_q^{eIVbi} \int_0^a \cos k_{xp}^{mj} x \frac{\cos k_{xq}^{eIVbi}}{\sqrt{1+\delta_{0q}}} dx & J_{pq}^{10} &= \frac{1}{j k_{yq}^{eIVbi}} \int_{b_w}^{b_{w+1}} \sin k_{yp}^{mj} y \exp(\mp j k_{yq}^{eIVbi} (y-b_{w+1})) dy \\
J_{pq}^{11} &= \int_0^a \sin k_{xp}^{mj} x \sin k_{xq}^{mIVbi} x dx & J_{pq}^{12} &= k_{yp}^{mj} \int_{b_w}^{b_{w+1}} \cos k_{yp}^{mj} y \exp(\mp j k_{yq}^{mIVbi} (y-b_{w+1})) dy
\end{aligned} \tag{4-65}$$

and where $c_{I,II} = 0, c_n$ and $w = n - i$. For coupling between waveguide III and the resonator region, the equations for $\nu = 1, 2$ are

$$\begin{aligned}
\pm K_{11pq}^{III-(\nu)i} &= \sqrt{Z_p^{eIII}} \sqrt{Y_q^{eIVmi}} C_p^{III} C_q^{IVmi} \frac{\cos k_{yq}^{eIVmi} (b_n - b_{i-1})}{\sqrt{1+\delta_{0q}}} [J_{pq}^1 J_{pq}^2 \pm J_{pq}^3 J_{pq}^4] \\
\pm K_{12pq}^{III-(\nu)i} &= \sqrt{Z_p^{eIII}} \sqrt{Y_q^{mIVmi}} C_p^{III} D_q^{IVmi} k_{yq}^{mIVmi} \cos k_{yq}^{mIVmi} (b_n - b_{i-1}) [J_{pq}^5 J_{pq}^6] \\
\pm K_{21pq}^{III-(\nu)i} &= \sqrt{Z_p^{mIII}} \sqrt{Y_q^{eIVmi}} D_p^{III} C_q^{IVmi} \frac{\cos k_{yq}^{eIVmi} (b_n - b_{i-1})}{\sqrt{1+\delta_{0q}}} [-J_{pq}^7 J_{pq}^8 \pm J_{pq}^9 J_{pq}^{10}] \\
\pm K_{22pq}^{III-(\nu)i} &= \sqrt{Z_p^{mIII}} \sqrt{Y_q^{mIVmi}} D_p^{III} D_q^{IVmi} k_{yq}^{mIVmi} \cos k_{yq}^{mIVmi} (b_n - b_{i-1}) [-J_{pq}^5 J_{pq}^6]
\end{aligned} \tag{4-66}$$

where

$$\begin{aligned}
J_{pq}^1 &= k_{xp}^{eIII} k_{xq}^{eIVmi} \int_0^a \sin k_{xp}^{eIII} x \sin k_{xq}^{eIVmi} x dx & J_{pq}^2 &= \int_{c_{i-1}}^{c_i} \frac{\cos k_{zp}^{eIII} z}{\sqrt{1+\delta_{0p}}} \exp(\mp j k_{zq}^{eIVmi} (z-c_{(\nu)})) dz \\
J_{pq}^3 &= (k_c^2)_p^{eIVmi} \int_0^a \frac{\cos k_{xp}^{eIII} x}{\sqrt{1+\delta_{0p}}} \frac{\cos k_{xq}^{eIVmi}}{\sqrt{1+\delta_{0q}}} dx & J_{pq}^4 &= \frac{k_{zp}^{eIII}}{j k_{zq}^{eIVmi}} \int_{c_{i-1}}^{c_i} \sin k_{zp}^{eIII} z \exp(\mp j k_{zq}^{eIVmi} (z-c_{(\nu)})) dz
\end{aligned}$$

$$\begin{aligned}
J_{pq}^5 &= k_{xp}^{eIII} \int_0^a \sin k_{xp}^{eIII} x \sin k_{xq}^{eIVmi} x dx & J_{pq}^6 &= \int_{c_{i-1}}^{c_i} \frac{\cos k_{zp}^{eIII} z}{\sqrt{1 + \delta_{0p}}} \exp(\mp j k_{zq}^{eIVmi} (z - c_{(v)})) dz \\
J_{pq}^7 &= k_{xq}^{eIVmi} \int_0^a \sin k_{xp}^{eIII} x \sin k_{xq}^{eIVmi} x dx & J_{pq}^8 &= k_{zp}^{eIII} \int_{c_{i-1}}^{c_i} \cos k_{zp}^{eIII} z \exp(\mp j k_{zq}^{eIVmi} (z - c_{(v)})) dz \\
J_{pq}^9 &= k_{xp}^{eIII} (k_c^2)_q^{eIVmi} \int_0^a \cos k_{xp}^{eIII} x \frac{\cos k_{xq}^{eIVmi}}{\sqrt{1 + \delta_{0q}}} dx & J_{pq}^{10} &= \frac{1}{j k_{zq}^{eIVmi}} \int_{c_{i-1}}^{c_i} \sin k_{zp}^{eIII} z \exp(\mp j k_{zq}^{eIVmi} (z - c_{(v)})) dz \\
J_{pq}^{11} &= \int_0^a \sin k_{xp}^{eIII} x \sin k_{xq}^{eIVmi} x dx & J_{pq}^{12} &= k_{zp}^{eIII} \int_{c_{i-1}}^{c_i} \cos k_{zp}^{eIII} z \exp(\mp j k_{zq}^{eIVmi} (z - c_{(v)})) dz
\end{aligned}
\tag{4-67}$$

and the subscripts of c are (1) = $i - 1$ and (2) = i .

These coupling matrices can now be introduced into the general algorithm presented in Appendix C which will solve for the generalized scattering matrix of the T-junction with stepped resonator region. Because the junction is lossless and reciprocal, this scattering matrix is symmetric and orthogonal. Again, the algorithms found in Appendix A are all applicable to this scattering matrix.

4.4. WAVEGUIDE CORNERS

This section presents a confirmation of the approach outlined above in the stepped T-junction by its application to waveguide corners. As indicated earlier, the waveguide corner may be treated theoretically in the same fashion as a T-junction with one short circuited port. That is, waveguide II in Figure 4.3 is short circuited at $z = c_n$ and the resulting structure, shown in Figure 4.9, is the discontinuity-distorted waveguide corner. The straight miter configuration in this discussion is approximated by a series of steps.

Placing a short circuit on the opening of port 2 of the T-junction, the scattering matrix of a stepped T-junction is converted to that of a stepped waveguide corner. In Figure 4.3 with $\mathbf{B}^{\text{II}} = -\mathbf{A}^{\text{II}}$ at $z = c_n$, the scattering matrix \mathbf{S}^c for the corner is

$$\begin{aligned} \begin{bmatrix} \mathbf{B}^I \\ \mathbf{B}^{III} \end{bmatrix} &= \begin{bmatrix} \mathbf{S}_{11}^c & \mathbf{S}_{12}^c \\ \mathbf{S}_{21}^c & \mathbf{S}_{22}^c \end{bmatrix} \begin{bmatrix} \mathbf{A}^I \\ \mathbf{A}^{III} \end{bmatrix} \\ &= \begin{bmatrix} \mathbf{S}_{11} - \mathbf{S}_{12}(\mathbf{I} + \mathbf{S}_{22})^{-1}\mathbf{S}_{21} & \mathbf{S}_{13} - \mathbf{S}_{12}(\mathbf{I} + \mathbf{S}_{22})^{-1}\mathbf{S}_{23} \\ \mathbf{S}_{31} - \mathbf{S}_{32}(\mathbf{I} + \mathbf{S}_{22})^{-1}\mathbf{S}_{21} & \mathbf{S}_{33} - \mathbf{S}_{32}(\mathbf{I} + \mathbf{S}_{22})^{-1}\mathbf{S}_{23} \end{bmatrix} \begin{bmatrix} \mathbf{A}^I \\ \mathbf{A}^{II} \end{bmatrix} \end{aligned} \quad (4-68)$$

With twenty-five modes and a five-step approximation of a straight miter, the calculation of the entire generalized scattering matrix takes about one minute per frequency point on an IBM RISC 6000/530 workstation.

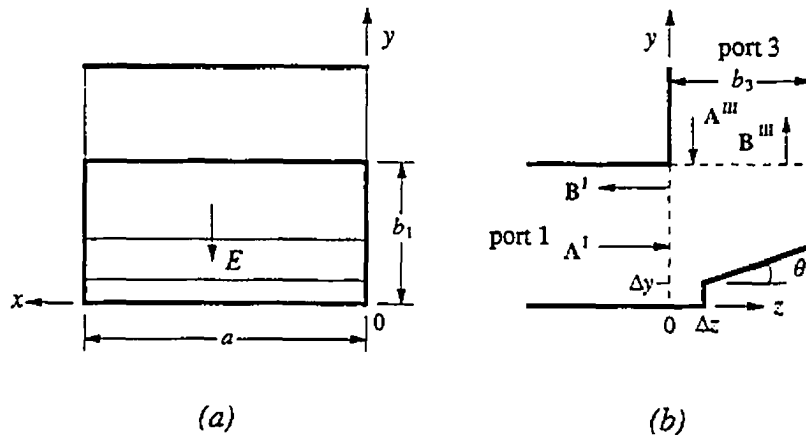


FIGURE 4.9 Structure of a waveguide corner: (a) end view; (b) side view (cf. Figure 1.3(a) for a three-dimensional view of the corner).

The major goal in a waveguide bend design is the maintenance of a specified return loss over a wide bandwidth. In addition, space requirements and insertion loss specifications may necessitate a reduction in size and refinement of the design. Clearly, in the literature, straight mitered corners have consistently demonstrated themselves to be the most effective in meeting all of these objectives. It should be noted, therefore, that the theory here presented is applied to the straight mitered corner not as an alternate method of analysis, but rather, to demonstrate the accuracy of the formulation. However, in a paper by Carle [106], satisfying return loss has been achieved in a 90° corner by using waveguide steps as a lead to the resonator region. This configuration

strongly lends itself to analysis by this theory. Using this formulation, the analysis can be accomplished even when moving the steps into the resonator region, and this could result in a significant reduction in size to the waveguide bend.

In Section 4.4.1, the published measurements of a dual-mode mitered square waveguide corner are compared to the calculated response of a step miter approximation computed by this formulation. Using the example of a mitered 180° waveguide bend, Section 4.4.2 demonstrates that the scattering parameters computed by this theory conform well to results previously calculated by other numerical techniques.

4.4.1. 90° Waveguide Corners

The step convergence analysis of an E -plane dual mode square waveguide 90° corner, assuming a staircase approximation of the straight mitered structure published by Park et al. [107], is presented in Figure 4.10. Close agreement with these results is obtained by using a twelve step approximation of the mitered corner. A similar investigation regarding the number of modes for a constant number of steps reveals that the consideration of 20 to 25 modes in the theoretical model is sufficient.

Figure 4.10(a) shows the results for a TE_{10} -mode (E -plane) excitation. The resonance effect, occurring here at approximately 9 GHz, is frequently encountered in numerical modeling of the E -plane square waveguide, and appears slightly below TE_{11} -mode cut-off frequency, for example [108]. For the H -plane (TE_{01} -mode excitation) in Figure 4.10(b), such resonances do not occur because of the vanishing electric field tangential to the miter boundary. However, this case requires the inclusion of a higher number of modes (up to 35) to satisfy this boundary condition; furthermore, up to fifteen steps must be used to approximate the straight miter. The results in Figure 4.10(b) differ from those presented in [107], because a higher frequency dependence will always be exhibited from a stepped mitered corner for the TE_{01} -mode polarization than from a straight mitered corner.

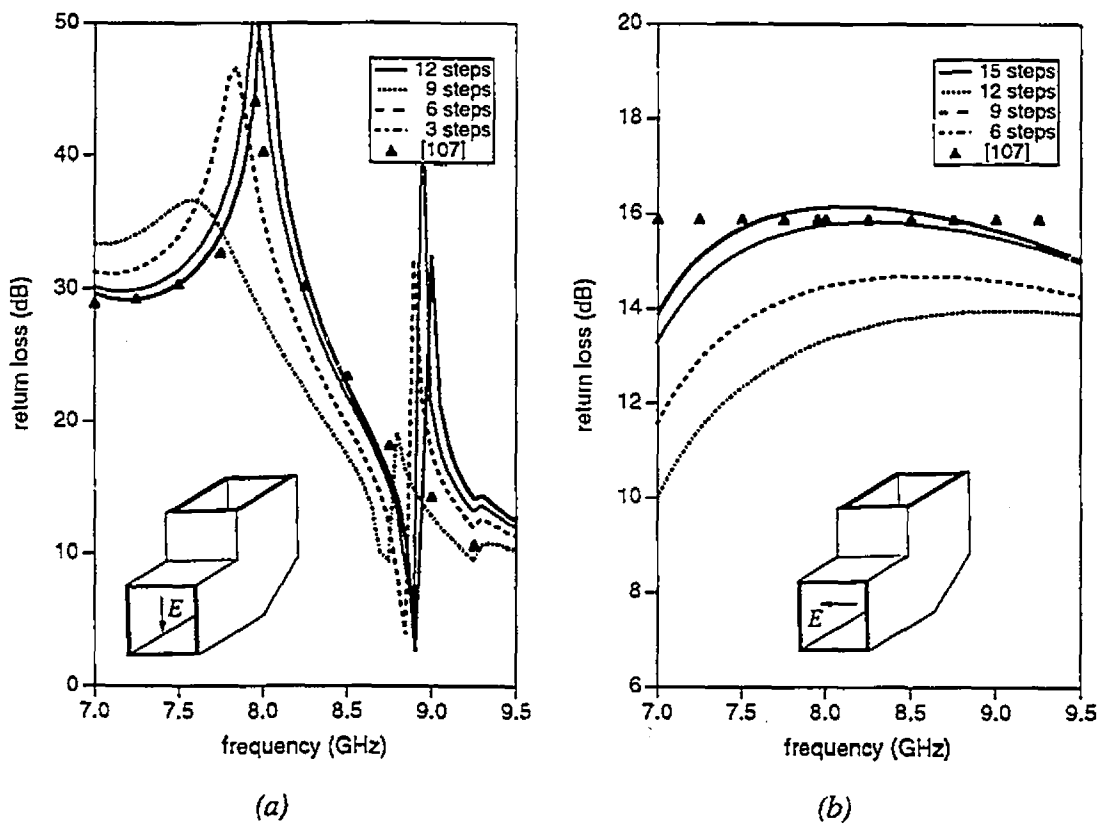


FIGURE 4.10 Input return loss of a mitered E-plane corner. Approximation of miter by increasing the number of steps. (a) TE_{10} -mode. (b) TE_{01} -mode. Dimensions (mm): $a = b_1 = b_3 = 22.86$, $\Delta y = 0.0$, $\Delta z = 5.08$, and $\theta = 45.0^\circ$ (cf. Figure 4.9).

As pointed out by Park [107], a change in the miter dimension also enables the H -plane return loss to peak within the fundamental-mode frequency range of the two orthogonal polarizations. This is demonstrated in Figure 4.11, showing again good agreement with the data provided. Here, twenty-two steps were used to approximate the straight mitered corner, again because of higher frequency dependence for this polarization.

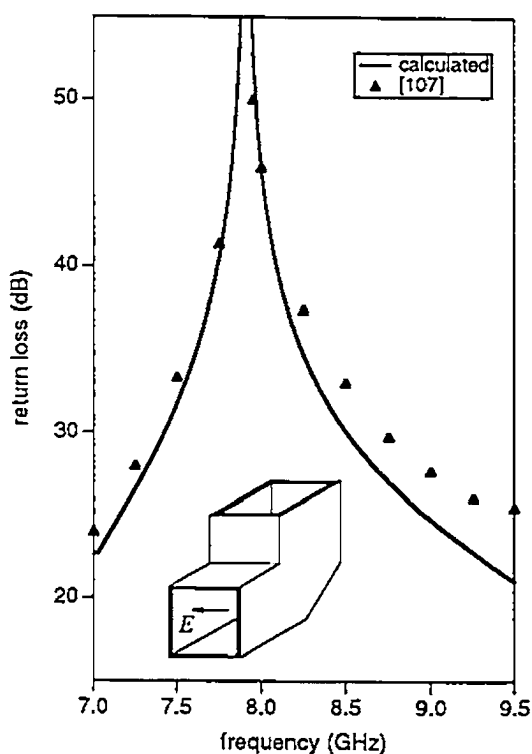


FIGURE 4.11 *Input return loss of a mitered H -plane corner with 22-step approximation. Dimensions (mm): $a = b_1 = b_3 = 22.86$, $\Delta y = 0.0$, $\Delta z = 6.55$, and $\theta = 45.0^\circ$ (cf. Figure 4.9).*

4.4.2. 180° Waveguide Corners

As a final example, the advantage of this model, i.e., the fact that the generalized scattering matrix of the discontinuity-distorted waveguide corner is

calculated instead of only the fundamental-mode scattering parameters, becomes obvious when other components are connected in close proximity to the corner, such as in the case of the 180° bend shown in Figure 4.12. Since the interactions of the higher order modes between the two 90° corners are rigorously taken into account, satisfactory agreement with the finite-element analysis is obtained.

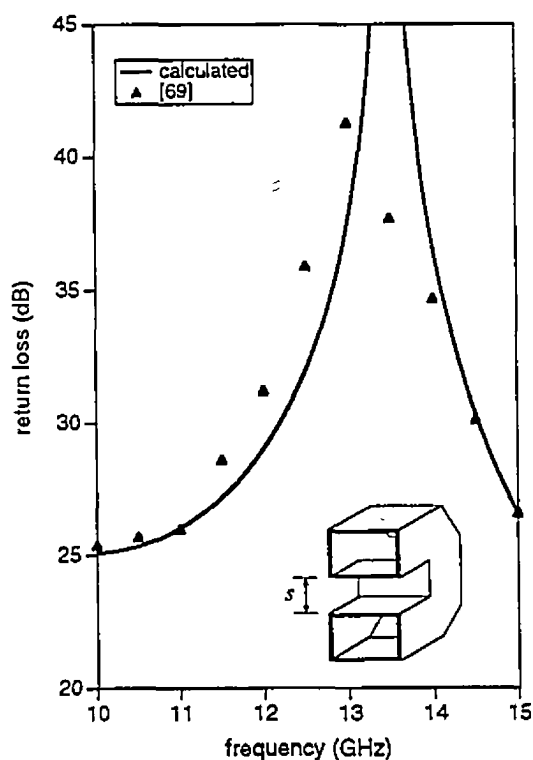


FIGURE 4.12 Comparison of this theory (five-step miter approximation) with the finite element analysis at a 180° E-plane bend [69]. Dimensions (mm): $a = 19.05$, $b_1 = 5.08$, $b_3 = 4.826$, $\Delta y = 0.0$, $\Delta z = 0.659$, $\theta = 45.0^\circ$ and $s = 6.096$ (cf. Figure 4.9).

4.5. COMPONENT DESIGN

In order to demonstrate its effectiveness, the formulation is used in this section to design two different components. First the mathematical theory is applied to

develop computer-aided design routines for the optimization of conventional power divider configurations. Next, the same is applied in the case of the orthomode transducer.

4.5.1. Power Divider

There are many types of power dividers that have been matched to a variety of different applications. Of interest to this discussion is direct power splitting by E -plane T-junctions. The typical power divider of this type consists of a conjunction of three waveguides forming an asymmetrical T, the power typically entering through one port and being divided through the T-junction. Typically, in this type of component, the only flexibility the designer has available for optimization to achieve equal power division has been the height of the waveguide itself. The width is generally kept constant throughout the component to maintain an identical fundamental-mode cutoff frequency in the adjoining waveguides. This type of division has been studied and presented by Arndt et al. in [75], and the designs, which will be optimized by the introduction of steps within the resonator region, are drawn from his work. The geometric structure of such a stepped power divider, where the steps are represented by an inclined surface at an angle θ , is shown in Figure 4.13.

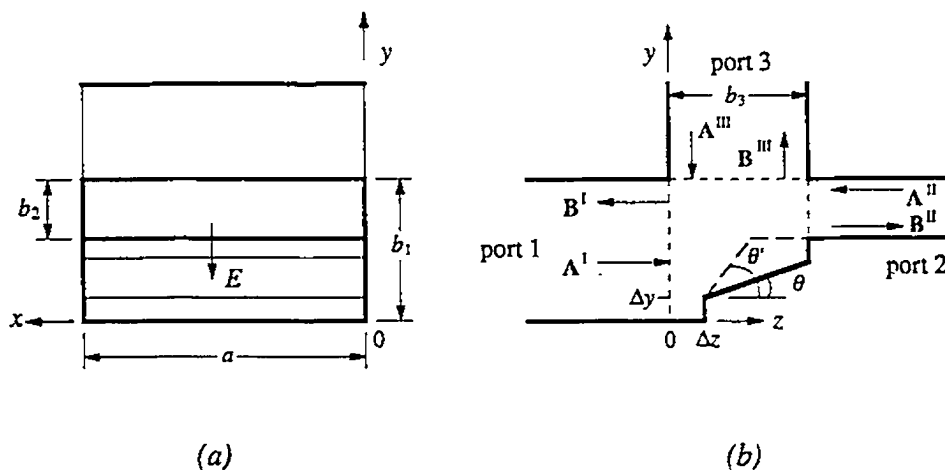


FIGURE 4.13 Structure of a compact E -plane T-junction power divider: (a) end view; (b) side view (cf. Figure 1.5(b) for a three-dimensional view of the divider).

A simple single step power divider as discussed in [75] has been recalculated using the formulation from Section 4.3. To allow compactness of design, the single waveguide step in this divider was placed within the aperture of port 2. Arndt optimized the various waveguide heights in an algorithm which cascaded the scattering matrix of two simple E -plane discontinuities, a T-junction, and a waveguide step (as calculated in Chapter 2). This presentation analyzes the same configuration by placing the step within the resonator region and mathematically reducing its distance from the aperture to zero, as described at the end of Section 4.2. It is clear from Figure 4.14 that excellent agreement between the results of these two methods exists. This figure also shows the response curves which result when the step is moved to two different coordinates within the resonator region. No significant improvement seems to be achieved, but rather some deterioration can be noted.

When, however, five steps instead of the single one, are introduced into the resonator region, improvements in bandwidth as well as a more desirable division of power are achieved, as depicted in Figure 4.15. This power divider maintains a return loss of better than 22 dB compared to 17 dB in [75] for the frequency range 10 - 15 GHz. A power division within +0.9 and -0.6 dB is obtained over the entire frequency range compared to the respective values of +1.3 and -0.8 dB. The steps in the resonator region, which are all of equal width and approximate an 18.5° incline (cf. Figure 4.13), were optimized using twenty-five modes. It should be noted that optimization was performed only for the steps and not for the height of the connecting waveguides. Computation time is approximately the same as found in the calculation of the waveguide corner.

If the waveguide heights are also optimized, the previous design may be modified to achieve a crossover in the coupling between input and output ports within the response band (cf. Figure 4.16). At a frequency of 12 GHz, 3 dB power division is accomplished with a return loss of greater than 27 dB. However, in comparison to Figure 4.15, the response deterioration is greater at the band limits.

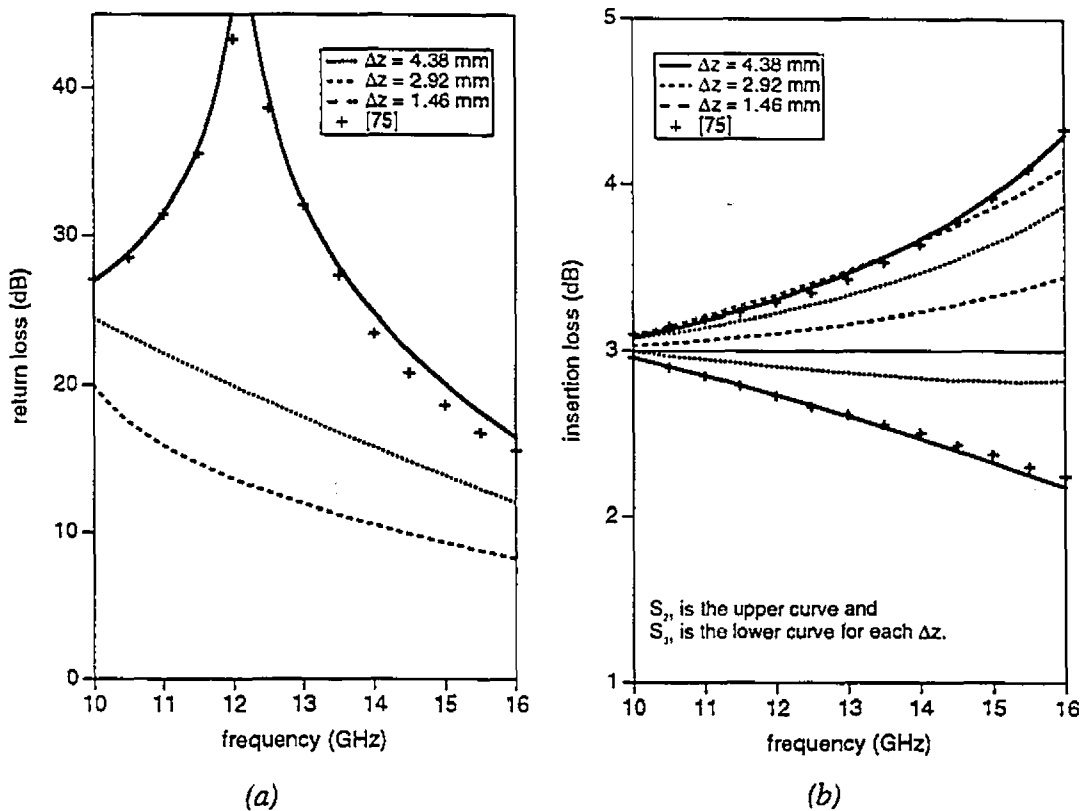


FIGURE 4.14 Comparison of this theory with [75] for a simple E-plane T-junction power divider and the effect of moving the step into the resonator region: (a) return loss; (b) insertion loss. Dimensions (mm): $a = 2b_1 = 15.799$, $b_2 = 4.41$, $b_3 = 4.38$, $\Delta y = b_1 - b_2$ and $\theta = 0^\circ$ (cf. Figure 4.13).

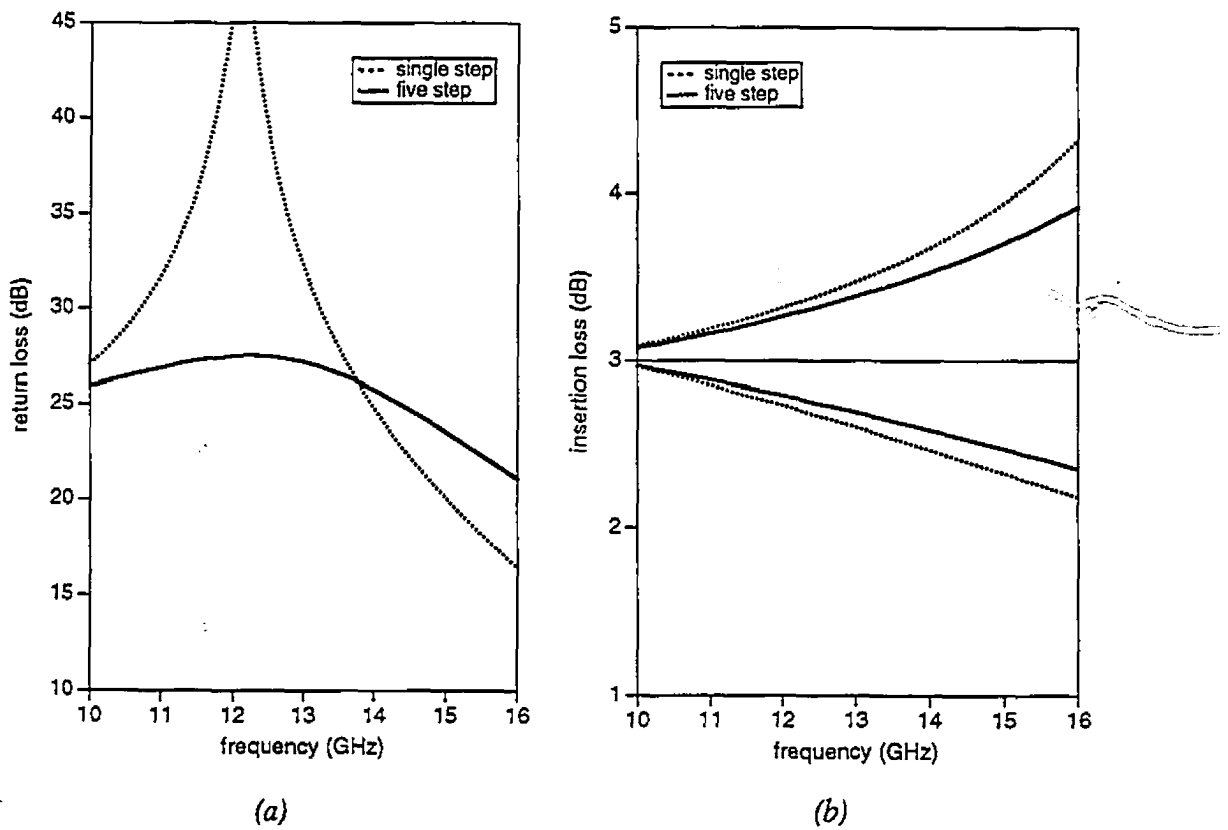


FIGURE 4.15 Performance comparison of a single step E-plane T-junction power divider as in [75] with that of a five step where $\Delta y = \Delta z = 0.0$ and $\theta = 18.5^\circ$: (a) return loss; (b) insertion loss. Waveguide dimensions as in Figure 4.14.

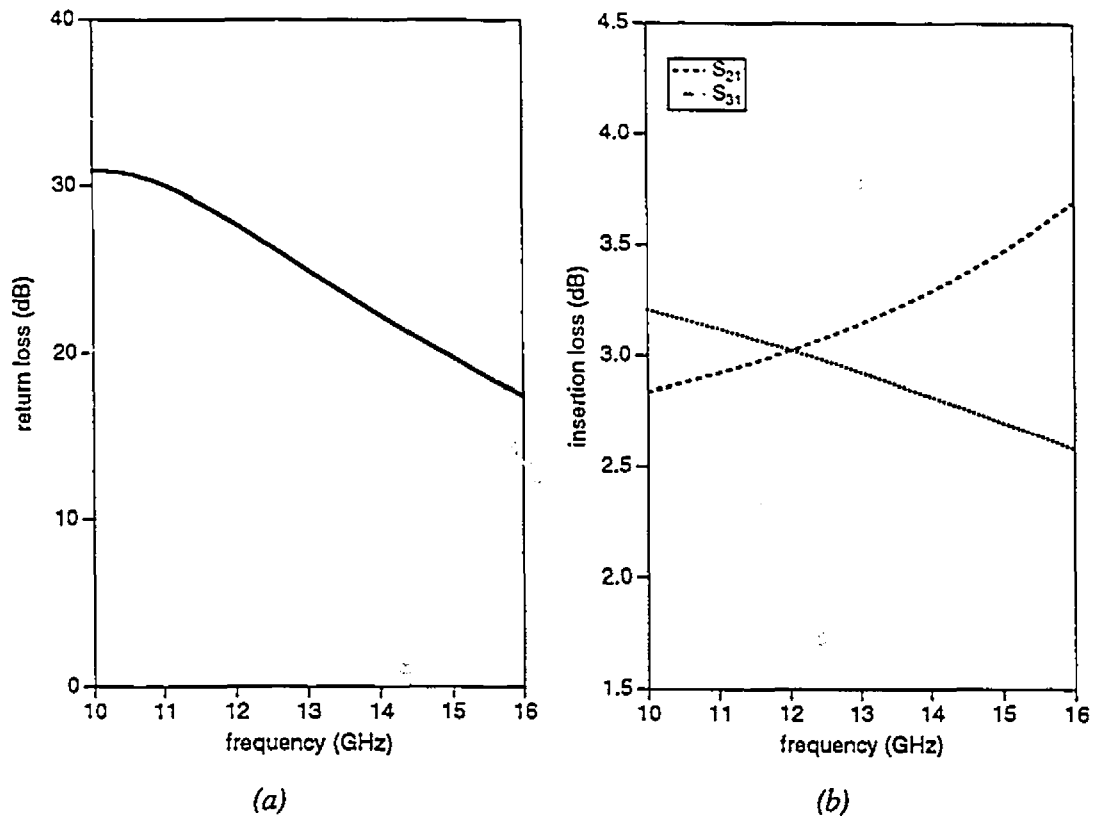


FIGURE 4.16 Response of a five step E-plane T-junction power divider achieving a 3 dB crossover for the insertion loss within the performance band: (a) return loss; (b) insertion loss. Dimensions (mm): $a = 2b_1 = 4b_2 = 15.799$, $b_3 = 4.38$, $\Delta y = \Delta z = 0.0$ and $\theta = 18.5^\circ$ (cf. Figure 4.13).

4.5.2. Orthomode Transducer

Orthomode transducers are generally used as antenna feed components to receive and separate waves of different polarizations. They are also used when either switchable polarization, or a common feed for both transmission and reception, is required. Examples include the junction formed by a connection between a circular and two rectangular waveguides to utilize simultaneously right-hand/left-hand circular and/or horizontal/vertical linear polarizations. A second example is the junction of two rectangular waveguides situated perpendicular and orthogonal to each other and connecting to a square waveguide, see Figure 1.5(c), where the primary purpose of this transducer is to separate/excite the orthogonal dominant modes (TE₁₀-mode and TE₀₁-

mode) in the square waveguide by output/input from the adjoining waveguides. This latter configuration is the one that is of interest here.

Very little computer-aided design for orthomode transducers has been published thus far in the literature, mostly due to the complicated configuration of these components and the complexity of the calculations required. Most designs to date rely heavily on empirical design formula and procedures. The approximate nature of a typical design procedure is made clear in [109] where a compact orthomode transducer has been designed for Ku-band rectangular waveguide input and circular waveguide output. Another example of this type of design method can be found in [110].

In [46] can be seen a still rare example of computer-aided design for an orthomode transducer that incorporates E -plane steps to reduce the square waveguide to a rectangular waveguide as well as a simple septum matching element. This design is clearly a prototype which will require a great deal of refinement before it can reach a useful state. It must be noted that the steps used in this design are outside the resonator region and that this is necessitated by the numerical model employed.

One of these empirical designs employs a linear double taper waveguide for the straight through arm, and the side arm is coupled to the square waveguide with a resonant iris opposite the slope face of the taper. The position of the side arm is then adjusted to obtain the most desirable impedance characteristics over the design bandwidth and matched with an inductive iris [110]. Figure 4.17 shows this design with its dimensions. Applying the new approach presented here, steps are introduced to approximate the double taper. The width-expanding taper, found in the straight through waveguide, is approximated by steps solely outside the resonator region, while for the height-reducing taper, steps are positioned both inside and outside this region. Figure 4.18 shows the agreement between the numerical model and the experimental results. It may be noted that a calculation of such a complex configuration using the port reflection coefficient method [105] becomes difficult to carry out because of the large number of discontinuities encountered on all coordinate planes both inside and outside the resonator region. With 25 modes in each of the subregions, the computation of this structure requires 20 minutes of CPU time per frequency point on an IBM RISC 6000/530 workstation. The maximum time required for other structures might be estimated from

this value as the CPU time depends -- as a rough first-order approximation -- linearly on the number of steps in the junction region.

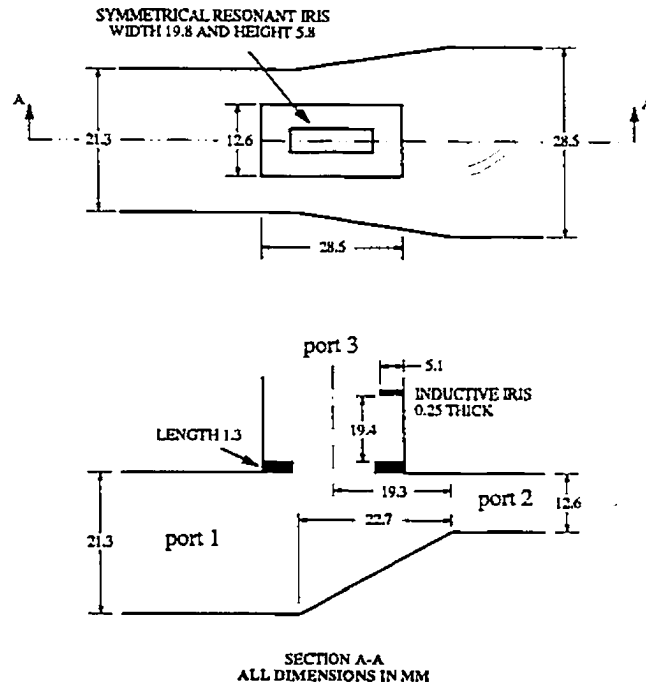


FIGURE 4.17 Configuration and dimensions of a double taper orthomode transducer.

When the compact orthomode transducer design, seen in Figure 4.19, is optimized by varying the heights and lengths of the steps within the resonator region, the response curve shown in Figure 4.20, similar to that of the computer-aided design in [46], is obtained. Both of these are composed of a 15.798 mm square waveguide input port to facilitate the excitation of both orthogonal TE_{10} and TE_{01} modes simultaneously in the output waveguides. The TE_{10} mode is transmitted to port 2 of the straight through arm, whereas the TE_{01} mode is coupled to port 3 of the side arm which is mounted perpendicular and orthogonal. The advantage of this design is in its size, being almost 60 percent shorter.

Improving upon this compact stepped orthomode transducer design by adding a resonant iris (double-plane step) at the aperture of port 3, results in the response

depicted in Figure 4.21. More than 20 dB return loss may be achieved over the bandwidth of the component by this addition. Also shown in the figure, for comparison (dashed lines), is the outcome of a return-loss calculation, which considers only the fundamental-mode scattering matrix of the junction for the connection to the iris discontinuity in the branching waveguide, while maintaining full generalized scattering matrix operation throughout all other computations. This corresponds to the scenario of calculating the discontinuity-distorted T-junction by a port reflection coefficient method involving shorting planes. The large discrepancies (of up to 10 dB) between these two approaches clearly demonstrates, first, the advantage of, and necessity for, the new generalized scattering matrix formulation presented here and, second, the limitations of the port reflection coefficient method.

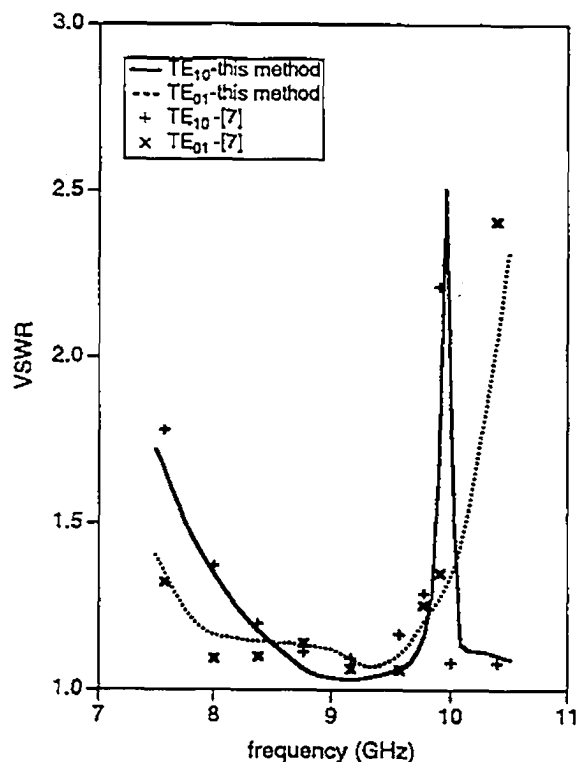


FIGURE 4.18 VSWR of rectangular waveguide orthomode transducer [110]. Dimensions in Figure 4.17.

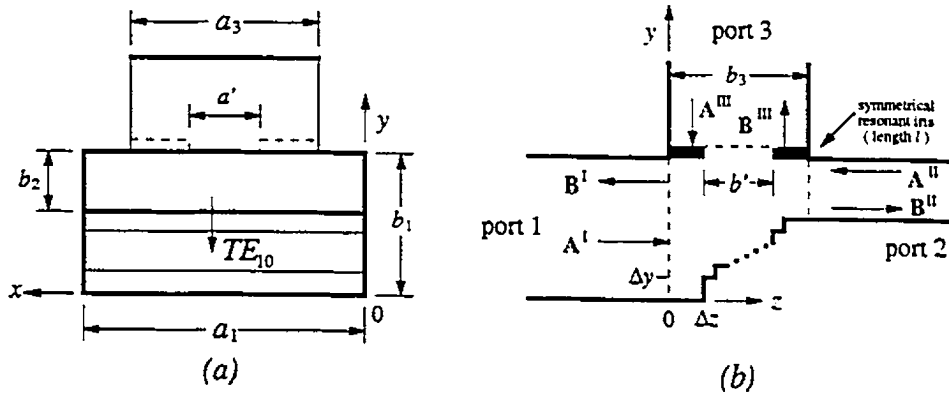


FIGURE 4.19 Compact orthomode transducer with resonant iris: (a) end view; (b) side view.

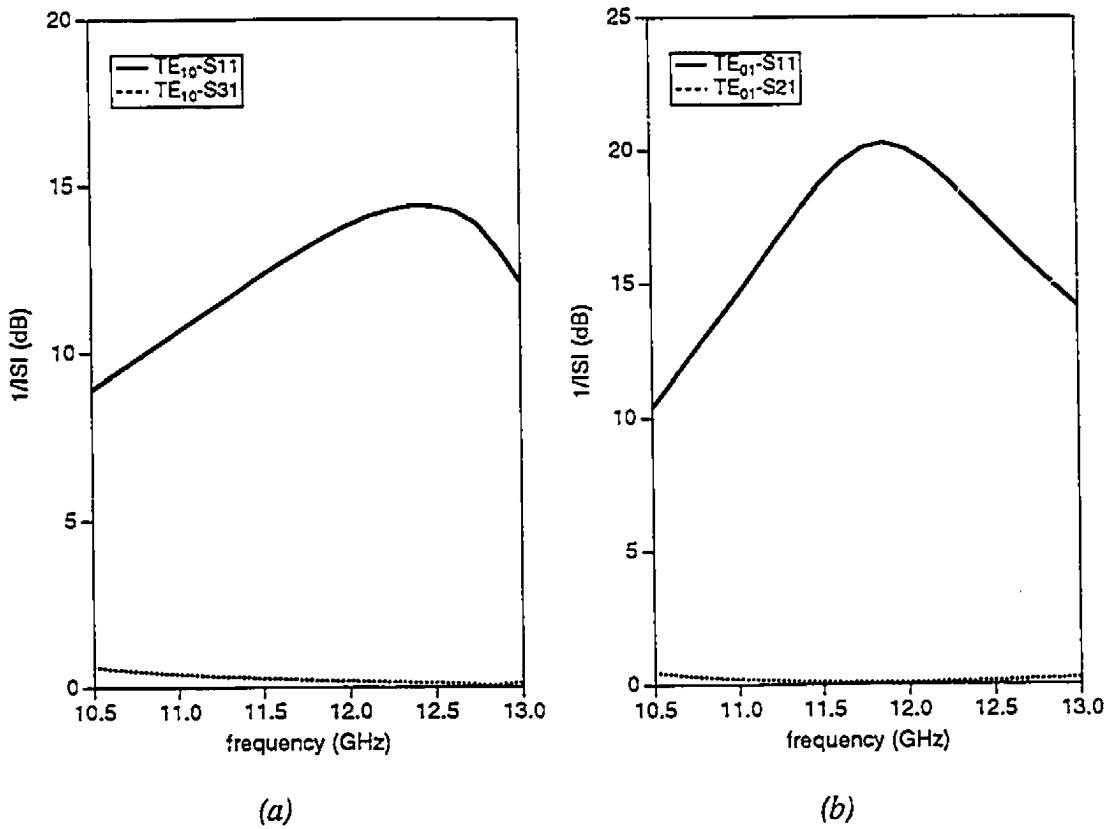


FIGURE 4.20 Performance of an optimized five step compact orthomode transducer without a resonant iris. Return loss and insertion loss for (a) TE₁₀ polarization; (b) TE₀₁ polarization. Dimensions (mm): $a_1 = 2a_3 = b_1 = 2b_2 = b_3 = 15.798$ and $\Delta y = \Delta z = 0.0$.

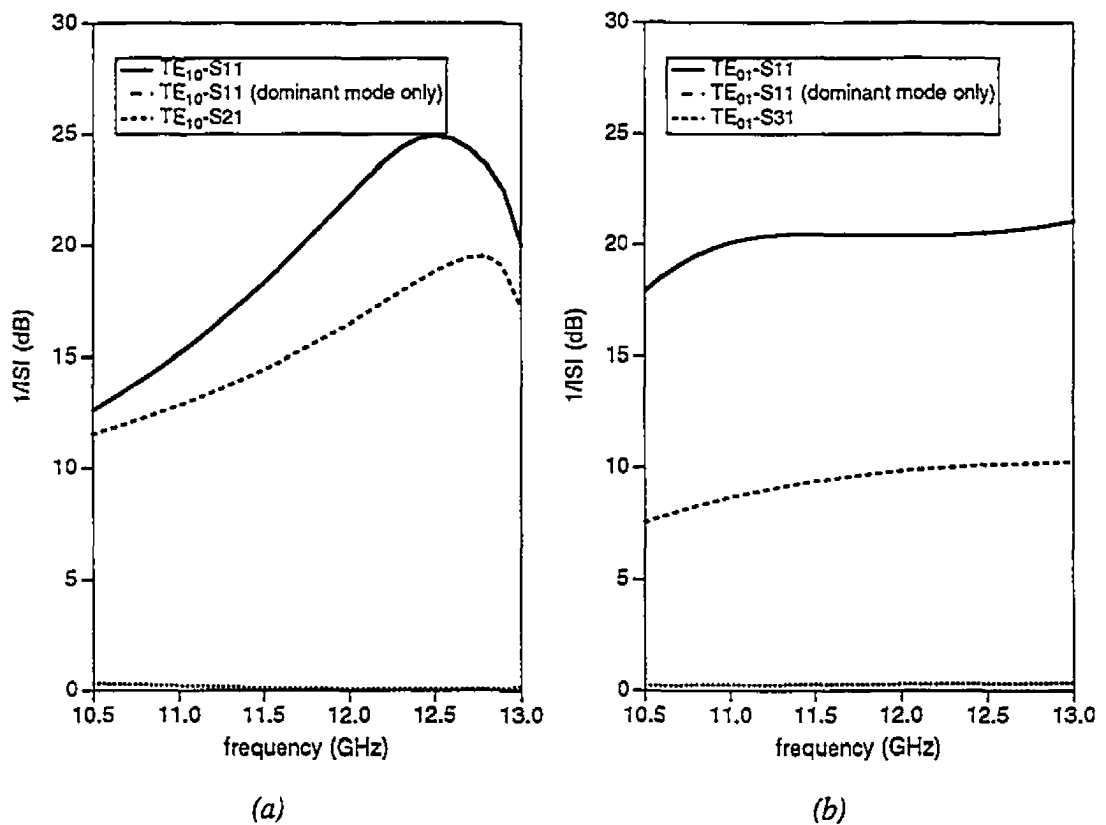


FIGURE 4.21 Performance of an optimized five step compact orthomode transducer with a resonant iris. This formulation including higher order modes at the interfaces (solid and dotted lines), fundamental-mode scattering matrix for junction (dashed lines). Return loss and insertion loss for (a) TE_{10} polarization; (b) TE_{01} polarization. Dimensions (mm): $a_1 = 2a_3 = b_1 = 2b_2 = b_3 = 15.798$, $a' = 5.924$, $b' = 11.849$, $l = 1.0$ and $\Delta y = \Delta z = 0.0$ (cf. Figure 4.19).

5. CONCLUSIONS AND RECOMMENDATIONS

5.1. CONCLUSIONS

The goal of this research has been to provide a significant contribution to the development of accurate computer-aided analysis and design of original and innovative components constructed in the all-metal nonstandard rectangular waveguide technology for microwave and satellite communication systems. The avenue pursued to accomplish this end has been the mode-matching method because of its flexibility and particular suitability to the rectangular waveguide medium, and the facile applicability of the formulations resulting from such an approach to a wide range of other waveguide technologies. Significant throughout the work and central to its methodology is what has been termed here as the 'building block' elemental approach; that is, the deliberate analysis of smaller discrete discontinuities and the cascading or combining of these into eventual component designs. Hence, the emphasis has been upon the mathematical description of the discontinuity in question rather than on the component as a whole.

In Chapter 1, the state of development in the field was presented as well as a survey of areas lending themselves to possible advancement in component design. The first such area identified for investigation was nonstandard waveguide cross-sections selected for their enhanced propagation characteristics. A second area was the introduction of discontinuities into the resonator regions of multi-ports because of its promising potential in achieving greater compactness with improved performance.

Chapter 2 then reviewed two standard discontinuities, namely, the double-plane step and the E -plane T-junction solved by the mode-matching method. This was to

form the foundation for an understanding of the unconventional discontinuities to be examined later.

One of the core discussions of this work occurs in Chapter 3, in which the rectangular-to-T-septum waveguide discontinuity was considered. To solve first for the propagation characteristics, two standard field analysis techniques were applied, namely the transverse resonance method and the standing wave formulation. It was demonstrated that a singular value decomposition method applied to the standing wave formulation improves the accuracy and reliability of the field-matching analysis in a T-septum waveguide cross-section. This technique eliminates the disadvantages of poles in the system determinant function and the need to determine the position of a zero in the occurrence of an extremely steep gradient. Close agreement with the theoretical data and direct measurements, both available from the literature, was obtained for the propagation characteristics of the T-septum waveguide. Having calculated these characteristics, this cross-sectional analysis was then applied to a rectangular-to-T-septum waveguide discontinuity.

The theoretical treatment of the T-septum waveguide mode-matching method forms a powerful tool for the computer-aided design of evanescent-mode filter applications. Through the incorporation of higher-order mode interactions, the proposed model provides design data that are in close agreement with experimental results from the testing of a 10 GHz X-band filter prototype. The broadband characteristics of the T-septum waveguide make it possible, first, to improve stopband behaviour compared to common evanescent-mode configurations and, second, to reduce considerably the size of the filter. The length of the three-resonator prototype is approximately one third of the guide's wavelength at the midband frequency. Other design data are given for the X- and Ka- bands. This technology was applied to a transformer and a typical design presented, thus demonstrating the applicability of the formulation to a T-septum-to-T-septum waveguide discontinuity.

The design of an integrated T-septum waveguide diplexer incorporating the *E*-plane T-junction followed. By employing the advantages of T-septum evanescent filter structures and reduced height waveguide technology, an extremely small component, which is ideally suited for compact front end applications, was designed and

a prototype constructed. The design procedure was based on separate channel filter design and a final optimization including all relevant parameters to improve the input return loss performance. Excellent performance was observed with respect to stopband characteristics in the higher frequencies. In both prototypes, a high dispersion loss was measured in the passbands of the filter responses. It was determined that this loss is largely attributable to the abrupt conjunction of the miniaturized T-septum filter segments with the larger input/output X-band waveguides and could be reduced by engineering a better transition between the two technologies.

In Chapter 4, the mathematical approach described for two-port junctions formed by waveguides of nonstandard cross-section was extended to multi-ports with nonstandard resonator regions. The basic building block introduced was the T-junction with a resonator region distorted by discontinuities. An approach recently proposed in the literature, in which the scattering parameters of the multi-port junction are obtained through experiments conducted using shorted ports, was determined to be inadequate for this work because, by definition, it produces only the fundamental-mode matrix. A new formulation, which applied superposition to the non-homogeneous boundary conditions of the resonator region toward a solution of the Helmholtz equation, was then proposed for determining the full-wave scattering matrix of the discontinuity-distorted T-junction. Since the discontinuities within the resonator region are rigorously taken into account and their influences are transformed to the apertures of the T-junction, the generalized scattering matrix -- as opposed to hitherto known fundamental-mode parameters -- can be calculated. The formulation was applied to a T-junction with step discontinuities placed within its resonator region and, having obtained its scattering matrix, the discontinuity could then be used as one of several basic building blocks in the design of various components.

As a first demonstration of the validity of the approach, the generalized scattering matrix of the T-junction was appropriately modified to yield that of a 90° corner. Using a stepped approximation for a straight miter, the results of this formulation are compared with the measurements of a 90° waveguide bend and with the response calculated for an 180° bend using the finite-element method. The results are in close agreement with data from the literature.

Subsequent to this, the T-junction with a stepped resonator region was introduced as a basic building block discontinuity into two component design examples, namely, the power divider and the orthomode transducer. In the case of the power divider, the recalculation of a known single-step example showed excellent agreement. Multiple steps were then introduced into the resonator region and resulted in a significant improvement in the response of the component. A similar process was carried out for an orthomode transducer. Again a known example, with more than twenty discontinuities present inside and outside the resonator region, was recalculated producing good agreement, further demonstrating the complexity of problem to which the formulation can be applied. Using the stepped resonator region T-junction, two new designs of an orthomode transducer were produced, one with, and one without, a resonant iris in the side arm. The response calculated for the one without the iris was comparable to that of a previously published and known design but had the advantage of being less than half the length. Introducing a resonant iris into the side arm resulted in a further advantage by producing a significant improvement in the response band.

These results sufficiently demonstrate that a significant contribution to the computer-aided design of components in rectangular waveguide technology has been made possible by employing the formulations, in conjunction with the mode-matching method, presented in this thesis. The foundation has been set to engender a new discussion of nonstandard discontinuities in two-port and multi-port components, making it possible to design a smaller and more efficient variety by employing the theoretical approach proposed in this work.

5.2. RECOMMENDATIONS

This line of research has been pursued with deliberate attention to its expandability and broader application in other areas of waveguide technology. The formulation, or rather set of formulations, presented in this thesis are in actuality a more efficient mathematical means of analysis developed to facilitate computer-aided component design. It is obvious that these formulations can indeed be extended to a wide range of related component design problems.

The first and most obvious proposal is to exploit the two main building blocks presented here, namely the rectangular-to-T-septum waveguide and the T-junction with stepped resonator region, by an exhaustive extension into all the component designs made possible by the ability to calculate their generalized scattering matrices. For the rectangular-to-T-septum waveguide, some examples include transformers, low pass filters, and other components that would take advantage of its dual mode nature, such as polarizers. Employing the stepped resonator region, some new designs that can be pursued, besides variations to waveguide corners, are diplexers and multiplexers.

A second recommendation is to explore the possibility of improvement to the computer algorithm in order to achieve greater numerical stability of the formulations and further reduce the CPU time expended. An example of this can be seen in the case of the stepped resonator region in which alternate matrix descriptions, such as an ABCD or admittance matrix, might be employed to transfer information from the interior subregions to the apertures, thus possibly reducing the number of matrix inversions necessary in the calculation.

Another area for further research might be to explore new waveguide technologies, such as a square coaxial guide used in antenna feed networks, the antipodal ridge guide for polarization rotation purposes, a multiple ridge guide for application in waffle-iron filters and a plus shaped guide employed as an alternative to the rectangular iris.

The formulation developed and applied in the thesis to the stepped T-junction can also be used to solve for other discontinuity-distorted resonator regions, such as the ridged E -plane T-Junction. It may be speculated that this could lead to the development of a new class of components depending on which particular discontinuity is in question. Finally, there is the whole area of open radiating components to which variants of the formulation may be applied to achieve new designing algorithms for horn antennas, active and passive waveguide radiators, and near-field obstacle compensation.

REFERENCES

- [1] J.R. Whinnery and H.W. Jamieson, "Equivalent circuits for discontinuities in transmission lines", *Proc. I.R.E.*, vol. 32, no. 2, pp. 98-114, Feb. 1944.
- [2] N. Marcuvitz (Ed.), *Waveguide Handbook*. New York: McGraw-Hill, 1951.
- [3] G. Matthaei, L. Young and E.M.T. Jones, *Microwave Filters, Impedance-Matching Networks, and Coupling Structures*. Dedham, MA: Artech House, 1980.
- [4] R.E. Collin, *Field Theory of Guided Waves*. New York: McGraw-Hill, 1960, pp.409-552.
- [5] T. Itoh, "An overview on numerical techniques for modeling miniaturized passive components", *Annales des Télécommunications*, vol. 41, pp. 449-462, Sept.-Oct. 1986.
- [6] T. Itoh (Ed.), *Numerical Techniques for Microwave and Millimeter-wave Passive Structures*. New York: John Wiley & Sons, 1989.
- [7] A. Wexler, "Computation of electromagnetic fields", *IEEE Trans. Microwave Theory Tech.*, vol. MTT-17, no. 8, pp. 416-439, Aug. 1969.
- [8] T.E. Rozzi, "The variational treatment of thick interacting inductive irises", *IEEE Trans. Microwave Theory Tech.*, vol. MTT-21, no. 2, pp. 82-88, Feb. 1973.
- [9] K. Ishibashi and E. Sawado, "Three-dimensional analysis of electromagnetic fields in rectangular waveguides by the boundary integral equation method", *IEEE Trans. Microwave Theory Tech.*, vol. MTT-38, no. 9, pp. 1300-1308, Sept. 1990.
- [10] T. Rozzi and M. Mongiardo, "E-plane steps in rectangular waveguide", *IEEE Trans. Microwave Theory Tech.*, vol. MTT-39, no. 8, pp. 1279-1288, Aug. 1991.
- [11] K. Ishibashi and E. Sawado, "A method for the rapidly convergent representation of electromagnetic fields in a rectangular waveguide", *IEEE Trans. Microwave Theory Tech.*, vol. MTT-39, no. 10, pp. 1796-1799, Oct. 1991.
- [12] M. Swaminathan, E. Arvas, T.K. Sarkar and A.R. Djordjevic, "Computation of

- cutoff wave numbers of TE and TM modes in waveguides of arbitrary cross sections using a surface integral formulation", *IEEE Trans. Microwave Theory Tech.*, vol. MTT-38, no. 2, pp. 154-159, Feb. 1990.
- [13] E. Kühn, "A contour-integral matching method for the analysis of metallic and dielectric waveguides of arbitrary cross-section", *Arch. Elektr. Übertr.*, vol. 40, pp. 263-270, May 1986.
- [14] J-W. Tao and H. Baudrand, "Multimodal variational analysis of uniaxial waveguide discontinuities", *IEEE Trans. Microwave Theory Tech.*, vol. MTT-39, no. 3, pp. 506-516, Mar. 1991.
- [15] A. Wexler, "Solution of waveguide discontinuities by modal analysis", *IEEE Trans. Microwave Theory Tech.*, vol. MTT-15, no. 9, pp. 508-517, Sept. 1967.
- [16] R. Safavi-Naini and R.H. MacPhie, "Scattering at rectangular-to-rectangular waveguide junctions", *IEEE Trans. Microwave Theory Tech.*, vol. MTT-30, no. 11, pp. 2060-2063, Nov. 1982.
- [17] R. De Smedt and B. Denturck, "Scattering matrix of junctions between rectangular waveguides", *IEE Proc.*, Vol. 130, Pt.H, no. 2, pp. 183-190, March 1983.
- [18] R.R. Mansour and R.H. MacPhie, "Scattering at an N -furcated parallel-plate waveguide junction", *IEEE Trans. Microwave Theory Tech.*, vol. MTT-33, no. 9, pp. 830-835, Sept. 1985.
- [19] H.D. Knetsch, "Beitrag zur Theorie sprunghafter Querschnittsveränderungen von Hohlleitern", *Arch. Elektr. Übertr.*, vol. 22, pp. 591-600, Dec. 1968.
- [20] P.H. Masterman and P.J.B. Clarricoats, "Computer field-matching solution of waveguide transverse discontinuities", *Proc. IEE.*, vol. 118, no. 1, pp. 51-63, Jan. 1971.
- [21] J. Esteban and J. M. Rebollar, "Generalized scattering matrix of generalized two-port discontinuities: application to four-port and non symmetric six-port couplers", *IEEE Trans. Microwave Theory Tech.*, vol. MTT-39, no. 10, pp. 1725-1734, Oct. 1991.
- [22] R. Mittra and S.W. Lee, *Analytical Techniques in the Theory of Guided Waves*, New York: MacMillan, 1971.
- [23] Q. Zhang and T. Itoh, "Spectral-domain analysis of scattering from E -plane circuits elements", *IEEE Trans. Microwave Theory Tech.*, vol. MTT-35, no. 2, pp. 138-150, Feb. 1987.
- [24] M. Koshiba and M. Suzuki, "Application of the boundary-element method to waveguide discontinuities", *IEEE Trans. Microwave Theory Tech.*, vol. MTT-34, no. 2, pp. 301-307, Feb. 1986.

- [25] S. Ramo and J. Whinnery, *Fields and Waves in Modern Radio*. New York: John Wiley & Sons, 1944.
- [26] S.B. Cohn, "Properties of ridge wave guide", *Proc. IRE*, vol. 35, pp. 783-788, Aug. 1947.
- [27] S. Hopfer, "The design of ridged waveguides", *IRE Trans. Microwave Theory Tech.*, vol. MTT-3, pp. 20-29, Oct. 1955.
- [28] T.N. Anderson, "Rectangular and ridge waveguide", *IRE Trans. Microwave Theory Tech.*, vol. MTT-4, pp. 201-209, Oct. 1956.
- [29] J.R. Pyle, "The cutoff wavelength of the TE₁₀ mode in ridged rectangular waveguide of any aspect ratio", *IEEE Trans. Microwave Theory Tech.*, vol. MTT-14, no. 4, pp. 175-183, Apr. 1966.
- [30] J.P. Montgomery, "On the complete eigenvalue solution of ridged waveguide", *IEEE Trans. Microwave Theory Tech.*, vol. MTT-19, no. 6, pp. 547-555, June 1971.
- [31] Y. Utsumi. "Variational analysis of ridged waveguide modes", *IEEE Trans. Microwave Theory Tech.*, vol. MTT-33, no. 2, pp. 111-120, Feb. 1985.
- [32] J. Bornemann, "Comparison between different formulations of the transverse resonance field-matching technique for the three-dimensional analysis of metal-finned waveguide resonators", *Int. J. Numerical Modelling*, vol. 4, pp. 63-73, 1991.
- [33] G.G. Mazumder and P.K. Saha, "A novel rectangular waveguide with double T-septums", *IEEE Trans. Microwave Theory Tech.*, vol. MTT-33, no. 11, pp. 1235-1238, Nov. 1985.
- [34] G.G. Mazumder and P.K. Saha, "Rectangular waveguide with T-shaped septa", *IEEE Trans. Microwave Theory Tech.*, vol. MTT-35, no. 2, pp. 201-204, Feb. 1987.
- [35] Y. Zhang and W.T. Joines, "Some properties of T-septum waveguides", *IEEE Trans. Microwave Theory Tech.*, vol. MTT-35, no. 8, pp. 769-775, Aug. 1987.
- [36] F.J. German and L.S. Riggs, "Bandwidth properties of rectangular T-septum waveguides", *IEEE Trans. Microwave Theory Tech.*, vol. MTT-37, no. 5, pp. 917-919, May 1989.
- [37] B.E. Pauplis and D.C. Power, "On the bandwidth of T-septum waveguide", *IEEE Trans. Microwave Theory Tech.*, vol. MTT-37, no. 5, pp. 919-922, May 1989.
- [38] Y. Zhang and W.T. Joines, "Attenuation and power-handling capability of T-septum waveguides", *IEEE Trans. Microwave Theory Tech.*, vol. MTT-35, no. 9, pp. 858-861, Sept. 1987.

- [39] P.K. Saha and G.G. Mazumder, "Bandwidth characteristics of inhomogeneous T-septum waveguides", *IEEE Trans. Microwave Theory Tech.*, vol. MTT-37, no. 6, pp. 1021-1026, June 1989.
- [40] R.R. Mansour and R.H. MacPhie, "Properties of dielectric-loaded T-septum waveguides", *IEEE Trans. Microwave Theory Tech.*, vol. MTT-37, no. 10, pp. 1654-1657, Oct. 1989.
- [41] R.S. Elliott, "Two-mode waveguide for equal mode velocities", *IEEE Trans. Microwave Theory Tech.*, vol. MTT-16, no. 5, pp. 282-286, May 1968.
- [42] N.G. Alexopoulos and M.E. Armstrong, "Two-mode waveguide for equal mode velocities: correction", *IEEE Trans. Microwave Theory Tech.*, vol. MTT-21, no. 3, pp. 157-158, March 1973.
- [43] E.D. Sharp, "An exact calculation for a T-junction of rectangular waveguides having arbitrary cross-sections", *IEEE Trans. Microwave Theory Tech.*, vol. MTT-15, no. 2, pp. 109-116, Feb. 1967.
- [44] E. Kühn, "A mode-matching method for solving field problems in waveguide and resonator circuits", *Arch. Elektr. Übertr.*, vol. 27, pp. 511-518, Dec. 1973.
- [45] X-P. Liang, K.A. Zaki and A.E. Atia "A rigorous three plane mode-matching technique for characterizing waveguide T-junctions, and its application in multiplexer design", *IEEE Trans. Microwave Theory Tech.*, vol. MTT-39, no. 12, pp. 2138-2147, Dec. 1991.
- [46] T. Sieverding and F. Arndt, "Field theoretic CAD of open or aperture matched T-junction coupled rectangular waveguide structures", *IEEE Trans. Microwave Theory Tech.*, vol. MTT-40, no. 2, pp. 353-362, Feb. 1992.
- [47] B.N. Das, N.V.S. Narasimha Sarma and A. Chakraborty, "A rigorous variational formulation of an H plane slot-coupled Tee junction", *IEEE Trans. Microwave Theory Tech.*, vol. MTT-38, no. 1, pp. 93-95, Jan. 1990.
- [48] F. Arndt, J. Bornemann, D. Grauerholz and R. Vahldieck, "Theory and design of low-insertion loss fin-line filters", *IEEE Trans. Microwave Theory Tech.*, vol. MTT-30, no. 2, pp. 155-162, Feb. 1982.
- [49] R. Vahldieck, J. Bornemann, F. Arndt and D. Grauerholz, "Optimized waveguide E -plane metal insert filters for millimeter-wave applications", *IEEE Trans. Microwave Theory Tech.*, vol. MTT-31, no. 1, pp. 65-69, Jan. 1983.
- [50] Y-C. Shih, T. Itoh and L.Q. Bui, "Computer-aided design of millimeter-wave E -plane filters", *IEEE Trans. Microwave Theory Tech.*, vol. MTT-31, no. 2, pp. 135-141, Feb. 1983.
- [51] Y-C. Shih and T. Itoh, " E -plane filters with finite-thickness septa", *IEEE Trans. Microwave Theory Tech.*, vol. MTT-31, no. 12, pp. 1009-1012, Dec. 1983.

- [52] H. Patzelt and F. Arndt, "Double-plane steps in rectangular waveguides and their application for transformers, irises, and filters", *IEEE Trans. Microwave Theory Tech.*, vol. MTT-30, no. 5, pp. 771-776, May. 1982.
- [53] F. Arndt, U. Tucholke and T. Wriedt, "Computer-optimized multisection transformers between rectangular waveguides of adjacent frequency bands", *IEEE Trans. Microwave Theory Tech.*, vol. MTT-32, no. 11, pp. 1479-1484, Nov. 1984.
- [54] F. Arndt, B. Koch, H-J. Orlok and N. Schröder, "Field theory design of rectangular waveguide broad-wall metal-insert slot couplers for millimeter-wave applications", *IEEE Trans. Microwave Theory Tech.*, vol. MTT-33, no. 2, pp. 95-104, Feb. 1985.
- [55] F. Arndt, T. Sieverding and P. Anders, "Optimum field theory design of broadband *E*-plane branch guide phase shifters and 180° couplers", *IEEE Trans. Microwave Theory Tech.*, vol. MTT-38, no. 12, pp. 1854-1861, Dec. 1990.
- [56] N.C. Albertsen and P. Skov-Madsen, "A compact septum polarizer", *IEEE Trans. Microwave Theory Tech.*, vol. MTT-31, no. 8, pp. 654-660, Aug. 1983.
- [57] F. Arndt, W. Tucholke and T. Wriedt, "Broadband dual-depth *E*-plane corrugated square waveguide polarizer", *Electron. Lett.*, vol. 20, no. 11, pp. 458-459, May 1984.
- [58] T. Ege and P. McAndrew, "Analysis of stepped septum polarizers", *Electron. Lett.*, vol. 21, no. 24, pp. 1166-1168, Nov. 1985.
- [59] J. Esteban and J.M. Rebollar, "Characterization of corrugated waveguides by modal analysis", *IEEE Trans. Microwave Theory Tech.*, vol. MTT-39, no. 6, pp. 937-943, June 1991.
- [60] Q. Zhang and T. Itoh, "Computer-aided design of evanescent-mode waveguide filter with nontouching *E*-plane fins", *IEEE Trans. Microwave Theory Tech.*, vol. MTT-36, no. 2, pp. 404-412, Feb. 1988.
- [61] J. Bornemann and F. Arndt, "Transverse resonance, standing wave, and resonator formulations of the ridge waveguide eigenvalue problem and its application to the design of *E*-plane finned waveguide filters", *IEEE Trans. Microwave Theory Tech.*, vol. MTT-38, no. 8, pp. 1104-1113, Aug. 1990.
- [62] J-C Nanan, J.W. Tao, H. Baudrand, B. Theron and S. Vigneron, "A two-step synthesis of broadband ridged waveguide bandpass filters with improved performances", *IEEE MTT-S Microwave Symp. Dig.*, pp. 547-550, 1991.
- [63] G.F. Craven and C.K. Mok, "The design of evanescent mode waveguide bandpass filters for a prescribed insertion loss characteristic", *IEEE Trans. Microwave Theory Tech.*, vol. MTT-19, no. 3, pp. 295-308, Mar. 1971.
- [64] E.S. Hensperger, "Broad-band stepped transformers from rectangular to double-

- ridged waveguide", *IRE Trans. Microwave Theory Tech.*, vol. MTT-6, pp. 311-314, July 1958.
- [65] J. Bornemann and F. Arndt, "Modal-S-matrix design of optimum stepped ridged and finned waveguide transformers", *IEEE Trans. Microwave Theory Tech.*, vol. MTT-35, no. 6, pp. 561-567, June 1987.
- [66] L. Lewin, "Propagation in curved and twisted waveguides of rectangular cross-section", *Proc. IRE*, vol. 102, part B, pp. 75-80, Jan. 1955.
- [67] J.J. Campbell and W.R. Jones, "Symmetrically truncated right-angle corners in parallel-plate and rectangular waveguides", *IEEE Trans. Microwave Theory Tech.*, vol. MTT-16, no. 8, pp. 517-529, Aug. 1968.
- [68] P. Carle, "Right-angle junction for rectangular waveguides", *21st European Microwave Conf. Proc.*, pp. 711-715, 1991.
- [69] J. Uher, J. Bornemann and U. Rosenberg, *Waveguide Components for Antenna Feed Systems. Theory and CAD*. Norwood: Artech House Inc., 1993.
- [70] A.E. Atia, "Computer-aided design of waveguide multiplexers", *IEEE Trans. Microwave Theory Tech.*, vol. MTT-22, no. 3, pp. 332-336, Mar. 1974.
- [71] J. Rhodes and R. Levy, "Design of general manifold multiplexers", *IEEE Trans. Microwave Theory Tech.*, vol. MTT-27, no. 2, pp. 111-123, Feb. 1979.
- [72] R. Vahldieck and B. Varailhon de la Filolie, "Computer-aided design of parallel-connected millimeter wave diplexers/multiplexers", *IEEE MTT-S Microwave Symp. Dig.*, pp. 435-438, 1988.
- [73] R. Vahldieck and B. Varailhon de la Filolie, "A novel waveguide quadruplexer for millimeter-wave applications", *19th European Microwave Conf. Proc.*, pp. 621-626, 1989.
- [74] J. Dittloff and F. Arndt, "Rigorous field theory design of millimeter-wave E-plane integrated circuit multiplexers", *IEEE Trans. Microwave Theory Tech.*, vol. MTT-37, no. 2, pp. 340-350, Feb. 1989.
- [75] F. Arndt, I. Ahrens, U. Papziner, U. Wiechmann and R. Wilkeit, "Optimized E-plane T-junction series power dividers", *IEEE Trans. Microwave Theory Tech.*, vol. MTT-35, no. 11, pp. 1052-1059, Nov. 1987.
- [76] R.C. Johnson, F.L. Cain and E.N. Bone, "Dual-mode coupler", *IEEE Trans. Microwave Theory Tech.*, vol. MTT-15, no. 11, pp. 651-652, Nov. 1967.
- [77] R. Levy, "Improved single and multi-aperture waveguide coupling theory, including explanation of mutual interactions", *IEEE Trans. Microwave Theory Tech.*, vol. MTT-28, no. 4, pp. 331-338, Apr. 1980.

- [78] G.G. Gentili, "Properties of TE-TM mode-matching techniques", *IEEE Trans. Microwave Theory Tech.*, vol. MTT-39, no. 9, pp. 1669-1673, Sept. 1991.
- [79] Y.C. Shih and K.G. Gray, "Convergence of numerical solutions of step-type waveguide discontinuity problems by modal analysis", *IEEE MTT-S Microwave Symp. Dig.*, pp. 233-235, 1983.
- [80] F. Dai, "Scattering and transmission matrix representations of multiguide junctions", *IEEE Trans. Microwave Theory Tech.*, vol. MTT-40, no. 7, pp. 1538-1544, July 1992.
- [81] J. Bornemann and R. Vahldieck, "Characterization of a class of waveguide discontinuities using a modified TE_{mn}^x mode approach", *IEEE Trans. Microwave Theory Tech.*, vol. MTT-38, no. 12, pp. 1816-1821, Dec. 1990.
- [82] R. Safavi-Naini and R.H. MacPhie, "On solving waveguide junction scattering problems by the conservation of complex power technique", *IEEE Trans. Microwave Theory Tech.*, vol. MTT-29, no. 4, pp. 331-343, Apr. 1981.
- [83] F. Alessandri, G. Bartolucci and R. Sorrentino, "Admittance matrix formulation of waveguide discontinuity problems: computer-aided design of branch guide directional couplers", *IEEE Trans. Microwave Theory Tech.*, vol. MTT-36, no. 2, pp. 394-403, Feb. 1988.
- [84] P. Moon and D.E. Spencer, *Field Theory Handbook*. New York: Springer-Verlag, 1971.
- [85] H. Steyskal, "On the orthogonality of approximate waveguide mode functions", *IEEE Trans. Microwave Theory Tech.*, vol. MTT-29, no. 6, pp. 615-617, June 1981.
- [86] J.M. Rebollar, J. Esteban and J.E. Page, "Fullwave analysis of three and four-port rectangular waveguide junctions", *IEEE Trans. Microwave Theory Tech.*, vol. MTT-42, no. 2, pp. 256-263, Feb. 1994.
- [87] R. Vahldieck and J. Bornemann, "A modified mode-matching technique and its application to a class of quasi-planar transmission lines", *IEEE Trans. Microwave Theory Tech.*, vol. MTT-33, no. 10, pp. 916-926, Oct. 1985.
- [88] V.A. Labay and J. Bornemann, "Matrix singular value decomposition for pole-free solutions of homogeneous matrix equations as applied to numerical modeling methods", *IEEE Microwave Guided Wave Lett.*, vol. 2, no. 2, pp. 49-51, Feb. 1992.
- [89] R.A. Horn and C.A. Johnson, *Matrix Analysis*. New York: Cambridge University Press, 1985.
- [90] V.A. Labay and J. Bornemann, "Singular value decomposition improves accuracy and reliability of T-septum waveguide field-matching analysis", *Intl. J.*

- Microwave and Millimeter-Wave CAE*, vol. 2, no. 2, pp. 82-89, 1992.
- [91] G.V. Eleftheriades, A.S. Omar, L.P.B. Katehi and G.M. Rebeiz, "Some important properties of waveguide junction generalized scattering matrices in the context of the mode matching technique", *IEEE Trans. Microwave Theory Tech.*, vol. MTT-42, no. 10, pp. 1896-1903, Oct. 1994.
- [92] G. Craven, "Waveguide bandpass filters using evanescent modes", *Electron. Lett.*, vol. 2, no. 7, pp. 251-252, July 1966.
- [93] H.F. Chappell, "Waveguide low pass filter using evanescent mode inductors", *Microwave J.*, vol. 21, no. 12, pp. 71-72, Dec. 1978.
- [94] R.V. Snyder, "Broadband waveguide or coaxial filters with wide stopbands, using a stepped-wall evanescent mode approach", *Microwave J.*, vol. 26, no. 12, pp. 83-88, Dec. 1983.
- [95] A.M.K. Saad, "Novel lowpass harmonic filters for satellite application", *IEEE MTT-S Microwave Symp. Dig.*, pp. 292-294, 1984.
- [96] L.Q. Bui, D. Ball and T. Itoh, "Broad-band millimeter-wave *E*-plane bandpass filters", *IEEE Trans. Microwave Theory Tech.*, vol. MTT-32, no. 12, pp. 1655-1658, Dec. 1984.
- [97] J. Bornemann and F. Arndt, "Modal *S*-matrix design of metal finned waveguide components and its application to transformers and filters", *IEEE Trans. Microwave Theory Tech.*, vol. MTT-40, no. 7, pp. 1528-1537, July 1992.
- [98] X-P. Liang, K.A. Zaki and A.E. Atia, "Characterizing waveguide T-junctions by three plane mode-matching techniques", *IEEE MTT-S Microwave Symp. Dig.*, pp. 849-852, 1991.
- [99] F. Arndt, J. Dittloff, U. Papziner, D. Fasold, N. Nathrath and H. Wolf, "Rigorous field theory design of compact and lightweight broadband diplexers for satellite communication systems", *19th European Microwave Conf. Proc.*, pp. 1214-1219, 1989.
- [100] A.A. Kirilenko, S.L. Senkevich, V.I. Tkachenko and B.G. Tysik, "Waveguide diplexer and multiplexer design", *IEEE Trans. Microwave Theory Tech.*, vol. MTT-42, no. 7, pp. 1393-1396, July 1994.
- [101] M. Guglielmi, "Simple CAD procedure for microwave filters and multiplexers", *IEEE Trans. Microwave Theory Tech.*, vol. MTT-42, no. 7, pp. 1347-1352, July 1994.
- [102] F. Alessandri, M. Mongiardo and R. Sorrentino, "Computer-aided design of beam forming networks for modern satellite antennas", *IEEE Trans. Microwave Theory Tech.*, vol. MTT-40, no. 6, pp. 1117-1127, June 1992.

- [103] H-W. Yao, A.E. Abdelmonem, J-F. Liang, X-P. Liang, K.A. Zaki and A. Martin, "Wide-band waveguide and ridge waveguide T-junctions for diplexer applications", *IEEE Trans. Microwave Theory Tech.*, vol. MTT-41, no. 12, pp. 2166-2173, Dec. 1993.
- [104] A. Abdelmonem and K.A. Zaki, "Slit-coupled ridge waveguide T-junction", *IEEE Microwave and Guided Wave Lett.*, vol. 5, no. 2, pp. 40-41, Feb. 1995.
- [105] Z. Ma and E. Yamashita, "Port reflection coefficient method for solving multi-port microwave network problems", *IEEE Trans. Microwave Theory Tech.*, vol. MTT-43, no. 2, pp. 331-337, Feb. 1995.
- [106] P. Carle, "New accurate and simple equivalent circuit for circular *E*-plane bends in rectangular waveguide", *Electron. Lett.*, vol. 23, no. 10, pp. 531-532, May 1987.
- [107] P.K. Park, R.L. Eisenhart and S.E. Bradshaw, "Matched dual mode square waveguide corner", *IEEE MTT-S Microwave Symp. Dig.*, pp. 155-156, 1986.
- [108] J. Esteban and J. Rebollar, "Field theory CAD of septum OMT-polarizers", *IEEE APS Int. Symp. Dig.*, pp. 2146-2149, 1992.
- [109] O. Shahan, "Orthomode transducer fits tight quarters", *M.S.N.*, vol. 19, no. 8, pp. 60-62, Aug. 1989.
- [110] R.C. Johnson, F.L. Cain and E.N. Bone, "Dual-mode coupler", *IEEE Trans. Microwave Theory Tech.*, vol. MTT-15, no. 11, pp. 651-652, Nov. 1967.
- [111] D.V. Krupezevic, V.J. Brankovic and F. Arndt, "The wave-equation FD-TD method for the efficient eigenvalue analysis and *S*-matrix computation of waveguide structures", *IEEE Trans. Microwave Theory Tech.*, vol. MTT-41, no. 12, pp. 2109-2115, Dec. 1993.
- [112] H. Jin and R. Vahldieck, "A frequency domain TLM method", *IEEE MTT-S Microwave Symp. Dig.*, pp. 775-778, 1992.

APPENDIX A: GENERALIZED S-MATRIX METHOD

A.1. INTRODUCTION

The Generalized S-matrix Method is composed of a group of algorithms that are used to cascade or combine the modal scattering matrix of two or more discontinuities. This method incorporates all higher order mode interactions between two discontinuities. The following sections describe the application of the method in four distinct cases: the cascading of two two-port discontinuities, the cascading of a two-port discontinuity followed by a homogeneous waveguide, the combining of a two-port discontinuity with its inverse separated by a finite length of waveguide, and the combination of a three-port discontinuity with that of a two-port. Each section will begin with an illustration of the case in question followed by a presentation of the mathematical formulae.

A.2. TWO TWO-PORTS

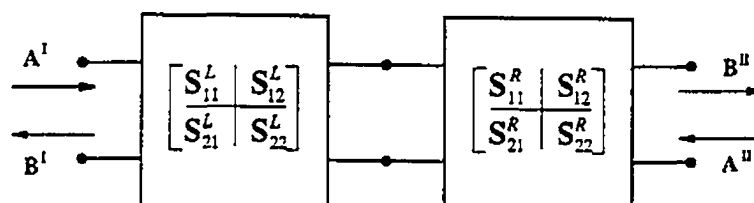


FIGURE A.1 Cascading two-port scattering matrices.

The overall scattering matrix is

$$\begin{aligned} \begin{bmatrix} \mathbf{B}^I \\ \mathbf{B}^{II} \end{bmatrix} &= \begin{bmatrix} \mathbf{S}_{11} & \mathbf{S}_{12} \\ \mathbf{S}_{21} & \mathbf{S}_{22} \end{bmatrix} \begin{bmatrix} \mathbf{A}^I \\ \mathbf{A}^{II} \end{bmatrix} \\ &= \begin{bmatrix} \mathbf{S}_{11}^L + \mathbf{S}_{12}^L \mathbf{S}_{11}^R \mathbf{W} \mathbf{S}_{21}^L & \mathbf{S}_{12}^L (\mathbf{I} + \mathbf{S}_{11}^R \mathbf{W} \mathbf{S}_{22}^L) \mathbf{S}_{12}^R \\ \mathbf{S}_{21}^R \mathbf{W} \mathbf{S}_{21}^L & \mathbf{S}_{22}^R + \mathbf{S}_{21}^R \mathbf{W} \mathbf{S}_{22}^L \mathbf{S}_{12}^R \end{bmatrix} \begin{bmatrix} \mathbf{A}^I \\ \mathbf{A}^{II} \end{bmatrix} \end{aligned} \quad (\text{A-1})$$

where

$$\mathbf{W} = (\mathbf{I} + \mathbf{S}_{22}^L \mathbf{S}_{11}^R)^{-1} \quad (\text{A-2})$$

A.3. TWO-PORT AND HOMOGENEOUS WAVEGUIDE

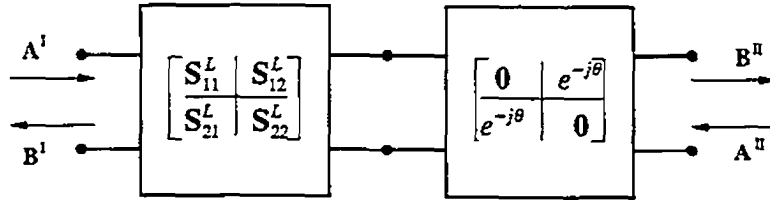


FIGURE A.2 Cascading a two-port scattering matrix with a homogeneous waveguide of electrical length θ .

For a waveguide with the propagation along the z-coordinate axis

$$\begin{aligned} \begin{bmatrix} \mathbf{B}^I \\ \mathbf{B}^{II} \end{bmatrix} &= \begin{bmatrix} \mathbf{S}_{11} & \mathbf{S}_{12} \\ \mathbf{S}_{21} & \mathbf{S}_{22} \end{bmatrix} \begin{bmatrix} \mathbf{A}^I \\ \mathbf{A}^{II} \end{bmatrix} \\ &= \begin{bmatrix} \mathbf{S}_{11}^R & \mathbf{S}_{12}^R \mathbf{U} \\ \mathbf{U} \mathbf{S}_{21}^R & \mathbf{U} \mathbf{S}_{22}^R \mathbf{U} \end{bmatrix} \begin{bmatrix} \mathbf{A}^I \\ \mathbf{A}^{II} \end{bmatrix} \end{aligned} \quad (\text{A-3})$$

where

$$\mathbf{U} = \text{diag}(-jk_{z,p}^{e,m} l)$$

and the propagation constant k_z at a frequency f is given by

$$jk_{z,p}^{e,m\text{II}} = \begin{cases} jk \sqrt{1 - \left(\frac{f_{c\text{II}}^{e,m\text{II}}}{f}\right)^2} & \text{when } f > f_{c\text{II}}^{e,m\text{II}} \\ k \sqrt{1 - \left(\frac{f}{f_{c\text{II}}^{e,m\text{II}}}\right)^2} & \text{when } f < f_{c\text{II}}^{e,m\text{II}} \end{cases} \quad (\text{A-4})$$

and where k_c and f_c are the cut-off wave number and frequency for the mode, respectively, and $k^2 = \omega^2 \mu \epsilon$.

A.4. TWO-PORT AND ITS INVERSE STRUCTURE

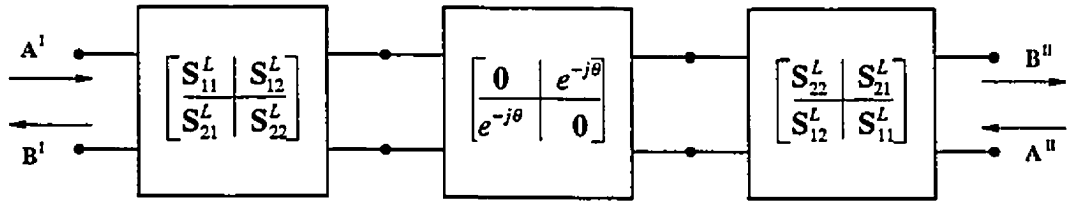


FIGURE A.3 Scattering matrix of a two-port discontinuity and its inverse separated by electrical length θ .

The generalized scattering matrix of the combined structure is

$$\begin{bmatrix} \mathbf{B}^I \\ \mathbf{B}^{II} \end{bmatrix} = \begin{bmatrix} \mathbf{S}_{11} & \mathbf{S}_{12} \\ \mathbf{S}_{21} & \mathbf{S}_{22} \end{bmatrix} \begin{bmatrix} \mathbf{A}^I \\ \mathbf{A}^{II} \end{bmatrix} \quad (\text{A-5})$$

where

$$\begin{aligned} \mathbf{S}_{11} &= \mathbf{S}_{22} = \mathbf{S}_{11}^L + \mathbf{S}_{12}^L \mathbf{U} [\mathbf{I} - \mathbf{S}_{22}^L \mathbf{U} \mathbf{S}_{22}^L \mathbf{U}]^{-1} \mathbf{S}_{22}^L \mathbf{U} \mathbf{S}_{21}^L \\ \mathbf{S}_{21} &= \mathbf{S}_{12} = \mathbf{S}_{12}^L \mathbf{U} [\mathbf{I} - \mathbf{S}_{22}^L \mathbf{U} \mathbf{S}_{22}^L \mathbf{U}]^{-1} \mathbf{S}_{21}^L \end{aligned} \quad (\text{A-6})$$

and where

$$\mathbf{U} = \text{diag}(-jk_{z,p}^{\epsilon,m}l) \quad (\text{A-7})$$

The propagation constants k_z are given in eq.(A-4).

A.5. TWO-PORT AND THREE-PORT

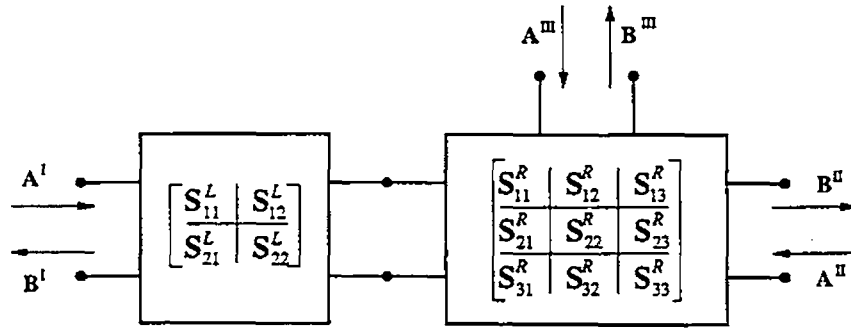


FIGURE A.4 Cascading a two-port scattering matrix with that of a three-port.

The generalized scattering matrix of a two-port connected to port 1 of a three-port is

$$\begin{bmatrix} \mathbf{B}^I \\ \mathbf{B}^{II} \\ \mathbf{B}^{III} \end{bmatrix} = \begin{bmatrix} \mathbf{S}_{11} & \mathbf{S}_{12} & \mathbf{S}_{13} \\ \mathbf{S}_{21} & \mathbf{S}_{22} & \mathbf{S}_{23} \\ \mathbf{S}_{31} & \mathbf{S}_{32} & \mathbf{S}_{33} \end{bmatrix} \begin{bmatrix} \mathbf{A}^I \\ \mathbf{A}^{II} \\ \mathbf{A}^{III} \end{bmatrix} \quad (\text{A-8})$$

where

$$\begin{aligned} \mathbf{S}_{11} &= \mathbf{S}_{11}^L + \mathbf{S}_{12}^L \mathbf{W} \mathbf{S}_{11}^R \mathbf{S}_{21}^L \\ \mathbf{S}_{12} &= \mathbf{S}_{12}^L \mathbf{W} \mathbf{S}_{12}^R \\ \mathbf{S}_{13} &= \mathbf{S}_{12}^L \mathbf{W} \mathbf{S}_{13}^R \\ \mathbf{S}_{21} &= \mathbf{S}_{21}^R \mathbf{S}_{21}^L + \mathbf{S}_{21}^R \mathbf{S}_{22}^L \mathbf{W} \mathbf{S}_{11}^R \mathbf{S}_{21}^L \\ \mathbf{S}_{22} &= \mathbf{S}_{21}^R \mathbf{S}_{22}^L \mathbf{W} \mathbf{S}_{12}^R + \mathbf{S}_{22}^R \\ \mathbf{S}_{23} &= \mathbf{S}_{21}^R \mathbf{S}_{22}^L \mathbf{W} \mathbf{S}_{13}^R + \mathbf{S}_{23}^R \end{aligned}$$

$$\begin{aligned}
\mathbf{S}_{31} &= \mathbf{S}_{31}^R \mathbf{S}_{21}^L + \mathbf{S}_{31}^R \mathbf{S}_{22}^L \mathbf{W} \mathbf{S}_{11}^R \mathbf{S}_{21}^L \\
\mathbf{S}_{32} &= \mathbf{S}_{31}^R \mathbf{S}_{22}^L \mathbf{W} \mathbf{S}_{12}^R + \mathbf{S}_{32}^R \\
\mathbf{S}_{33} &= \mathbf{S}_{31}^R \mathbf{S}_{22}^L \mathbf{W} \mathbf{S}_{13}^R + \mathbf{S}_{33}^R
\end{aligned} \tag{A-9}$$

and where

$$\mathbf{W} = (\mathbf{I} - \mathbf{S}_{11}^R \mathbf{S}_{11}^L)^{-1}. \tag{A-10}$$

Connecting a two-port to either port 2 or 3 is calculated according to this algorithm with a cyclic interchange of port numbers.

APPENDIX B: ELECTRIC FIELD DISTRIBUTION

This appendix shows the real part of the electric field distribution calculated from the known scattering matrix at the rectangular-to-T-septum waveguide discontinuity. Figure B.1 depicts the cross-sectional dimensions thereof which were used to calculate this field distribution at $y = 0$. Figures B.2-B.3 demonstrate the convergence of the y -component of the electric field according to the number of modes: 5, 15, 25 and 40. Though the y -component is the only one shown because of its majority contribution to the field, the other components can be similarly calculated. At the interface, the electric field would completely match if an infinite number of modes were taken into account. As seen in Figure B.1, using only 5 or 15 modes obviously leads to considerable error in field distribution. The high amplitude of the electric field is due to the normalization to 1W for the incoming TE_{10} -mode in Region I (cf. Figure 3.4). Note that this normalization has no effect on the scattering matrix itself.

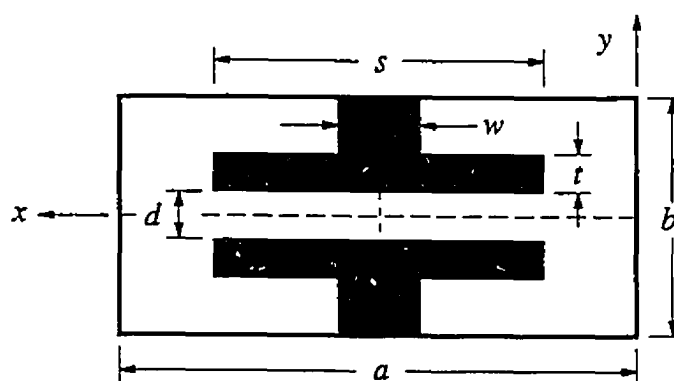


FIGURE B.1 *The cross-sectional dimensions of the rectangular-to-T-septum waveguide discontinuity used for the calculation of the electric field distribution.*

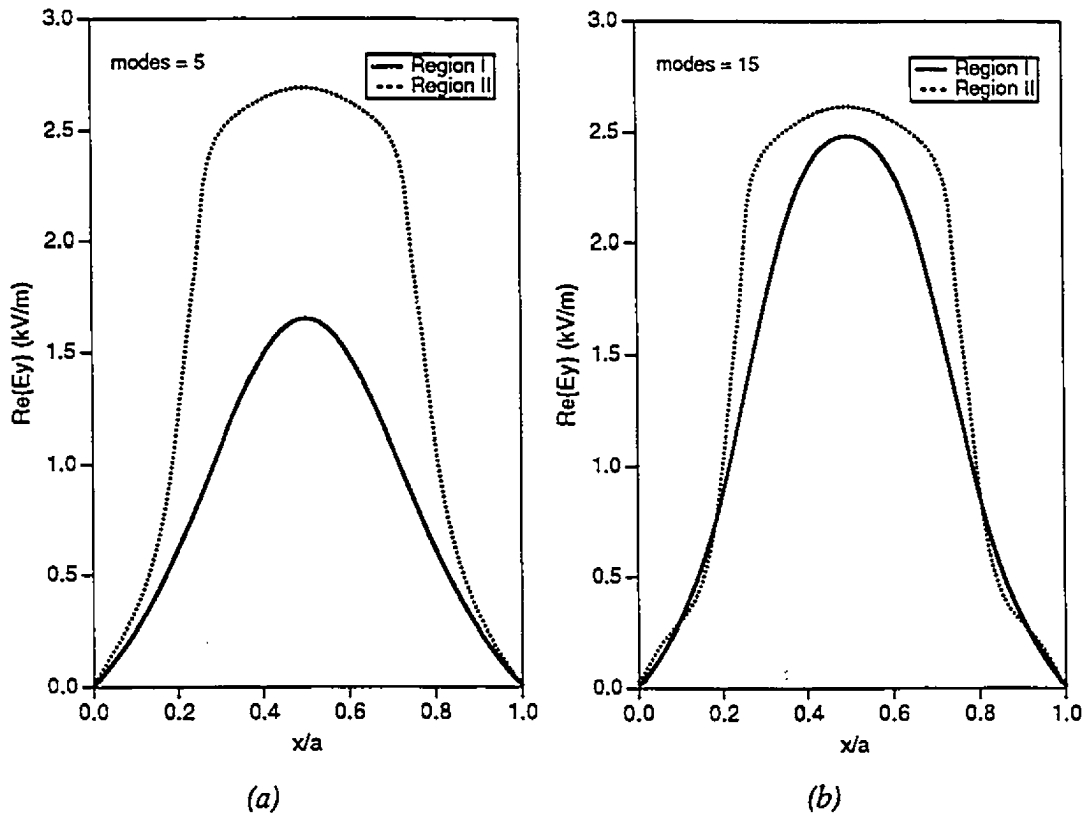


FIGURE B.2 The real part of the y-component of the electric field distribution at the rectangular-to-T-septum interface as a function of x at $y=0$. (a) 5 modes; (b) 15 modes. Dimensions: $a/b=0.5$, $d/b=0.2$, $t/b=0.05$, $s/a=0.5$, and $w/a=0.25$ (cf. Figure B.1).

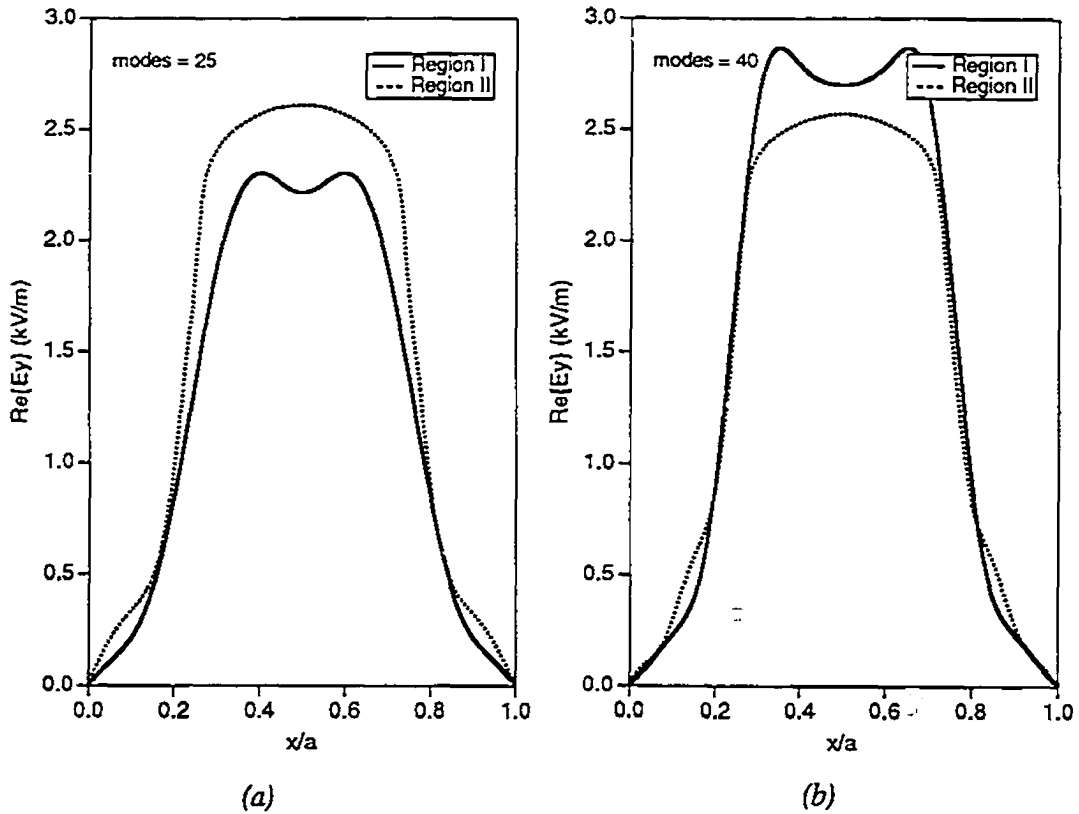


FIGURE B.3 The real part of the y -component of the electric field distribution at the rectangular-to-T-septum interface as a function of x at $y=0$. (a) 25 modes; (b) 40 modes. Dimensions: $a/b=0.5$, $d/b=0.2$, $t/b=0.05$, $s/a=0.5$, and $w/a=0.25$ (cf. Figure B.1).

A further increase in the number of modes shows an improved field convergence. It should be noted that the dimensions chosen for figures B.2 and B.3 are critical due to the narrow gap width; larger gap widths show a field convergence with a much lower number of modes. Conversely, the determination of the scattering matrix for the rectangular-to-T-septum waveguide necessarily involves an integration and, therefore, convergence occurs at approximately 25 modes for this structure.

APPENDIX C: ALTERNATIVE MATRIX INVERSION

The following formulation is put forth in this work to solve the eq.(4-46) rather than by simple inversion in order to obtain computation efficiency. This algorithm requires five matrix inversions which are one third the size of the original matrix and reduces the CPU time to less than 20% that of the single inversion.

First, the matrix equation is rewritten as

$$\left[\begin{array}{c|c|c} -\mathbf{I} - \mathbf{M}_1 & -\mathbf{M}_2 & -\mathbf{M}_3 \\ \hline -\mathbf{M}_4 & \mathbf{I} + \mathbf{M}_5 & -\mathbf{M}_6 \\ \hline -\mathbf{M}_7 & -\mathbf{M}_8 & \mathbf{I} + \mathbf{M}_9 \end{array} \right] \begin{bmatrix} \mathbf{B}^I \\ \mathbf{B}^{II} \\ \mathbf{B}^{III} \end{bmatrix} = \left[\begin{array}{c|c|c} -\mathbf{I} + \mathbf{M}_1 & \mathbf{M}_2 & \mathbf{M}_3 \\ \hline \mathbf{M}_4 & \mathbf{I} - \mathbf{M}_5 & \mathbf{M}_6 \\ \hline \mathbf{M}_7 & -\mathbf{M}_8 & \mathbf{I} - \mathbf{M}_9 \end{array} \right] \begin{bmatrix} \mathbf{A}^I \\ \mathbf{A}^{II} \\ \mathbf{A}^{III} \end{bmatrix} \quad (\text{C-1})$$

then, the variable \mathbf{B} is partially separated by

$$\begin{aligned} \mathbf{B}^I &= \mathbf{N}_1 \mathbf{N}_2 \mathbf{B}^{III} + \mathbf{N}_1 \mathbf{N}_2 \mathbf{A}^I + \mathbf{N}_1 \mathbf{N}_4 \mathbf{A}^{II} + \mathbf{N}_1 \mathbf{N}_2 \mathbf{A}^{III} \\ \mathbf{B}^{II} &= \mathbf{N}_5 \mathbf{N}_6 \mathbf{B}^{III} + \mathbf{N}_5 \mathbf{N}_7 \mathbf{A}^I + \mathbf{N}_5 \mathbf{N}_8 \mathbf{A}^{II} + \mathbf{N}_5 \mathbf{N}_6 \mathbf{A}^{III} \end{aligned} \quad (\text{C-2})$$

where

$$\begin{aligned} \mathbf{N}_1 &= \left[-(\mathbf{I} + \mathbf{M}_1) + \mathbf{M}_2 (\mathbf{I} + \mathbf{M}_5)^{-1} \mathbf{M}_4 \right]^{-1} & \mathbf{N}_5 &= \left[-(\mathbf{I} + \mathbf{M}_5) + \mathbf{M}_4 (\mathbf{I} + \mathbf{M}_1)^{-1} \mathbf{M}_2 \right]^{-1} \\ \mathbf{N}_2 &= \mathbf{M}_3 + \mathbf{M}_2 (\mathbf{I} + \mathbf{M}_5)^{-1} \mathbf{M}_6 & \mathbf{N}_6 &= \mathbf{M}_6 + \mathbf{M}_4 (\mathbf{I} + \mathbf{M}_1)^{-1} \mathbf{M}_3 \\ \mathbf{N}_3 &= -(\mathbf{I} - \mathbf{M}_1) + \mathbf{M}_2 (\mathbf{I} + \mathbf{M}_5)^{-1} \mathbf{M}_4 & \mathbf{N}_7 &= \mathbf{M}_4 \left[\mathbf{I} + (\mathbf{I} + \mathbf{M}_1)^{-1} (\mathbf{I} - \mathbf{M}_1) \right] \\ \mathbf{N}_4 &= \mathbf{M}_2 \left[\mathbf{I} + (\mathbf{I} + \mathbf{M}_5)^{-1} (\mathbf{I} - \mathbf{M}_5) \right] & \mathbf{N}_8 &= (\mathbf{I} - \mathbf{M}_5) - \mathbf{M}_4 (\mathbf{I} + \mathbf{M}_1)^{-1} \mathbf{M}_2 \end{aligned} \quad (\text{C-3})$$

and hence,

$$\mathbf{B}^{III} = \mathbf{S}_{31} \mathbf{A}^I + \mathbf{S}_{32} \mathbf{A}^{II} + \mathbf{S}_{33} \mathbf{A}^{III} \quad (\text{C-4})$$

where

$$\begin{aligned} \mathbf{S}_{31} &= \mathbf{Y}[\mathbf{M}_7(\mathbf{I} + \mathbf{N}_1\mathbf{N}_3) + \mathbf{M}_8\mathbf{N}_5\mathbf{N}_7] \\ \mathbf{S}_{32} &= \mathbf{Y}[\mathbf{M}_8 + \mathbf{M}_7\mathbf{N}_1\mathbf{N}_4 + \mathbf{M}_8\mathbf{N}_5\mathbf{N}_8] \\ \mathbf{S}_{33} &= \mathbf{Y}[(\mathbf{I} + \mathbf{M}_9) + \mathbf{M}_7\mathbf{N}_1\mathbf{N}_2 + \mathbf{M}_8\mathbf{N}_5\mathbf{N}_6] \end{aligned} \quad (\text{C-5})$$

and where

$$\mathbf{Y} = [(\mathbf{I} + \mathbf{M}_9) - \mathbf{M}_7\mathbf{N}_1\mathbf{N}_2 - \mathbf{M}_8\mathbf{N}_5\mathbf{N}_6]^{-1}. \quad (\text{C-6})$$

This now allows the expression of the complete modal scattering matrix as

$$\begin{aligned} \mathbf{B}^I &= \mathbf{S}_{11}\mathbf{A}^I + \mathbf{S}_{12}\mathbf{A}^{II} + \mathbf{S}_{13}\mathbf{A}^{III} \\ \mathbf{B}^{II} &= \mathbf{S}_{21}\mathbf{A}^I + \mathbf{S}_{22}\mathbf{A}^{II} + \mathbf{S}_{23}\mathbf{A}^{III} \end{aligned} \quad (\text{C-7})$$

where

$$\begin{aligned} \mathbf{S}_{11} &= \mathbf{N}_1[\mathbf{N}_2\mathbf{S}_{31} + \mathbf{N}_3] & \mathbf{S}_{21} &= \mathbf{N}_5[\mathbf{N}_6\mathbf{S}_{31} + \mathbf{N}_7] \\ \mathbf{S}_{12} &= \mathbf{N}_1[\mathbf{N}_2\mathbf{S}_{32} + \mathbf{N}_4] & \mathbf{S}_{22} &= \mathbf{N}_5[\mathbf{N}_6\mathbf{S}_{32} + \mathbf{N}_8] \\ \mathbf{S}_{13} &= \mathbf{N}_1\mathbf{N}_2[\mathbf{S}_{22} + \mathbf{I}] & \mathbf{S}_{23} &= \mathbf{N}_5\mathbf{N}_6[\mathbf{S}_{33} + \mathbf{I}] \end{aligned} \quad (\text{C-8})$$

The generalized scattering matrix of the T-junction with discontinuity-distorted resonator region given by eq.(C-6) and eqs.(C-8) has now been determined. This scattering matrix can be combined and cascaded with any other scattering matrix using the Generalized S-matrix Method in Appendix A.

Surname: LABAY
Given Names: Vladimír Andrew

Place of Birth: Winnipeg, Manitoba, Canada
Date of Birth: 11 May 1965

EDUCATIONAL INSTITUTIONS ATTENDED

University of Victoria	1990-1995
University of Manitoba	1983-1989

DEGREES AWARDED

Master of Science in Electrical Engineering, M.Sc., 1990.
UNIVERSITY OF MANITOBA, Winnipeg, MB, Canada.

Bachelor of Science in Electrical Engineering, B.Sc. (E.E.), 1987.
UNIVERSITY OF MANITOBA, Winnipeg, MB, Canada.

HONORS AND AWARDS

Natural Sciences and Engineering Research Council Postgraduate Scholarship
1990-1992.
University of Victoria President's Research Scholarship 1991, 1992.
Graduate Research Assistantship awarded by Wardrop Engineering Inc. 1988-1990.
Engineering and St. Paul's College Dean's Honor Role 1987.
Chown Centennial Entrance Scholarship 1983 (University of Manitoba)
Governors General Award 1983.

THESES

- V.A. Labay, *Computer Modeling of a Continuous Microwave Food Process Unit*, M.Sc. Thesis, March 1990.
- V.A. Labay, *The Design of a Wireline Directional Coupler for Beam Forming Applications*, B.Sc.(E.E.) Thesis, March 1987.

PUBLICATIONS

- V.A. Labay and J. Bornemann, "Generalized scattering matrix of waveguide corners distorted by discontinuities in the resonator region", accepted for publication in *IEEE MTT-S Microwave Symp. Dig.*, 1995.
- J. Bornemann and V.A. Labay, "Ridge waveguide polarizer with finite and stepped-thickness septum", accepted for publication in *IEEE Trans. Microwave Theory Tech.*, 1995.
- V.A. Labay and J. Bornemann, "An integrated T-septum waveguide diplexer for compact front-end applications", *IEEE MTT-S Microwave Symp. Dig.*, pp. 463-466, 1993.
- V.A. Labay and J. Bornemann, "CAD of T-septum waveguide evanescent-mode filters", *IEEE Trans. Microwave Theory Tech.*, vol. MTT-41, no. 4, pp. 731-733, Apr. 1993.
- V.A. Labay and J. Bornemann, "A field-theory-based technique for the group-delay analysis of rectangular waveguide filters", *Proc. Antennas 92*, pp. 271-276, 1992.
- V.A. Labay and J. Bornemann, "A new evanescent-mode filter for densely packaged waveguide applications", *IEEE MTT-S Microwave Symp. Dig.*, pp. 901-904, 1992.
- V.A. Labay and J. Bornemann, "Matrix singular value decomposition for pole free solutions of homogeneous matrix equations as applied to numerical modeling methods", *IEEE Microwave Guided Wave Lett.*, vol. 2, no. 2, pp. 49-51, Feb. 1992.
- V.A. Labay and J. Bornemann, "Singular value decomposition improves accuracy and reliability of T-septum waveguide field-matching analysis", *Intl. J. Microwave and Millimeter-Wave CAE*, vol. 2, no. 2, pp. 82-89, Feb. 1992.

PARTIAL COPYRIGHT LICENSE

I hereby grant the right to lend my dissertation to users of the University of Victoria Library, and to make single copies only for such users or in response to a request from the Library of any other university, or similar institution, on its behalf or for one of its users. I further agree that permission for extensive copying of this dissertation for scholarly purposes may be granted by me or a member of the University designated by me. It is understood that copying or publication of this dissertation for financial gain shall not be allowed without my written permission.

TITLE OF DISSERTATION:

Computer-aided design of passive microwave components in nonstandard rectangular waveguide technology.

AUTHOR:

VLADIMIR ANDREW LABAY
28 April 1995